Mechanosensitive Ca^{2+} Signaling of *Ex Vivo* Osteocytes in Aging and Treatment

Andrea E. Campi

Submitted in partial fulfillment of the

requirements for the degree of

Doctor of Philosophy

in the Graduate School of Arts and Sciences

COLUMBIA UNIVERSITY

2019

ABSTRACT

Mechanosensitive Ca^{2+} Signaling of *Ex Vivo* Osteocytes in Aging and Treatment

Andrea E. Campi

Of the three major cell types in bone, osteocytes are considered the major mechanosensors, capable of detecting whole-bone mechanical forces at a cellular level and coordinating tissue-level bone formation and resorption responses. The pathology of age-induced bone loss, a major factor in the development of osteoporosis, is attributed to impaired osteocyte mechanosensing. However, real-time evidence of immediate osteocyte responses to mechanical load to support the blunted tissue-level responses that have been demonstrated thus far is lacking. A ubiquitous cellular response upstream of many functions in all cell types, intracellular calcium (Ca^{2+}) is an early mechanosensitive signal in osteocytes, wherein the response characteristics studied in systems of multiple scales are related to mechanical stimuli. Thus, this phenomenon can be characterized as a real-time measure of osteocyte mechanosensitivity. The objective of this thesis was to utilize an *ex vivo* model of osteocyte Ca^{2+} signaling to investigate potentially altered mechanosensitivity of the osteocyte network in two clinical contexts: aging, and a recently-approved therapy for treatment of osteoporosis. Additionally, we aimed to enhance this *ex vivo* model to identify a functional consequence of this robust Ca^{2+} signaling response to mechanical load in the context of osteocyte mechanotransduction.

We first sought to characterize and compare Ca^{2+} signaling responses to mechanical load in osteocytes from aged and young-adult mice using an *ex vivo* model to visualize cell networks in viable mouse tibiae. We found that fewer osteocytes responded to whole-bone cyclic mechanical loading in aged mice tibiae compared to those from young-adult mice and did so in a

delayed manner, suggesting a diminished mechanosensitivity to load. Osteocytes from aged mice also lacked the well-correlated relationship between Ca^{2+} signaling synchrony and cell-cell distance exhibited by young-adult osteocyte networks. Taken together, we have demonstrated, for the first time, a real-time measure of the dampened mechanosensing and lack of signal coordination in aged osteocyte networks *in situ*, which may contribute to blunted long-term bone formation responses to load.

Next, we utilized the *ex vivo* Ca^{2+} signaling model to investigate the effect of bone formation in response to treatment with sclerostin antibody (Scl-Ab) on osteocyte mechanosensing. Previous studies have identified two phases of bone formation response to Scl-Ab treatment: an initial period of rapid bone formation with short-term dosing and a return to a steady phase of bone formation response with long-term dosing. Thus, we treated mice according to three groups: vehicle, short-term Scl-Ab, and long-term Scl-Ab. Serum P1NP assays and biweekly micro-CT scans throughout the treatment period confirmed the two phases of bone formation response to Scl-Ab. At the conclusion of treatment, under *ex vivo* whole-bone loading matched at 10 N, there were no significant differences in osteocyte Ca^{2+} signaling parameters between treatment groups. However, under strain-matched loading, fewer osteocytes from the short-term group exhibited Ca^{2+} responses and the initiation of Ca^{2+} signaling was delayed. We interpreted this as reduced mechanosensing in osteocytes that have been newly-embedded in bone that has been rapidly formed in response to Scl-Ab, as confirmed by alizarin red intensity analysis in the osteocyte field of view *ex vivo*. This study provides real-time evidence of the cellular responses under the distinct phases of bone formation response to Scl-Ab and demonstrates that osteocyte mechanosensing is maintained with long-term treatment, suggesting that other mechanisms may be responsible for self-regulation of bone formation.

Given the robust Ca^{2+} responses to load characterized in osteocytes by our group and others, we concluded this work by investigating a consequence of this mechanism that may contribute to osteocyte mechanotransduction. A common Ca^{2+}-dependent mechanism that has been demonstrated in osteocytes *in vitro* with possible implications for cell-cell communication is contraction of the actin cytoskeleton. Therefore, we sought to confirm this mechanism in osteocytes maintained in their native 3D network and morphology using the *ex vivo* murine tibia model. We successfully enhanced the model to simultaneously image intracellular Ca^{2+} and the F-actin network of individual osteocytes *in situ* at high magnification using transgenic Lifeact mice paired with either Ca^{2+} dye or bred with Ca^{2+} indicator mice. In both models, using biochemical stimuli, we quantified actin network dynamics over time and identified Ca^{2+}-dependent contractile events. Under mechanical loading, phasic actin network contractions corresponded to individual Ca^{2+} peaks in single osteocytes. The mechanosensitive nature of these contractions was demonstrated by comparing cellular dynamics in single cells under two paired mechanical loading levels; interestingly, mechanosensitivity was dependent on the order of application of these load magnitudes. In identifying this novel mechanosensitive Ca^{2+}-dependent mechanism, we enhance the understanding of the mechanotransduction pathway in osteocytes and have provided a potential point of intervention in cases where osteocyte mechanotransduction is inhibited, such as in osteoporosis.

Taken together, this body of work contributes to knowledge of how osteocytes are sensing mechanical forces in different contexts and transducing signals to effector cells. We provide novel, real-time, immediate measures of osteocyte mechanosensing *in situ* that may correspond to whole-bone responses, such as age-induced bone loss or the differential responses to Scl-Ab treatment. Future work will focus on ways to recover diminished osteocyte

mechanosensing and further connect the cell responses we observe herein to long-term bone formation responses in clinical applications.

Table of Contents

List of Tables

List of Figures

Figure 4.3 Biochemically-induced Ca^{2+} responses and subsequent actin dynamics in Fluo-8 + Lifeact osteocytes. Representative time courses of intracellular Ca^{2+} and actin network strain along the short (ε, short) and long (ε, long) axes of osteocytes stimulated by addition of either **A.** 20 mM ATP (n=15 cells), or **B.** 20 μM ionomycin (n=33 cells) to the experimental system, indicated by arrows. A contractile event is identified following the peak in intracellular Ca^{2+} in response to ATP (+) while the contraction in response to ionomycin-induced Ca^{2+} influx begins immediately following the Ca^{2+} response……74

Figure 4.4 ATP-induced Ca^{2+} responses and subsequent actin dynamics in GCaMP3 + Lifeact osteocytes. Representative time courses of intracellular Ca^{2+} and actin network strain along the short (ε, short) and long (ε, long) axes of an osteocyte stimulated by the addition 10 mM ATP (n= 6 cells). Addition of media control and biochemical stimulus are indicated by arrows. Time-lapse images of GCaMP3 and Lifeact mRFP for the given osteocyte are displayed at time points before (t=0 s) and immediately after addition of ATP (t=336 s), and at return to baseline (t=600s). A contractile event is identified following the peak in intracellular Ca^{2+} (+)……..75

Figure 4.5 Ionomycin-induced Ca^{2+} responses and subsequent actin dynamics in GCaMP3 + Lifeact osteocytes. Representative time courses of intracellular Ca^{2+} and actin network strain along the short (ε, short) and long (ε, long) axes of an osteocyte stimulated by the addition 10 μM ionomycin (n= 6 cells). Addition of media control and biochemical stimulus are indicated by arrows. Time-lapse images of GCaMP3 and Lifeact mRFP for the given osteocyte are displayed

Acknowledgements

I would like to first thank my thesis committee for their support in making this body of work possible – Professors Clark Hung, Henry Hess, Lance Kam, and Liyun Wang. Your guidance has been invaluable through every step of the PhD process and I am humbled to have had the opportunity to share my work with and learn from experts in the field of biomedical engineering such as yourselves.

I owe an infinite amount of thanks to my thesis advisor, BME department chair, and director of the Bone Bioengineering Laboratory – X. Edward Guo, PhD. I have learned far more than just research methods and concepts of bone bioengineering under Ed's mentorship. He taught me the delicate balance of questioning everything with a critical eye while simultaneously having confidence in myself and my research. Thank you Ed for being an advocate for me and for this work, and for the many opportunities you provided me as a graduate student.

My journey to Columbia started at the University of Rochester, where I received support from the David T. Kearns Center under the direction of Beth Olivares, PhD. It was here as a McNair Scholar that I first learned that pursuing a PhD in biomedical engineering was even an option for a first-generation college student like myself. Through the McNair and Xerox programs sponsored by the Kearns Center, I connected with my undergraduate research mentor, Professor Amy Lerner. Sincerest thanks to Amy for supporting me in an undergraduate research endeavor that sparked my desire to delve deeper into the field through graduate study and for being a mentor to me ever since I "flew the nest" and came to NYC.

This work would not have been possible without guidance from top experts and collaborators in the field of bone research. Many thanks to Gill Holdsworth, PhD and Hua Zhu (David) Ke, PhD, who provided the opportunity to study how a promising treatment for

osteoporosis influences cellular response. It has been a pleasure to help tell this story with you and to follow the stages of this therapy to FDA approval. Professor Matt Silva from Washington University in St. Louis was kind enough to provide mice for the age studies in addition to his invaluable insights and enthusiasm regarding our findings and how they may relate to tissue-level responses.

I was extremely fortunate to spend these past six and a half years in a supportive and collaborative lab environment, owed entirely to members past and present. Drs. Andrew Baik, Bin Zhou, Ji Wang, and Eric Yu were among the first to welcome me to the lab and I am inspired by their success both at Columbia and beyond. Dr. Da Jing always made himself available as a resource and his guidance has perpetuated the success of these projects studying osteocytes *ex vivo*. I especially want to thank Dr. Genevieve Brown, someone that I've looked up to since first visiting the Columbia campus and who continues to inspire me both as a scientist and as a friend. I leave the lab in the capable hands of current BBL members. Thank you to Sam Robinson for the many, many hours of micro-CT scanning and mouse work. Even more valuable was the moral support ("someday, this will just be a thing that you did") when I was doubting myself. It's been a pleasure working with/next to and learning from Jenny Hu. I eagerly await her elegant contributions to the field of osteoarthritis and beyond. Teo Dinescu will now hold the title of the sole Andreea in the lab and I know great things will come of it. Thank you all.

I've had the pleasure of mentoring several students in the course of my PhD research and am honored to have provided a mere stepping stone in their paths to success after Columbia. Many thanks to Sarah Chiang (BS'18) for her conscientious work in analyzing and quantifying the early actin network contraction data and bearing with me when I wasn't quite sure what any of it meant yet; Lisa Torres (MS'19) for helping improve my image analysis techniques; Diana

Lu (BS'19) for running many plates of qPCR to genotype the triple transgenic mice while also developing the protocol for strain-gauging *ex vivo* mouse tibiae; Isabelle Stern (Vanderbilt '23) for aliquoting reagents, labeling tubes, tracing osteocytes, and bringing a positive and inquisitive attitude to her weekly lab visits.

The staff at Columbia are unparalleled and none of this work, nor any work that comes from our graduate program, would be possible without them. Thank you to Jarmaine Lomax, Paulette Loussaint, Michelle Cintron, James Ihn, Natalie Chee, Wendy Goldberg, Zach Corter, and Helen Cen for their hard work in keeping the department running smoothly. I'd especially like to thank Arthur Autz, who worked with me through several modifications of my loading device and helped troubleshoot problems with the Olympus confocal when I showed up in his office very frazzled.

The PhD process is not an easy one, but it is undoubtedly made easier by friends who are growing through it along with you. Emily Moore, Jen Hoi, Eben Estell, Milos Spasic, Matt Downs, Sam - thank you all for the incredible memories and treasured friendships.

The values instilled in me by my family are the compass that ultimately guided me to the completion of my PhD. Thank you to my parents Tim and Carrie for supporting my every endeavor without question and giving me the tools and the confidence to persevere. Thank you to my sisters Kayla and Jenna for inspiring me to be the best version of myself so I can be the best big sister to you. Thank you also to the Campi and Donaruma families for being a second family that always felt like home.

Lastly, I'd like to thank my incredibly supportive husband Bill for celebrating my every success and talking me through every set-back in this rollercoaster of a process over the past six and a half years. "When the day that lies ahead of me seems impossible to face, When someone

else instead of me always seems to know the way, Then I look at you and the world's alright with me, Just one look at you and I know it's gonna be a lovely day."[1]

Dedication

This work is dedicated to my late grandmother, Barbara Schultz: a brilliant woman and my biggest cheerleader, who instilled in me a love of learning and a curiosity of this great big world. Love, your Sweetie Pie.

Chapter 1: Introduction

1.1 Background

1.1.1 Cellular contributions to bone adaptation

Bone is a dynamic tissue capable of structural adaptation in response to the application or absence of mechanical loads. This fundamental assumption in bone research was originally hypothesized by Julius Wolff in the 19th century, who claimed that bone architecture aligned with mechanical stress trajectories and would adjust to follow as such[2]. Indeed, the integrity of bone tissue is highly dependent on mechanical stimulation, as evidenced in extreme cases such as differential bone gain in athletes[3, 4] and dramatic bone loss in situations of extended bedrest[5] or spaceflight[6]. These observations have motivated decades of research dedicated to the underlying cellular mechanisms contributing to this tissue response to varied mechanical loading environments in bone.

The shape and structure of bone is maintained by three primary cell types (Figure 1.1). Osteoblasts are cells of a mesenchymal stem cell lineage and are responsible for the synthesis and mineralization of new bone matrix. Osteoclasts are a multi-nucleated, hematopoietic cell type which resorbs bone. The coupled and balanced activities of these two cell types occurring on specific sites of the same bone surface is referred to as remodeling. Bone resorption and formation can also occur in an uncoupled manner and on separate surfaces to shape bone, known as modeling[7]. The third cell type, which has emerged as a critical cell type for mechanically-directed bone modeling and remodeling, is the osteocyte.

Osteocytes are derived from terminally-differentiated osteoblasts which become embedded in the bone matrix they produce. They are long-lived, dendritic cells which comprise

95% of all bone cells, speaking to their intransience[8]. Osteocytes are embedded throughout the mineralized bone matrix in an extensive interconnected network of channels known as the lacunar-canalicular system (LCS)[9]. The function of these cells was previously unknown or even considered to be inert. Unlike osteoblasts and osteoclasts found on bone surfaces, the location of osteocytes deep within the bone matrix presents a challenge for isolation of primary cells for *in vitro* studies or visualization of native osteocytes *in vivo*. Fortunately, continued improvements in research techniques and technology have facilitated the study of osteocytes and their influence on bone adaptation.

1.1.2 Osteocytes as mechanosensors

Physiological mechanical loading of long bone along its long axis results in bending, inducing compressive and tensile strains on bone surfaces. The magnitudes of these strains in the human tibia present in the range of 237–1250 με during normal ambulation[7, 10], and differences in strain magnitudes have been associated with differing degrees of bone adaptation[11, 12]. The shape, abundance, location, and connectivity of osteocytes prime them to detect these mechanical strains (Figure 1.2), but the exact mechanism by which they do so is unclear. It is most widely accepted that bending of bone creates pressure gradients within the LCS that drive interstitial fluid flow and create fluid shear stresses on the osteocyte cell membrane[13-16]. Indeed, this phenomenon has been quantified experimentally [17-19], lending further support to LCS fluid flow as the means of transduction of mechanical forces applied to the bone into a local mechanical signal perceived by osteocytes.

Osteocytes can translate changes in mechanical loading to an overall adaptive response in the form of bone modeling or remodeling. The most striking evidence of this comes from a transgenic mouse model of targeted ablation of osteocytes, in which mice were resistant to

unloading-induced bone loss[20]. It has also been established that mechanical loading and unloading influence osteocyte production of sclerostin[21], a negative regulator of the bone-forming osteoblasts, and receptor activator of nuclear factor κB ligand (RANKL)[22, 23], which activates bone-resorbing osteoclasts. Furthermore, these changes in protein production are highly correlated with sites of anabolic bone formation in response to prescribed mechanical loading in whole bones[21, 24-26]. Still, the immediate, intracellular mechanotransduction mechanisms in osteocytes which influence long-term, downstream adaptive responses remain unclear.

1.1.3 Altered mechanotransduction in clinical contexts

The ability of osteocytes to sense and translate mechanical loads can change depending on a variety of factors. For instance, as humans age, the osteocyte network degrades, as demonstrated by a reduction in osteocyte dendrite number and cell density[27]. This degeneration of osteocyte morphology and network characteristics is believed to influence osteocyte mechanosensing. For example, in contrast to sclerostin down-regulation that is typically seen with loading in younger mice[21, 25], osteocytes in aged mice show persistent expression of sclerostin under mechanical loading[28]. This diminished ability to translate mechanical loads through relevant protein production could explain the diminished osteogenic response to load in older mice that has been demonstrated by several groups[11, 29, 30]. Nevertheless, real-time data of the aged osteocyte network's ability to respond to mechanical load is lacking.

Decline in bone mass with age ultimately presents itself as osteoporosis, a disease that resulted in more than 2 million osteoporotic fractures in the United States in 2015[31]. One treatment for osteoporosis approved by the U.S. Food and Drug Administration in 2019 utilizes an antibody targeting sclerostin, the protein primarily produced by osteocytes to inhibit osteoblast activity and bone formation. Treatment with antibodies to sclerostin (Scl-Ab) in

preclinical animal models results in increased bone formation and decreased bone resorption[32], ultimately leading to a rapid increase in bone mass, bone mineral density (BMD) and bone strength. In clinical trials, Scl-Ab has been shown to rapidly increase bone mineral density and decrease the incidence of osteoporotic fractures[33, 34]. However, the effects of this treatment have also been shown to be dampened with repeated, long-term administration in both animal and human studies[35-37]. It is hypothesized that the altered mechanical environment of the bone due to increased bone formation may be influencing the osteocyte ability to respond to load, but there is no evidence of this to date.

1.1.4 Calcium signaling in osteocytes

Bone cells respond to physical stimuli with numerous biochemical signaling events, one of the earliest being a peak in intracellular calcium (Ca^{2+}) [38, 39]. This response was first demonstrated in osteoblasts but has also been characterized in osteoclasts and their hematopoietic precursors[40, 41]. Interestingly, the characteristics of Ca^{2+} signaling in osteoblast-like cells have been shown to be dependent upon fluid flow profile, mechanical loading frequency, and magnitude of shear stress[42, 43]. This prompted the investigation of Ca^{2+} signaling in osteocytes in an effort to elucidate potential mechanotransduction mechanisms.

Early studies of Ca^{2+} signaling in osteocytes relied on mechanical stimulation of single cells. In one particular model, a localized mechanical stimulus was applied to a single osteocyte using a glass microneedle, which induced site-specific calcium responses between the cell processes and cell body[44]. Studies utilizing fluid flow stimulation show changes in intracellular Ca^{2+} that are well-correlated with individual cell strain[45]. Experimental procedures have since shifted to utilizing osteocyte cell networks to recapitulate *in vivo* configuration and connectivity. Osteocytes in micropatterned networks show highly repetitive spike-like Ca^{2+} peaks under fluid

flow stimulation, which are sustained throughout the entire stimulation period. These osteocyte networks are more sensitive to fluid flow stimulation than similarly-formed networks of osteoblasts[46], and the Ca^{2+} responses are more pronounced under steady than oscillatory flow[47]. Similar means have been used to investigate the intracellular mechanisms underlying the initiation and sustainment of these Ca^{2+} oscillations under fluid flow[48].

Since osteocytes regulate bone remodeling by sensing the micromechanical environment induced by bone matrix deformation, it is favorable to study potential mechanosensing mechanisms in conditions that are as close to *in situ* as possible[49]. Many studies have utilized *ex vivo* whole-bone models of osteocyte mechanosensing, which maintain the stellate morphology of the osteocyte network in its surrounding native bone matrix. These models are used in combination with fluorescent microscopy techniques to observe the real-time Ca^{2+} response of bone cells to mechanical stimuli, including bone matrix deformation[50] and fluid shear over bone fragments[51]. One model in particular was developed to confirm the differences in Ca^{2+} signaling between osteocyte and osteoblast networks, demonstrating that native osteocytes within the bone matrix exhibit robust Ca^{2+} oscillations in response to physiological whole-bone loading, which are more robust than under autonomous conditions and more distinct than those of osteoblast cells on the bone surface[19]. These load-induced Ca^{2+} oscillations presented the same peak characteristics as previously observed in *in vitro* osteocytes under fluid flow[46-48], confirming this phenomenon in native osteocytes. Additionally, the responsive characteristics of osteocytes are enhanced with increasing mechanical load magnitude, presenting a real-time measure of osteocyte mechanosensitivity *in situ* in response to *ex vivo* long bone mechanical loading.

1.2 Motivations

Ca^{2+} signaling as an indicator of real-time osteocyte mechanosensitivity has yet to be translated to clinical contexts, such as in aging or osteoporosis treatment. Such a robust response in what is considered to be the primary mechanosensitive cell type in bone has the potential to uncover factors contributing to altered bone formation responses in these cases. Additionally, while Ca^{2+} oscillations in osteocyte networks have been confirmed in experimental systems of multiple scales, the exact function of this immediate response to load remains unclear. Specifically, the downstream consequences of Ca^{2+} signaling of osteocytes in their native bone matrix have yet to be observed and characterized, as well the mechanosensitive potential of these downstream functions.

1.3 Aims and Organization

The goal of this work is to enhance understanding of osteocyte mechanotransduction and how osteocyte mechanosensitivity may be altered in contexts related to bone disease pathologies. The studies presented in this thesis are based on an *ex vivo* murine tibia model of real-time osteocyte Ca^{2+} signaling in response to whole bone loading (Figure 1.3)[19].

In the first study presented in Chapter 2, we utilized the mechanosensitive properties of Ca^{2+} signaling in the osteocyte network to determine the effect of age on osteocyte mechanotransduction by comparing responses to mechanical load between young-adult mice and aged mice. We hypothesized that a loss of mechanosensitivity in the osteocyte network will be exhibited by a reduction in Ca^{2+} signaling responses under whole-bone mechanical loading of tibia from aged mice. This hypothesis was explored through the following aim:

> **Specific Aim 1:** Characterize and compare real-time Ca^{2+} signaling profiles of the *ex vivo* osteocyte network from mature adult and old mice in response to mechanical loading.

In the next study presented in Chapter 3, osteocyte mechanosensitivity was further investigated in the context of Scl-Ab treatment, which has recently been approved as a new therapy for osteoporosis. We hypothesized that bone formation responses to long-term treatment with Scl-Ab diminishes the Ca^{2+} signaling response in *ex vivo* osteocytes to mechanical load due to the alteration of the mechanical environment. Osteocyte mechanosensitivity was characterized in tibiae from mice treated with Scl-Ab or vehicle through the following Specific Aims:

> **Specific Aim 2a**: Compare real-time Ca^{2+} signaling profiles under load-matched mechanical stimulation of *ex vivo* osteocytes from mice that received either short- or long-term treatment with Scl-Ab or vehicle.
>
> **Specific Aim 2b**: Compare real-time Ca^{2+} signaling profiles under strain-matched mechanical stimulation of *ex vivo* osteocytes from mice that received either short- or long-term treatment with Scl-Ab or vehicle.

In Chapter 4, we investigated the functional consequences of load-induced Ca^{2+} oscillations in osteocytes by expanding upon the established *ex vivo* model to quantify intracellular actin network dynamics. We hypothesized that osteocytes exhibit Ca^{2+}-dependent actomyosin contractions in their native bone matrix in response to mechanical loading, and that these contractions also demonstrate mechanosensitive properties. The work in this chapter was guided by the following Specific Aims:

> **Specific Aim 3a:** Simultaneously image real-time Ca^{2+} and actin network dynamics of live osteocytes in their native bone matrix in response to biochemical and mechanical stimuli using an *ex vivo* murine tibiae model.
>
> **Specific Aim 3b:** Quantify Ca^{2+}-dependent actomyosin contractions in *ex vivo* osteocytes in response to different magnitudes of physiological mechanical loading of whole tibiae.

Chapter 5 summarizes the conclusions of these studies, suggests future work to expand on these findings, and outlines the significance of this body of work.

1.4 Figures

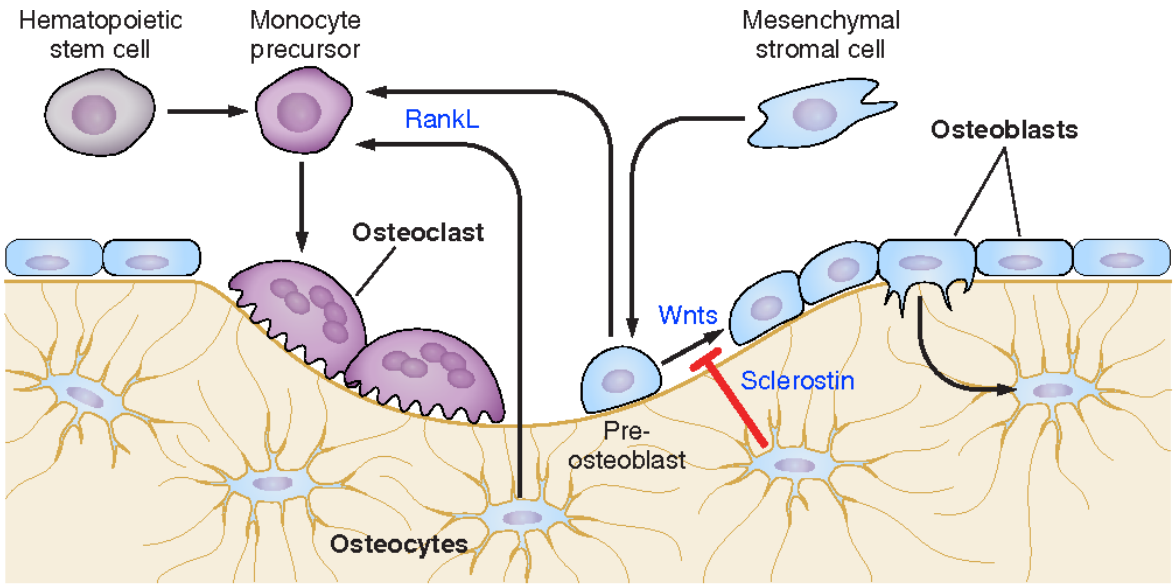

Figure 1.1 Major cell types in bone. The resorption and formation of bone is spatially and temporally coordinated by three major cell types. Osteoclasts are derived from hematopoietic stem cells which differentiate and fuse into multi-nucleated bone-resorbing cells. Bone is synthesized and mineralized by osteoblasts either in concert with (remodeling) or distinct from resorption (modeling). A proportion of mature osteoblasts further differentiates into osteocytes as they become embedded in the bone matrix they produce. Osteoblast and osteoclast activity are influenced by osteocyte production of sclerostin and RANKL, respectively. Given their role in transducing mechanical stimuli to promote bone formation and resorption processes, osteocytes are considered the primary mechanosensory cell type in bone. *Image credit: Riddle RC, Clemens TL. Bone Cell Bioenergetics and Skeletal Energy Homeostasis. Physiol Rev. Apr 2017;97(2):667-98. Epub 2017/02/17.*

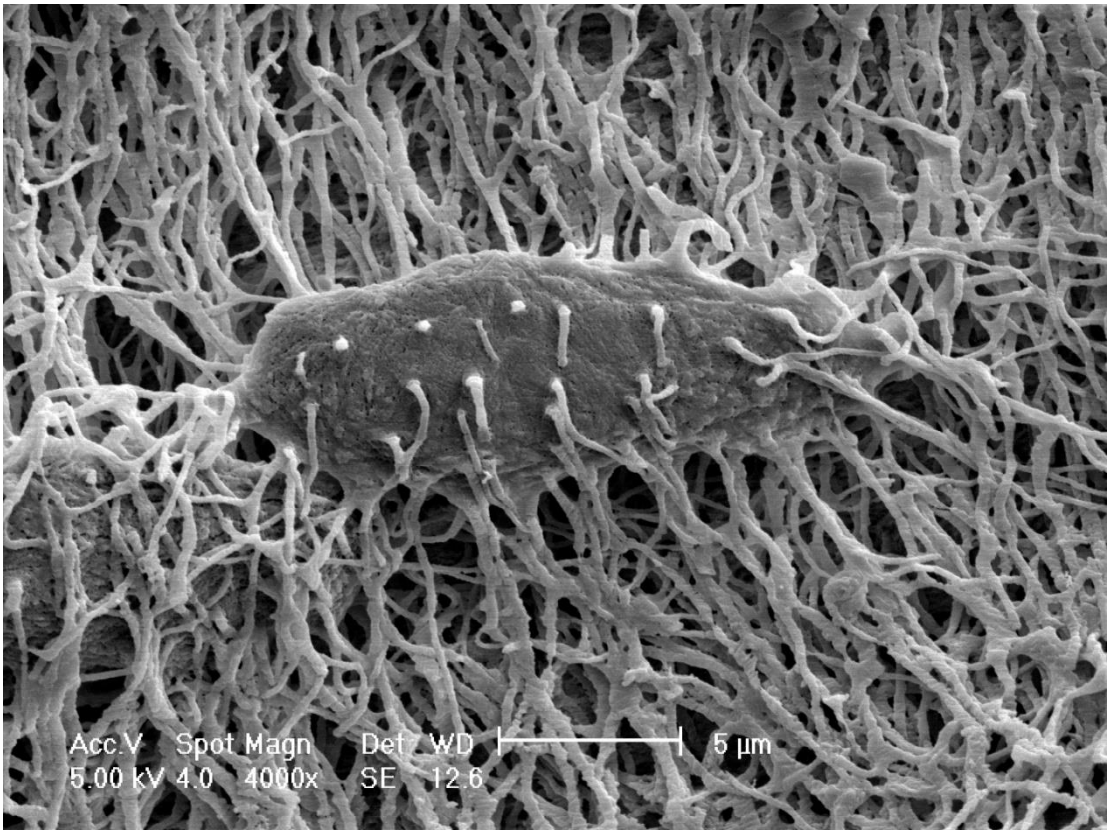

Figure 1.2 Scanning electron micrograph of an osteocyte in resin. Osteocytes exist as stellate cells embedded in the bone matrix, interconnected throughout the tissue via extensive dendritic processes. *Image credit: Lynda Bonewald.*

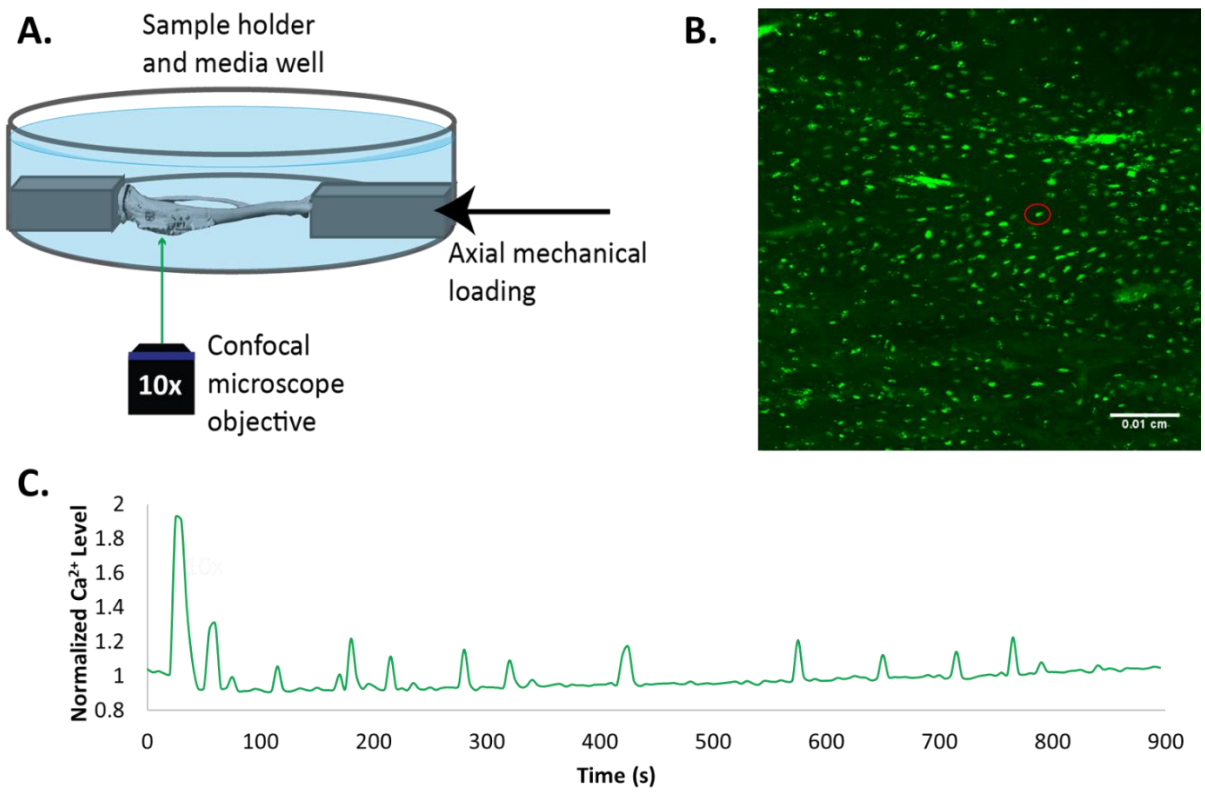

Figure 1.3 *Ex vivo* model of osteocyte Ca^{2+} signaling. A. Mouse tibiae are dissected and transferred to a custom mechanical loading system, where cyclic compressive loads are applied to the distal end of the whole bone while live osteocytes are imaged using confocal microscopy. **B.** The intracellular Ca^{2+} indicator Fluo-8 AM is incubated with tibia samples to allow for imaging of Ca^{2+} dynamics in live osteocytes over time in response to mechanical and biochemical stimuli. **C.** Fluo-8 intensity is normalized to baseline intensity and plotted over time for individual osteocytes (**B**, red oval). Peaks in intracellular Ca^{2+} are identified and characterized in response to cyclic mechanical loading.

Chapter 2: Mechanosensitive Calcium Signaling and Coordination in Osteocytes of Aged Mice

2.1 Introduction

Aging is one of the most important factors in determining the likelihood of developing osteoporosis[52, 53], a systemic disease characterized by low bone mass and microarchitectural deterioration of bone tissue with a consequent increase in bone fragility and susceptibility to fracture. Age-related changes in bone include trabecular perforation, thinning, and loss of connectivity, as well as cortical thinning and increased porosity[54], along with possible changes in the bone composition itself[55]. Osteoporotic reduction in skeletal mass is caused by an imbalance between bone resorption and bone formation[53], hinting at dysfunction of how osteocytes direct remodeling processes.

At the cellular level, it has been shown that aging adversely affects the integrity and morphology of the mechanosensing osteocyte network[56]. Methods such as acid-etching and scanning electron microscopy of resin-embedded bone reveals lower lacunar density and a reduction in canaliculi per lacuna within the bone matrix in both aged animals[57] and humans[27, 58], suggesting degradation of the connectivity of the cellular network. Most recently, confocal imaging modalities have allowed for comprehensive analysis of osteocyte cell morphology directly[59], in addition to properties of the lacunar-canalicular system (LCS) in which the cells reside[60]. Multiplexed-3D-confocal imaging of murine osteocytes reveals a dramatic reduction in osteocyte dendrite number and cell density, particularly in female mice where osteocyte dendricity decreases linearly with age and correlates significantly with cortical bone changes[59]. Given the crucial role of the osteocyte network in sensing and translating mechanical loads, it is

plausible that diminished connectivity of this cellular network could adversely affect short-term mechanotransduction processes driving long-term bone adaptation.

Impaired osteocyte sensitivity with age has been most commonly demonstrated in tissue-level analyses of bone formation in response to mechanical load. Micro-computed tomography (micro-CT) analysis reveals a suppression of the typical osteogenic response to mechanical loading, albeit still present, demonstrated by a greater accrual of cortical bone in young-adult compared to aged mice[61-63]. Early histomorphometry data suggests this suppressed response corroborates with reduced periosteal bone formation rate and bone forming surfaces in aged turkeys[29] and rats[30] compared to younger animals. In mice, this periosteal bone formation rate is 65-70% lower in old animals compared to young-adult animals loaded at equivalent peak strain[61]. At a cellular level, the reduced bone formation response of aged mice to loading may be due to the inability of aged osteocytes to sustain Wnt activity, which is required for optimal bone formation induced by repeated loading[28]. While these studies provide evidence for long-term effects of aging on tissue-level responses to mechanical loading, it is still unclear how aging directly affects the osteocyte network ability to immediately sense and transduce mechanical loads to influence long-term responses.

Early *in vitro* cell studies investigating bone cell responsiveness utilized human bone cell cultures from aged, osteoporotic donors. These studies focused on early release of prostaglandin E2 (PGE2), prostaglandin I2 (PGI2), nitric oxide, and transforming growth factor-beta (TGF-beta) in response to pulsating fluid flow and showed little to no effect of age on these responses[64, 65]. Another early biological response to physical stimuli in bone cells is a peak in intracellular calcium (Ca^{2+})[38], of which age has been shown to have a diminishing effect in rat osteoblastic cells[42]. However, the mechanosensitive potential of early Ca^{2+} responses in aged

osteocytes has yet to be investigated. Indeed, it has been shown that osteocyte networks *in vitro* demonstrate highly repetitive spike-like Ca^{2+} peaks under fluid flow stimulation, which are dramatically different from those in osteoblastic networks[46]. Recapitulating this phenomenon at a tissue-level scale, native osteocytes exhibit robust Ca^{2+} oscillations in response to physiological whole-bone loading, which are enhanced with increasing mechanical load magnitude and thus serve as a real-time measure of osteocyte mechanosensitivity *in situ* in response to whole bone mechanical loading[19]. Therefore, we hypothesize that impairment of mechanosensitivity in the aged osteocyte network will be exhibited by diminished Ca^{2+} signaling responses under mechanical loading, much akin to the age-related blunted protein expression and subsequent dampened bone formation responses shown by other groups.

2.2 Materials and Methods

2.2.1 Aged and young-adult mice

Female C57BL/6JN inbred mice at 5 and 22 months of age, corresponding to young-adult and old age in humans, respectively [66], were purchased from the National Institute of Aging aged rodent colony (NIA, Bethesda, MD, USA) managed by Charles River Laboratories (Wilmington, MA, USA) in collaboration with Dr. Matthew J. Silva (Department of Orthopaedic Surgery, Musculoskeletal Research Center, Washington University, St. Louis, MO, USA). Animals were housed 3-5 per cage and given access to food and water *ad libitum* (PicoLab 5053 and 5058, LabDiet, St. Louis, MO, USA). All animal procedures were approved by the Institutional Animal Care and Use Committee at Columbia University in accordance with Institute for Comparative Medicine and national guidelines.

2.2.2 Osteocyte intracellular Ca^{2+} imaging

Mice were sacrificed by CO_2 inhalation and bilateral tibiae were immediately dissected under sterile conditions. Tibiae were maintained in supplemented cell culture media (αMEM + 5% calf serum, 5% defined fetal bovine serum) and incubated at 37°C, 5% CO_2 for 2 hours. Tibia samples were then incubated with Ca^{2+} indicator Fluo-8 AM (AAT Bioquest, Sunnyvale, CA, USA) dissolved in 20% Pluronic F-127 in DMSO (Invitrogen, Carlsbad, CA, USA) for 45-60 minutes, washed, and post-incubated for 10 minutes before being transferred to a custom mechanical loading device for simultaneous loading and imaging. For experiments using 5-month-old and 22-month-old Dmp1-Cre;Ai38$^{flx/flx}$ mice, which inherently express the GCaMP3 Ca^{2+} indicator in osteocytes, tibiae were similarly dissected and maintained in supplemented media before being immediately placed in the custom mechanical loading device.

Using an Olympus FluoView FV1000 laser scanning confocal microscope with a 10x objective (Olympus, Waltham, MA, USA), Fluo-8 AM-dyed or GCaMP3-expressing osteocytes were visualized 20-30 μm below the anteromedial cortical bone surface of either the right or left tibiae, depending on baseline signals in the cells. Ca^{2+} indicators were excited at 473 nm and fluorescence emissions were collected at 520 nm. Kalman filtering was applied during imaging with an acquisition time of 2.218 s/frame. Depending on the distribution of Fluo-8 AM dye-loading and baseline cell signals, time-lapse images were recorded for n=6-8 tibiae/age group (Table 2.1). For Dmp1-Cre;Ai38$^{flx/flx}$ mice, images were recorded for 5 tibiae/age group.

2.2.3 Whole-bone mechanical loading

Confocal time-lapse images were synchronized with a rest-inserted mechanical loading protocol to eliminate out-of-focus motion artifacts resulting from deformation of the bone

sample, with images being acquired every 5 seconds for 900 seconds total[19]. Five baseline images were acquired before mechanical loading was initiated via a trigger from the FluoView software to a 16-bit data acquisition (DAQ) card (NI USB-6210) and LabView VI (National Instruments, Austin, TX, USA). Samples were maintained in supplemented cell culture media while cyclic mechanical loads were applied along the long axis of the whole bone using a custom-designed system[19]. A pre-load of 2 N was applied, followed by cyclic axial loading of 1 Hz triangle waveforms with 4 s rest-insertion after each cycle to allow for confocal image acquisition. Load magnitudes of 10.2 N and 8.3 N were applied to the 5-month-old and 22-month-old tibiae respectively, corresponding to anteromedial surface strain of 1500 $\mu\varepsilon$[67].

2.2.4 Osteocyte image analysis

Translation motion artifacts were removed using the StackReg image registration algorithm in ImageJ (U.S. National Institutes of Health; Bethesda, MD, USA). Cell bodies were manually traced using MetaMorph 7.0 (Molecular Devices, Downingtown, PA, USA), and the average Ca^{2+} indicator intensity of the cell body was extracted as a function of time. Using MATLAB 2014b (The MathWorks, Natick, MA, USA), the average pixel intensity of each individual cell was normalized by the average of corresponding baseline frames, and a Ca^{2+} peak was identified as a transient increase to 3 times the standard deviation of baseline intensity of each cell. The percentage of responsive cells ($\geq$ 1 peak) of all Fluo-8 AM-dyed or GCaMP3-expressing cells, average number of Ca^{2+} peaks exhibited by responsive cells, average Ca^{2+} peak magnitude, and average time to the first Ca^{2+} peak following initiation of mechanical loading were quantified for each tibia sample[19, 46, 47]. Ca^{2+} signaling in two osteocytes was considered synchronous if the time between the any of the peaks from each cell was less than 15 seconds[68]. Synchrony between cells was evaluated in a pair-wise manner for all cells in the field of view

(FOV). The number of synchronous cell pairs was normalized by all cell pairs in the FOV for each tibia sample.

2.2.6 Osteocyte network visualization

Tibia samples from 5-month-old and 22-month-old mice were fixed in 10% formalin for 48 hours before being transferred to 70% ethanol (n=5/group). Samples were then incubated with 100 μM Vybrant DiI (Thermo Fisher Scientific, Waltham, MA, USA) in 100% ethanol for 24 hours before imaging with confocal microscopy [69]. Images of the stained osteocyte cell membranes were taken in the approximate region of *ex vivo* osteocyte Ca^{2+} signalling, 20-30 μm below the anteromedial bone surface using confocal microscopy.

2.2.5 Micro-computed tomography scanning and analyses

Cortical bone morphological parameters of *ex vivo* frozen tibia samples were assessed via micro-computed tomography (micro-CT) using a Scanco VivaCT 80 system (Scanco Medical AG, Brüttisellen, Switzerland). Scanning parameters were 55 kVp energy, 109 μA intensity, and 300 ms integration time; reconstructed images had 5.0 μm isotropic voxel size. Prior to all analyses, a Gaussian filter was applied (sigma = 0.8, support = 1) to reduce noise. The cortical region of interest was set at 2.0 mm in length, centered midway between the tibial plateau and the distal tibiofibular junction. Global thresholds of 40% of the maximum gray scale value were used to classify cortical bone. Standard Scanco evaluation software was used to calculate cortical thickness (Ct.Th) in a subset of the experimental C57BL/6N mice tibia samples (n=4-5/group).

2.2.7 Statistics

All data are presented as mean ± standard deviation. Student's t-test was used to determine significant differences in cortical thickness, osteocyte responsive percentage, Ca^{2+} peak number, Ca^{2+} peak magnitude, and time to 1st peak between samples from 5-month-old and

22-month-old mice. To determine the correlation between synchronous cell pair number and cell-cell distance, a linear regression analysis was performed. Statistical significance is observed when $p<0.05$.

2.3 Results

2.3.1 Age-related changes in *ex vivo* mouse tibiae

22-month-old mice exhibited age-related bone loss as shown by micro-CT imaging of the cortical bone (Figure 2.1 A). Aged mice had significantly thinner cortical bone (0.102 ± 0.003 mm) compared to young-adult 5-month-old mice (0.151 ± 0.019 mm) at the time of sacrifice for Ca^{2+} imaging experiments (Figure 2.1 B). Fixed osteocyte networks of aged mice exhibited a lower cell density and diminished dendricity compared to networks of young-adult mice, suggesting compromised connectivity (Figure 2.2).

2.3.2 Ca^{2+} signaling is diminished in osteocytes of aged mice during tibial loading

Time-lapse Ca^{2+} signaling analysis was performed for 362 and 182 individual osteocytes dyed with Fluo-8 AM from 5-month-old and 22-month-old mice tibiae, respectively (Table 2.1). In 5-month-old mice, 34.6 ± 9.9% of osteocytes responded to mechanical loading with an average of 3.1 ± 0.9 Ca^{2+} peaks per responsive cell in the 900 s loading/imaging period. In 22-month-old mice, the percentage of responsive cells decreased significantly to 13.6 ± 5.0% of cells in the FOV (Figure 2.3, Figure 2.4 A). Despite few responding cells in the aged mice samples, the average number and intensity of Ca^{2+} peaks in response to mechanical load were not significantly different between age groups (Figure 2.4 B, C). Ca^{2+} signaling characteristics were comparable between Dmp1-Cre;Ai38$^{flx/flx}$ osteocytes and age-matched Fluo-8 AM-dyed osteocytes under the same loading conditions (Figure 2.5).

2.3.3 Osteocyte networks from aged mice lack coordination of Ca^{2+} signaling between cell pairs

In young-adult mice, responding cells initiated Ca^{2+} signaling 163.6 ± 72.3 seconds following loading initiation. By comparison, the initiation of Ca^{2+} signaling was delayed significantly in the osteocytes of aged mice (Figure 2.3, Figure 2.4 D), with the first Ca^{2+} peak occurring 326.7 ± 113.9 seconds following the start of cyclic mechanical loading. Synchrony analysis of Ca^{2+} signaling between all cell pairs in the FOV revealed a strong negative correlation (R^2=0.97) between cell-cell distance and number of synchronous cell pairs in 5-month-old osteocytes (Figure 2.6). This correlation was absent in 22-month-old osteocyte networks, with fewer total synchronous cell pairs (10 pairs) compared to 5-month-old osteocyte networks (442 pairs).

2.4 Discussion

The study of osteocytes in explanted bone tissue models allows for preservation of the native 3D network and connectivity, which are both unique and functionally relevant to this mechanosensing cell type. The nature of the intracellular osteocyte network can be influenced by mechanical environments[70] and disease pathologies. For instance, osteocyte connectivity is shown to be compromised with aging [59], which we observed in our own samples via cell membrane staining in fixed tibiae. The *ex vivo* model of osteocyte Ca^{2+} signaling allows us to directly study live cells in their native networks in whole-bone samples from animals affected by age-related bone loss, as confirmed by micro-CT. Thinning of the cortical bone with age motivated our selection of strain-matched mechanical load levels between age groups[67], such that the biological effects of aging on osteocyte network mechanosensitivity were captured rather than the effect of disparities in mechanical environment due to age-induced bone loss.

Additionally, the study of cortical osteocytes allowed us to capture mechanosensitive Ca^{2+} signaling in strain-matched areas, as opposed to in trabecular bone, where experimentally determining the mechanical loading environment proves to be challenging[61].

This study is the first to compare real-time mechanosensitive Ca^{2+} signaling in osteocyte networks from young-adult and old mice. Mechanosensing in the osteocyte network of aged mice was diminished to a significantly lower percentage of responsive cells while characteristics of the peaks themselves, particularly average peak number and average peak intensity, were consistent with those exhibited by osteocytes from young-adult mice. This implies that though there are fewer osteocytes sensitive to the prescribed anteromedial cortical bone strain in aged networks, these cells are responding in a manner comparable to young-adult osteocytes. It is possible that the low number of Fluo-8 dyed osteocytes, nearly half that of 5-month-old mice, is a direct result of the low osteocyte density of old mice. It is also feasible that age-related changes in metabolic processes may have affected Fluo-8 dye uptake between young-adult and aged mice. To address this, we also compared Ca^{2+} responses to mechanical load in osteocytes from young-adult and old Dmp1-Cre;$Ai38^{flx/flx}$ mice, which inherently express the Ca^{2+} indicator GCaMP3 in osteocytes [71, 72]. This data confirms our age-related, Fluo-8 AM-based observations in a mouse model that does not require further manipulation beyond dissection [73]. Taken together, our signaling data is in agreement with previous work suggesting that that there is a partial, but not complete loss of cortical mechanoresponsiveness with aging [62]

In a prior study of Ca^{2+} oscillations in aged bone cells, Donahue and colleagues demonstrated that osteoblastic cells isolated from old rats were less responsive to fluid flow in with a lower percentage of responsive cells, while the magnitude of fluid flow-induced Ca^{2+} oscillations was not significantly affected by age[42]. Our findings are consistent with these results

in that osteocyte networks from 22-month-old mice yield a lower percentage of responsive cells with a magnitude of responses not significantly different from that of 5-month-old mice. While the stimulus for mechanosensation in both studies is fluid flow, the current study utilizes axial whole-bone mechanical loading to induce physiological fluid flow in the LCS. Additionally, one key advantage of our study is our ability to study the responses of primary osteocytes *in situ* where the unique morphology of individual osteocytes and their extensive intercellular network are maintained. Indeed, this intercellular connectivity has been shown to have implications in mechanoresponsiveness to mechanical loading and signal transduction by work investigating the role of gap junction channel proteins in bone mechanostransduction[74].

In analyzing the characteristics of the Ca^{2+} peaks from individual osteocytes, we uncovered a delay in initiation of Ca^{2+} signaling in 22-month-old mice, suggesting an apparent randomness in Ca^{2+} responses of aged osteocytes. This motivated us to further investigate the synchrony of Ca^{2+} signaling between osteocytes in their native networks.. Micro-patterned MLO-Y4 cell networks *in vitro* have been shown to demonstrate high spatial intercellular synchronicity of Ca^{2+} oscillations in response to fluid flow, which is negatively correlated with intercellular distance[68]. Indeed, synchronous cell pair number decreased linearly with increasing cell-cell distance in osteocyte networks in 5-month-old mice tibiae. However, in old mice, our findings show that osteocyte networks exhibit an impaired ability to generate coordinated Ca^{2+} signaling. Reduction in osteocyte dendricity and cell density with age, particularly in females[59], may be responsible for the lack of intercellular signaling coordination. Notably, there were more osteocytes within the field of view available for analysis in 5-month-old versus 22-month-old mice, an observation that limits our study of cell-cell synchrony and warrants further

investigation. To account for this absolute difference, the number of responsive cells was normalized to all cells in a field of view for each tibia sample.

Future studies investigating rescue or enhancement of Ca^{2+} signaling in aged osteocyte networks will provide further insight to the mechanisms that are responsible for the diminished mechanosensing that we observe. Previous work has demonstrated the dominant role of ATP in mediating intercellular Ca^{2+} propagation from a single nanoindented bone cell to neighboring cells in a micropatterned network [75, 76], as well as intracellularly from the osteocyte process to the cell body [77]. Furthermore, inhibition of the ATP-related signaling pathway reduces the number of Ca^{2+} oscillations as well as the percentage of osteocytes responding to mechanical stimulation [19, 46, 78]. Therefore, agonists for receptors for the purnergic pathway may enhance ATP diffusion between neighboring cells in the osteocytic network and may promote spatial intercellular coordination of Ca^{2+} events in aged osteocytes. However, if age-related degradation of the osteocyte network is indeed responsible for diminished coordination of Ca^{2+} signaling in the osteocyte network, then agonists for pathways upstream of Ca^{2+} signaling may have little effect on cell-cell synchrony. In this case, future studies may then be best focused on the influence of osteocyte network integrity on Ca^{2+} responses to load. This could be achieved through overexpression of gap junction-related proteins, as with an osteocyte Cx43 overexpression model in which age-induced cortical bone changes were ameliorated by preserving osteocyte viability and maintaining bone formation [79]. It also would be of interest to computationally model possible changes in the fluid flow of the LCS, considered to be the primary mechanical stimulus in osteocyte mechanotransduction [16, 17], as a result of reduced cell density and dendricity in aged osteocyte networks.

2.5 Conclusions

The primary goal of this study was to utilize intracellular Ca^{2+} signaling to investigate the mechanosensitive capabilities of osteocytes from young-adult and old mice. By comparing the peak characteristics of Ca^{2+} oscillations of osteocyte networks from young-adult and old mice under tibial loading, we uncovered that mechanosensing in the osteocyte network of aged mice is diminished to a smaller percentage of cells with similar signaling characteristics as young-adult mice. We also show that osteocyte networks of aged mice exhibit an impaired ability to generate coordinated Ca^{2+} signaling. This compromised mechanosensing has implications for downstream bone cell signaling and may ultimately influence long-term bone formation processes that are impaired with aging.

2.6 Tables

	5-month-old	22-month-old
Tibia Samples	8	6
Osteocytes	362	182

Table 2.1 Experimental tibia samples and osteocytes dyed with Fluo-8 AM for analysis. Ca^{2+} signaling in tibial osteocytes of 5-month-old (young-adult) and 22-month-old (aged) mice were analyzed under strain-matched loading conditions. The number of tibia samples and osteocytes analyzed depended on the success of Fluo-8 intracellular Ca^{2+} dye-loading and baseline cell signals.

2.7 Figures

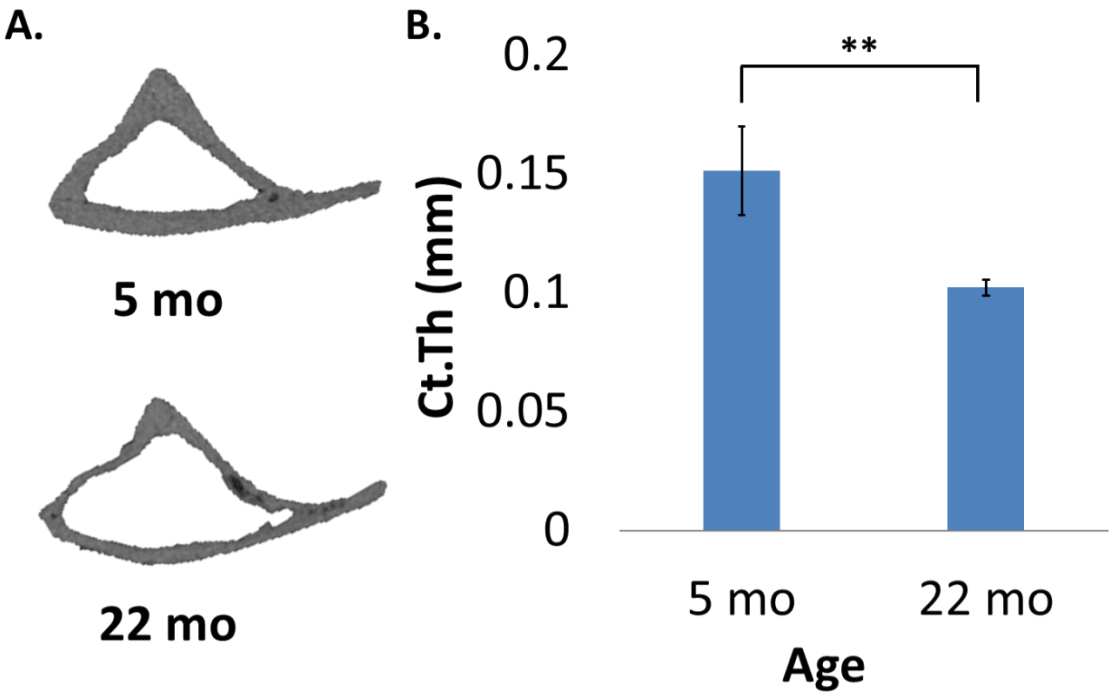

Figure 2.1 Age-induced changes in cortical bone of old mice. A. Representative *ex vivo* micro-CT cross sections of tibial cortical bone in 5-month-old and 22-month-old female mice show decreased cortical thickness (Ct.Th) in the aged mice compared to young-adult. **B.** Average Ct.Th was calculated for the aged (n=4) and young-adult (n=5) tibia samples. Data are mean ± SD. **p<0.01 (Student's t-test)

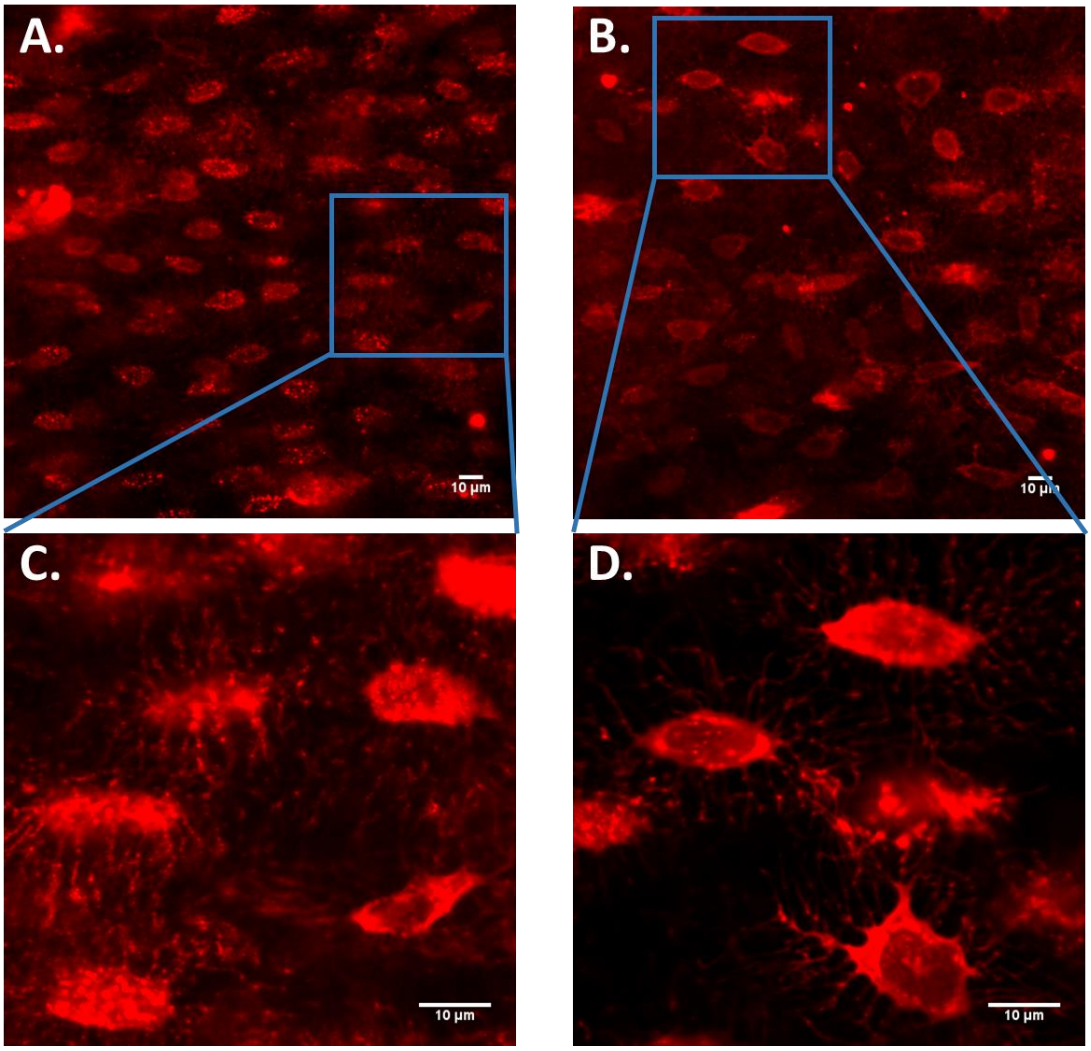

Figure 2.2 Age-induced changes in osteocyte network morphology. Fixed *ex vivo* osteocyte membranes are stained with DiI and imaged with confocal microscopy. Representative images are provided for cell networks from tibiae of 5-month-old (A, C) and 22-month old (B, D) mice.

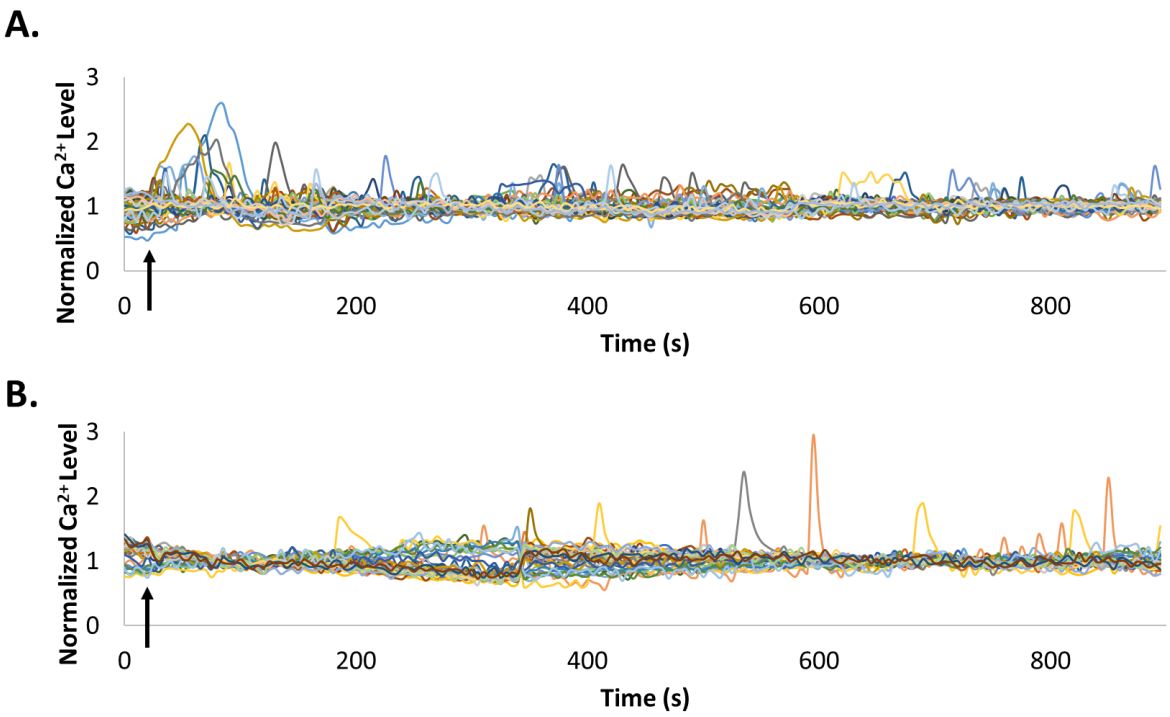

Figure 2.3 Representative Ca^{2+} traces for young-adult and aged *ex vivo* osteocytes. Average Fluo-8 AM intensity normalized by average baseline intensity prior to load is plotted over time for all osteocytes in the field of view of a given **A.** 5-month-old mouse tibia (n=53 cells) and **B.** 22-month-old mouse tibia (n=32 cells). Cyclic mechanical loading was initiated at t=25 s (arrows). Ca^{2+} peaks in each individual cell are defined as spikes in intensity that are greater than 3 times the standard deviation of the baseline intensity for that cell.

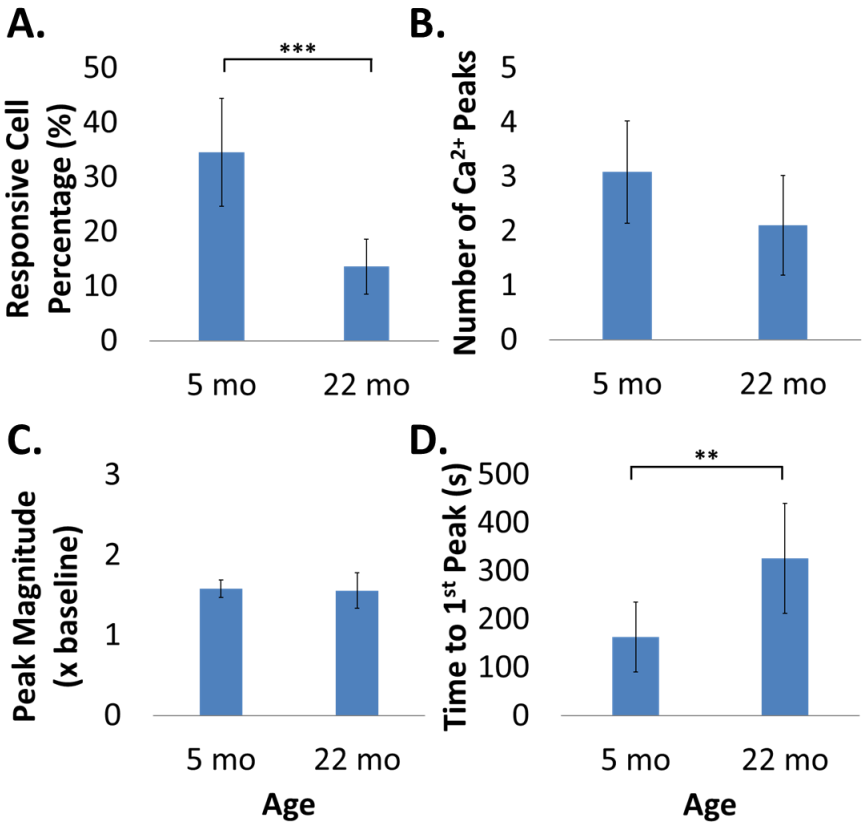

Figure 2.4 Load-induced Ca^{2+} signaling parameters in young-adult and aged osteocytes dyed with Fluo-8 AM. Based on Ca^{2+} peak identification from all Fluo-8 dyed osteocytes in the field of view (FOV) from 5-month-old (n=8 tibiae) and 22-month-old mice (n=6 tibiae). **A.** Percentage of responsive osteocytes (those that exhibit $\geq$ 1 Ca^{2+} peak) of all cells in the FOV. **B.** Number of intracellular Ca^{2+} peaks exhibited by responsive osteocytes. **C.** Magnitude of Ca^{2+} peaks relative to baseline Fluo-8 AM intensity. **D.** Time between initiation of mechanical loading and Ca^{2+} signaling. Data are mean ± SD. **p<0.01, ***p<0.001 (Student's t-test).

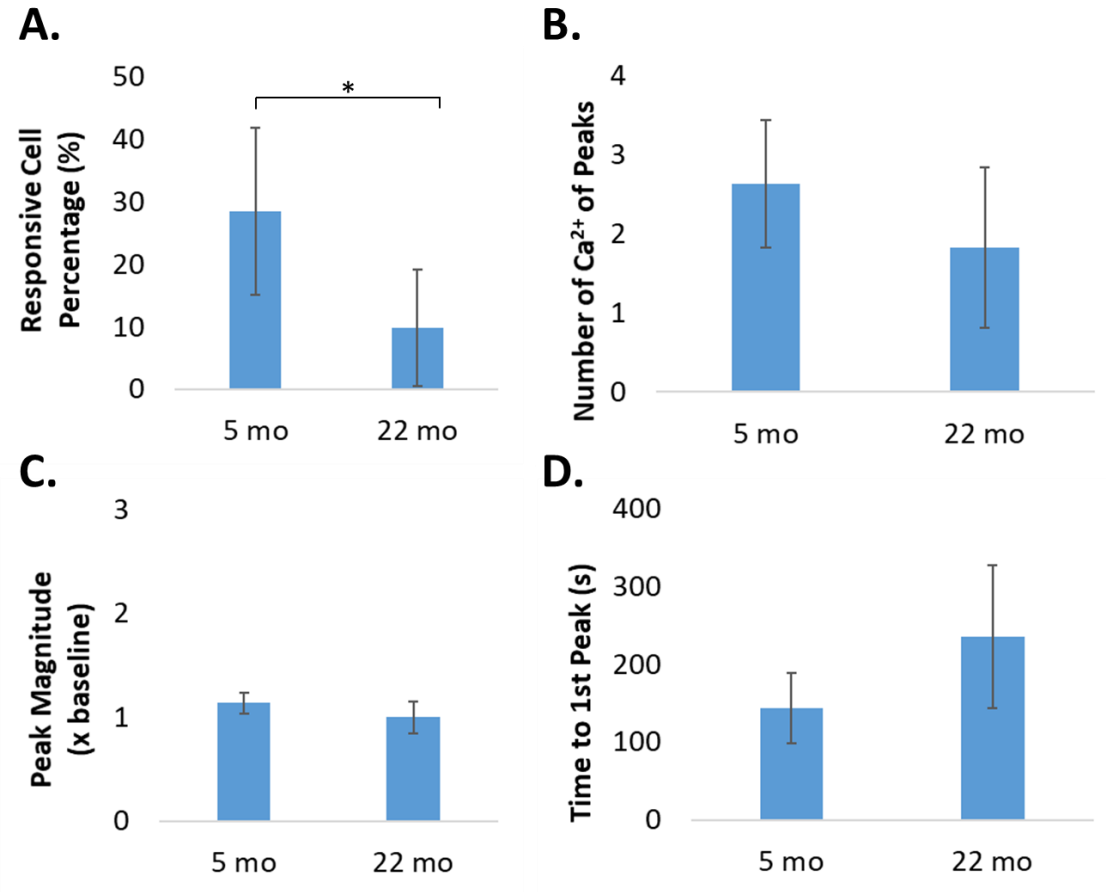

Figure 2.5 Load-induced Ca^{2+} signaling parameters in young-adult and aged osteocytes of Dmp1-Cre;Ai38$^{flx/flx}$ murine tibiae. A. Percentage of responsive of all cells in the FOV. B. Number of intracellular Ca^{2+} peaks exhibited by responsive osteocytes. C. Magnitude of Ca^{2+} peaks relative to baseline Fluo-8 AM intensity. D. Time between initiation of mechanical loading and Ca^{2+} signaling. n=5 tibiae/group. Data are mean ± SD. *p<0.05 (Student's t-test).

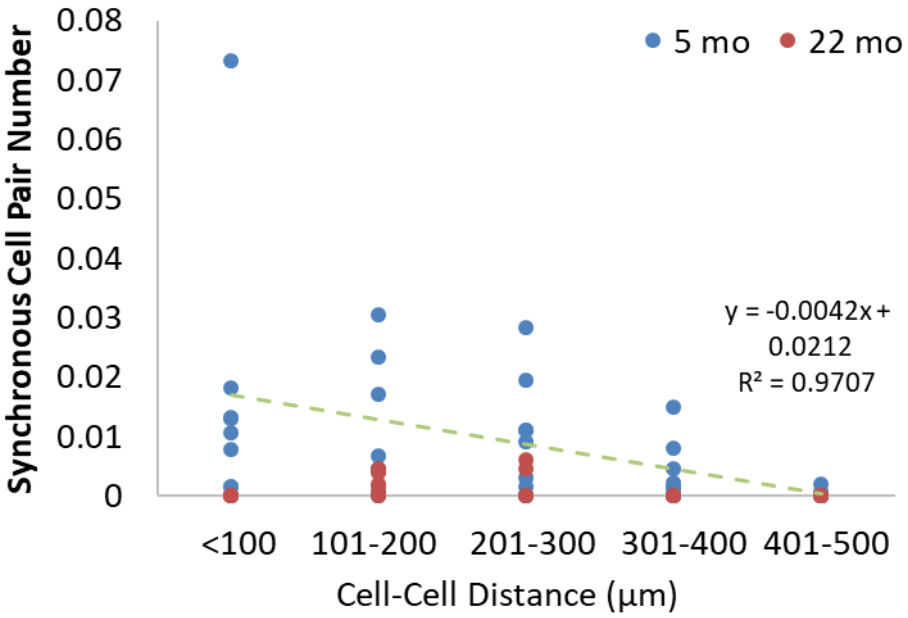

Figure 2.6 Ca^{2+} peak synchrony in osteocyte networks of young-adult and aged mice. Synchronous cell pairs, in which the time between the any of the Ca^{2+} peaks from each cell in the pair is less than 15 seconds, are totaled and normalized to the total number of cell pairs in the FOV. Data points represent normalized synchronous cell pair numbers according to cell-cell distance for each tibia sample (n=6-8/group). Trend line represents negative correlation between average synchronous cell pairs and cell-cell separation in 5-month-old mice. Data are mean ± SD.

Chapter 3: Osteocyte Mechanosensing Following Short-Term and Long-Term Treatment with Sclerostin Antibody

3.1 Introduction

Osteoporosis is a systemic skeletal disorder characterized by low bone mass with deteriorated tissue microarchitecture, resulting in skeletal fragility and increased risk of fracture. More than 2 million osteoporotic fractures occurred in the United States in 2015[31]. By 2025, fractures and costs associated are projected to reach over 3 million fractures incurring $25.3 billion[80]. Compromised bone mass leading to osteoporotic fracture is the consequence of an unbalanced bone remodeling process, with higher osteoclastic bone resorption than osteoblastic bone formation[81]. Since osteocytes are considered as the primary skeletal mechanosensors responsible for directing bone formation and resorption processes, promising treatments for osteoporosis have been developed to target key bone regulatory proteins produced by osteocytes. One such therapy that has recently received approval by the U.S. Food and Drug Administration is a monoclonal antibody to sclerostin (Scl-Ab), trade name EVENITY™ (romosozumab-aqqg)[82].

Encoded by the *Sost* gene, sclerostin is largely an osteocyte-specific protein[83-85]. Sclerostin binds LRP4/5/6 WNT co-receptors to inhibit WNT signaling[86-88], a pathway which promotes bone formation and indirectly decreases bone resorption[89, 90]. A more detailed understanding of the effects of sclerostin on bone has been gleaned from the study of rare bone diseases such as sclerosteosis and van Buchem disease, both high bone mass disorders resulting from lack of sclerostin expression and, hence, increased bone formation[91]. Mutations of the *Sost* gene in sclerosteosis patients highlighted sclerostin as a potential target in osteoporosis[92, 93], and

prompted preclinical studies using rodent models of genetic deletion or overexpression of *Sost*[94, 95]. In *Sost* knock-out mice, a high bone mass phenotype is presented, characterized by increases in bone mineral density (BMD), bone volume, bone formation, and bone strength[96]. In contrast, transgenic mice overexpressing human *Sost* exhibit a low bone mass phenotype with reduced trabecular bone volume, cortical bone thickness, and decreased bone strength due to significantly reduced bone formation[84]. These studies motivated investigation into the use of antibodies targeting sclerostin to increase bone formation, mass, and strength in patients suffering from osteoporosis.

In both pre-clinical models and patients treated with Scl-Ab, the initial response to treatment is robust. The first published report of pharmacological inhibition of sclerostin demonstrated complete recovery of estrogen deficiency-induced bone loss in rats within three weeks of Scl-Ab treatment[97]. Additionally, treatment of BALB/c mice with Scl-Ab rapidly increases whole body BMD and is accompanied by a significant peak in circulating levels of the bone formation marker N-terminal propeptide of type 1 collage (P1NP) following initial treatment doses[35]. In post-menopausal women, significant percent increases in BMD in lumbar spine and total hip occurred as early as 2 months following biweekly treatment with romosozumab[98]. Furthermore, an increase in P1NP was noted one week after the initial dose of romosozumab was administered, and serum P1NP levels were greatest at one month[33].

While the initial rate of bone formation following Scl-Ab treatment is quite high, histological studies in animal models[37] as well as clinical BMD measures have shown that this rate declines with long-term continuous treatment with Scl-Ab[33]. In multiple animal studies, the magnitude and rate of increase in P1NP is also attenuated upon repeat dosing with Scl-Ab[35, 36, 99]. Clinical trials demonstrate bone formation markers also eventually returning to baseline by six

months with monthly dosing of Scl-Ab, providing further translational confidence in preclinical results [33, 34]. One possible explanation for this return to baseline bone formation response with long-term treatment with Scl-Ab is that osteocytes may be modifying their cellular responses to a new mechanical environment created by initial Scl-Ab treatment; namely increases in bone mass and, therefore, bone stiffness. However, this explanation is speculative without a method of assessing real-time osteocyte mechanosensitivity under Scl-Ab treatment.

As previous work has shown, osteocytes exhibit robust mechanosensitive Ca^{2+} oscillations in response to mechanical stimuli such as fluid flow *in vitro*[46-48, 68] or whole bone mechanical stimulation[19, 73, 100]. In an *ex vivo* murine tibia model, varying strains engendered on the anteromedial cortical bone surface yield differential osteocyte Ca^{2+} signaling characteristics[19]. This model is well-suited to characterize the mechanosensitivity of osteocyte networks *in situ* in mice under various pharmacological treatments or transgenic modifications and would allow us to assess whether changes to the mechanical environment (i.e. increases in bone mass with Scl-Ab treatment) result in changes in osteocyte intracellular Ca^{2+} mechanosignaling. Therefore, we hypothesize that osteocyte Ca^{2+} mechanosensitivity to whole-bone mechanical loading is altered with long-term treatment of Scl-Ab, resulting in self-regulation of the bone formation response as evidenced by diminished rate of increase of BMD and dampened serum P1NP response[35].

3.2 Materials and Methods

3.2.1 Scl-Ab treatment

Scl-Ab or phosphate buffered saline (PBS) vehicle was administered weekly via subcutaneous injections to 12-week-old female BALB/cJ mice (Stock #000651, The Jackson

Laboratory, Bar Harbor, ME, USA) at 25 mg/kg/week per the following groups: vehicle (8 doses of PBS, n=16 mice), long-term treatment (8 doses of Scl-Ab, n=16 mice), or short-term treatment (6 doses of PBS followed by 2 doses of Scl-Ab at Day 42 & Day 49, n=16 mice) (Figure 3.1). Animals were housed 3-5 per cage and given access to food and water *ad libitum* (PicoLab 5053 and 5058, LabDiet, St. Louis, MO, USA). All animal procedures were approved by the Institutional Animal Care and Use Committee at Columbia University in accordance with Institute for Comparative Medicine and national guidelines.

3.2.2 Micro-computed tomography scanning and analyses

Cortical bone morphological parameters of the left tibia of each mouse were assessed biweekly via micro-computed tomography (micro-CT) using a Scanco VivaCT 80 system (Scanco Medical AG, Brüttisellen, Switzerland). Mice were anesthetized via isoflurane inhalation before and during scanning procedures. Scanning parameters were 55 kVp energy, 109 μA intensity, and 300 ms integration time; reconstructed images had 5.0 μm isotropic voxel size. Prior to all analyses, a Gaussian filter was applied (sigma = 0.8, support = 1) to reduce noise. The cortical region of interest was set at 2.0 mm in length, centered midway between the tibial plateau and the distal tibiofibular junction. Global thresholds of 40% of the maximum gray scale value were used to classify cortical bone. Standard Scanco evaluation software was used in the calculation of cortical BMD and cortical thickness.

3.2.3 Serum P1NP detection

Whole blood was collected from the lateral caudal vein of the tail of each mouse using a needle prick at baseline (Day 0), immediately prior to administration of the last two doses of Scl-Ab or PBS (Days 42 and 49), and four days following these time points, at which the peak P1NP levels are observed following dosage of Scl-Ab (Days 4, 46 and 53). Blood was left to clot at

room temperature for 20-30 minutes before being centrifuged at 10,000g for 5 minutes to separate the serum. Levels of serum P1NP at each time point were assessed by enzyme immunoassays in accordance with manufacturer protocols (ImmunoDiagnostic Systems, Fountain Hills, AZ, USA).

3.2.4 Osteocyte intracellular Ca^{2+} imaging

At Day 54, five days following the last treatment injection, mice were sacrificed by CO_2 inhalation and bilateral tibiae were immediately dissected under sterile conditions. Tibiae were maintained in supplemented cell culture media (αMEM + 5% calf serum, 5% defined fetal bovine serum) and incubated at 37°C, 5% CO_2 for 2 hours. Tibia samples were then incubated with Fluo-8 AM (AAT Bioquest, Sunnyvale, CA, USA) dissolved in 20% Pluronic F-127 in DMSO (Invitrogen, Carlsbad, CA, USA) for 45 minutes, washed, and post-incubated for 10 minutes before being transferred to a custom mechanical loading device for simultaneous loading and imaging.

Using an Olympus FluoView FV1000 laser scanning confocal microscope with a 10x objective, Fluo-8 AM dyed osteocytes were visualized 20-30 μm below the anteromedial cortical bone surface of either the right or left tibiae, depending on Fluo-8 AM dye uptake. Fluo-8 AM was excited at 473 nm and fluorescence emissions were collected at 520 nm. Kalman filtering was applied during imaging with an acquisition time of 2.218 s/frame. Depending on the distribution of dye-loading and baseline cell signals, time-lapse images were recorded for n=5-8 tibiae/group/loading condition.

3.2.5 Whole-bone mechanical loading

Confocal time-lapse images were synchronized with a rest-inserted mechanical loading protocol to eliminate out-of-focus motion artifacts resulting from deformation of the bone

sample, with images being acquired every 5 seconds for 900 seconds total[19]. Five baseline images were acquired before mechanical loading was initiated via a trigger from the FluoView software to a 16-bit data acquisition (DAQ) card (NI USB-6210) and LabVIEW VI (National Instruments, Austin, TX, USA). Samples were maintained in supplemented cell culture media while cyclic mechanical loads were applied along the long axis of the whole bone using a custom-designed system[19]. A pre-load of 2 N was maintained, followed by cyclic axial loading of 1 Hz triangle waveforms with 4 s rest-insertion after each cycle to allow for confocal image acquisition. Two loading conditions were applied to samples from each treatment group: twenty-four tibiae (8 per treatment group) were mechanically stimulated at a load magnitude of 10 N, while another 24 were stimulated at load magnitudes to match an anteromedial cortical bone strain of 2000 με between treatment groups as determined by strain gauging experiments (3.2.7).

3.2.6 Osteocyte image analysis

Translation motion artifacts were removed using the StackReg image registration algorithm in ImageJ (U.S. National Institutes of Health; Bethesda, MD, USA). Cell bodies were manually traced using MetaMorph 7.0 (Molecular Devices, San Jose, CA, USA), and the average Fluo-8 AM intensity of the cell body was extracted for each cell as a function of time. Using MATLAB 2014b (The MathWorks, Natick, MA, USA), the average pixel intensity of each individual cell was normalized by the average of corresponding 5 baseline frames, and a Ca^{2+} peak was identified as a transient increase greater than 3 times the standard deviation of baseline intensity of each cell. The percentage of cells exhibiting ≥ 1 Ca^{2+} peak of all Fluo-8 dyed cells in the field of view, average number of Ca^{2+} peaks exhibited by responsive cells, average Ca^{2+} peak

magnitude relative to baseline intensity, and the average time to the first Ca^{2+} peak following initiation of mechanical loading were quantified for each tibia sample[19, 46, 47].

3.2.7 Local bone mineralization analysis

Two days prior to sacrifice, a subset of mice (n=8/group) were injected subcutaneously with the fluorochrome alizarin red (30 mg/kg in 2% $NaHCO_3$; Sigma-Aldrich, St. Louis, MO, USA) to capture bone mineralization at the Day 54 sacrifice time point. Following the Ca^{2+} imaging and loading period, alizarin red was imaged in the same field of view as the osteocyte network at 594 nm to create a 54 μm z-stack of images at a 0.25 μm resolution. Alizarin red intensity was summed over all images in the z-stack and the average intensity of bone tissue in the summed image stack was calculated for each sample using MATLAB 2014b.

3.2.8 Anteromedial cortical bone strain measurement

A subset of tibiae from Scl-Ab treated mice (n=4/treatment group) were frozen following Ca^{2+} imaging and used to experimentally quantify load-induced strain on the surface of the Ca^{2+} imaging region of interest. The tensile strain on the anteromedial cortical bone surface resulting from whole-bone compression was measured using commercial strain gauges (C2A-06-015LW-120; Micro-Measurements - Vishay Measurements Group, Raleigh, NC, USA). Strain gauges were secured to the tibia anteromedial surface using cyanoacrylate adhesive (M-Bond 200 Adhesive; Micro-Measurements - Vishay Measurements Group), consistent with the location of the typical osteocyte Ca^{2+} imaging region (Figure 3.2). Tibia samples were immersed in PBS while mechanical testing was performed using the custom *ex vivo* mechanical loading system. A 500 mN pre-load was applied to secure the sample, after which the linear actuator was extended to 350 μm at 10 μm/s to compress the sample. The strain gauge output was connected to a conditioner and amplifier system (2100 System; Vishay Measurements Group), and strain values

during the loading period were recorded by the National Instruments DAQ board. Linear regression was performed to determine the average force-strain relationship for each of the Scl-Ab treatment groups. Based on these relationships, corresponding load levels were calculated to match an anteromedial strain of 2000 με across groups for subsequent mechanical loading and Ca^{2+} imaging.

3.2.9 Statistics

One-way ANOVA with Tukey's HSD post hoc analysis was used to compare differences in means between treatment groups at each time point for cortical BMD, cortical thickness, and serum P1NP; differences between groups were similarly evaluated for endpoint measures of osteocyte Ca^{2+} signaling (responsive percentage, Ca^{2+} peak number, Ca^{2+} peak magnitude, time to 1st peak) as well as alizarin red mineralization. Differences in each Ca^{2+} signaling parameter between loading conditions (strain-matched vs. load-matched) were evaluated by Student's t-test for each treatment group. Statistical significance is observed at $p<0.05$.

3.3 Results

3.3.1 P1NP response to Scl-Ab dosing is dampened with long-term treatment

Serum levels of the bone formation marker P1NP were probed during Scl-Ab treatment in female BALB/cJ mice. The 58% decrease in mean P1NP levels in vehicle control mice over the course of the experiment likely reflects reduced bone formation as the mice approach skeletal maturity. Serum P1NP levels prior to the initiation of Scl-Ab treatment in all groups are comparable to those of vehicle control mice. Scl-Ab induced a peak in serum P1NP following the first Scl-Ab dose administered to the mice, evidenced by a 129% increase in P1NP at Day 4 relative to D0 baseline in the long-term treated group, and a nearly 200% increase in P1NP at

Day 46 relative to Day 42 in the short-term treated group (Figure 3.3), both of which are significantly greater than age-matched vehicle controls ($p<0.0001$). In the long-term treated group, this robust peak in serum P1NP is absent following the 7th and 8th doses of the drug; however, P1NP levels remain significantly elevated ($p<0.05$) compared to vehicle control throughout the eight-week dosing period, except for prior to Day 49 dosing. Probing P1NP levels over two doses of Scl-Ab in the short-term group demonstrates that the elevated P1NP response to the first dose of Scl-Ab persists, even through timepoints immediately before and 4 days prior to the second dose.

3.3.2 Cortical bone is enhanced with Scl-Ab treatment

Cortical bone in BALB/cJ mice was significantly enhanced as early as 14 days following the initiation of Scl-Ab treatment compared to vehicle control (Figure 3.4). At Day 14, following two doses of Scl-Ab, mice from the long-term treated group demonstrated an increase in cortical tibia BMD of 5.6% and increase in cortical thickness of 11%, both compared to vehicle control, with comparable increases exhibited by mice from the short-term treated group between Day 42 and Day 53. Cortical BMD remains significantly higher in long-term treated animals than vehicle control animals throughout the treatment period. However, the rate of change of percent increases over vehicle, while still demonstrating net increases in BMD, is attenuated after the initial two-week treatment (Table 3.1).

3.3.3 Bone formation with Scl-Ab treatment results in differences in tibial force-strain relationships

Using strain gauges affixed to the anteromedial cortical bone of Scl-Ab treated tibia, average force-strain relationships were determined for each of the three treatment groups (Figure 3.5). These linear relationships were highly correlated with the average anteromedial surface

strain from a given force applied to tibia for each treatment group (R^2>0.99). At the prescribed 10 N load magnitude, it was determined that tensile strains of 2045 με, 1843 με, and 1560 με were engendered on the anteromedial cortical bone of vehicle, short-term, and long-term treated samples during confocal imaging of osteocyte intracellular Ca^{2+}, respectively (Table 3.2). To match an anteromedial cortical surface strain of 2000 με across the treatment groups, load magnitudes of 9.8 N, 10.9 N, and 13.0 N were applied to samples from vehicle, short-term, and long-term treatment groups during osteocyte Ca^{2+} imaging, respectively.

3.3.4 Osteocyte Ca^{2+} signaling in response to mechanical loading is diminished following short-term Scl-Ab treatment, but persists after long-term treatment

At Day 54 sacrifice, time-lapse images of osteocyte intracellular Ca^{2+} in at least five of the eight Fluo-8 dyed tibia per treatment group per loading conditions were processed for analysis (Table 3.3). Temporal dynamics of Fluo-8 intensity were analyzed for Ca^{2+} responses to mechanical loading for an average of 103 osteocytes per tibia sample. Osteocytes networks from each treatment group exhibited robust intracellular Ca^{2+} oscillations in response to cyclic axial compression. In cells from samples matched to 10 N loading conditions, no significant differences were observed in percentage of responsive cells (Figure 3.6 A) nor the characteristics of the responsive osteocyte Ca^{2+} peaks (Figure 3.6 B-D) between either Scl-Ab treatment group and vehicle control. Under strain-matched loading conditions of 2000 με, there was no difference in osteocyte Ca^{2+} signaling parameters between vehicle and long-term Scl-Ab treated groups. However, in the short-term treated group, the percentage of responsive cells was significantly reduced by about 16% compared to osteocytes in the strain-matched vehicle group ($p<0.05$, Figure 3.6 A). Initiation of Ca^{2+} signaling was also delayed as indicated by an increased time to the first Ca^{2+} peak observed during the imaging period (218.7 ± 36.4 s) compared to

vehicle control (149.1 ± 39.8 s) (Figure 3.6 D). Ca^{2+} peak magnitude and average number of Ca^{2+} peaks exhibited by the osteocytes did not differ between groups under strain-matched conditions. Overall, Ca^{2+} signaling measures did not differ between strain-matched and load-matched conditions for each treatment group.

3.3.5 Local bone mineralization is enhanced following short-term treatment of Scl-Ab

By averaging the intensity of summed z-stack images of alizarin red in the region of osteocyte imaging, mineralization in response to short-term and long-term Scl-Ab treatment prior to animal sacrifice was estimated. Newly calcified bone was more evident in short-term treated tibia, with an alizarin red intensity that was 52% higher than vehicle and 19% higher than long-term treated tibia in the region of interest (Figure 3.8). This increased intensity was only significant between vehicle and short-term tibia ($p<0.01$); alizarin red intensity of long-term treated tibia did not differ from short-term treated samples nor vehicle control.

3.4 Discussion

In both pre-clinical and clinical studies, Scl-Ab treatment has been shown to induce a robust initial phase of bone formation, evidenced by a rapid increase in BMD accompanied by a peak in circulating levels of P1NP. However, with continued long-term treatment with Scl-Ab, increases in BMD are slowed, driven by the reduction in bone resorption rather than increases in bone formation. Transient peaks in serum P1NP are also dampened in response to repeated doses. Thus, in their recent review of novel actions of sclerostin in bone, Holdsworth et al. posit that the bone formation response to Scl-Ab can be separated into two phases: an initial transient phase where Scl-Ab significantly and rapidly increases modeling-based bone formation; and a steady phase where BMD continues to increase due to long-term decreases in bone resorption,

but bone formation rates decline towards baseline levels with continuous treatment with Scl-Ab[94]. Based on these observations, we hypothesized that rapidly enhanced bone mass with initial Scl-Ab treatment changes the mechanical environment that osteocyte networks experience under physiological loading conditions, therefore influencing their mechanosensing as measured by Ca^{2+} signaling responses (Figure 3.8 A). Given their role in mechanotransduction, this altered mechanosensing in osteocytes could possibly have downstream consequences affecting osteoblast bone formation processes, resulting in the dampened bone formation response to long-term Scl-Ab treatment.

Serum levels of the bone formation marker P1NP were probed at different dosage points throughout the eight-week treatment period to investigate the bone formation response to Scl-Ab with short-term and long-term treatment. In agreement with a previous study of Scl-Ab treatment and P1NP dynamics in BALB/c mice[35], the P1NP response after an initial dose of Scl-Ab was significantly larger than responses in both age-matched animals that had received multiple doses of the antibody as well as age-matched vehicle control animals. Our findings are also consistent with the pulsatile profile of serum P1NP levels following initiation of treatment with romosozumab in clinical trials[33, 34]. However, while we have confirmed the dampening of the pulsatile P1NP response following repeat dosing of Scl-Ab, serum P1NP levels in the long-term treated group remain significantly elevated compared to vehicle control throughout the treatment period. We attribute this to our use of an increased dosage of 25 mg/kg/week compared to the previous study in 8-10-week-old BALB/c mice, which used 10 mg/kg/week. Our study is the first to probe naïve serum P1NP responses immediately prior to and four days following consecutive treatment doses, and our use of a higher dosage of Scl-Ab may also explain the sustained peak of P1NP over two consecutive doses of the drug in the short-term treated animals.

Consistent with previous reports, our temporal *in vivo* micro-CT measures of murine tibia cortical bone show that Scl-Ab rapidly increased both cortical BMD and cortical thickness within the first two weeks of treatment. These increases are maintained in long-term treated tibia cortical bone throughout the eight-week period, although rates of increase slow with repeated dosing. Percent changes in cortical BMD and cortical thickness relative to vehicle control in long-term treated mice differ slightly from the previous study of a similar treatment timeline in BALB/c mice[35], but may be explained by our local analysis of tibia cortical bone rather than whole body BMD. Our analysis of bone mineralization in the region of osteocyte Ca^{2+} signaling also confirms that bone formation is still be occurring with long-term treatment, albeit not at the initial rapid rate as in mice that have been treated with short-term Scl-Ab dosing, confirming the effects of the steady phase where net positive bone balance is reflected by decreased resorption concurrent to extended bone formation. Taken together, our *in vivo* cortical bone formation data as well as our findings using alizarin red intensity as an *ex vivo* measure of mineralization support the two phases of response to Scl-Ab proposed by Holdsworth et al.

It has been hypothesized that a rapid increase in bone mass during the initial, transient phase of response to Scl-Ab may lead to a reduction in local micro-strain on bone surface, thus activating negative feedback mechanisms to control bone formation[94]. Our strain-gauging data of Scl-Ab treated tibia confirms that increased cortical bone mass following long-term Scl-Ab treatment results in a decreased level of mechanical strain on the anteromedial cortical bone surface strain for a given mechanical load. For example, long-term Scl-Ab treatment contributes to a 23.7% decrease in anteromedial strain compared to age-matched vehicle controls (2045 με to 1560 με) when both are loaded at 10 N. However, as we see with our Ca^{2+} signaling results in osteocytes of samples matched to a 10 N load between treatment groups, osteocyte

mechanosensing is maintained despite the differential strain engendered due to Scl-Ab treatment. Prior studies on bone formation with varying load/strain applications *in vivo* suggest that differential strain increments from 350-500 με are sufficient to induce significant differences in cortical bone formation responses[101, 102]. However, the BALB/c mice used in the current study may exhibit different responses to given strain increments than the low bone mass C57BL/6 in which these *in vivo* studies were conducted[103]. Nonetheless, we show that the altered whole-bone mechanics due to Scl-Ab treatment does not induce changes in osteocyte Ca^{2+} signaling.

While the strain-matched osteocyte Ca^{2+} imaging experiments were expected to yield consistent mechanosensitive signaling characteristics between treatment groups due to the matched anteromedial cortical bone strain at our imaging region of interest, our analysis showed unexpected results. Fewer osteocytes responded with delayed Ca^{2+} peaks in short-term treated mice under strain-matched loading conditions. This reduced local responsiveness may reflect the behavior of "immature" osteocytes embedded in newly-formed cortical bone. Indeed, based on our alizarin red intensity data co-localized to regions of osteocyte Ca^{2+} signaling, we find that the osteocytes analyzed from the short-term group are located in bone that has been newly mineralized in response to initial Scl-Ab treatment. In mice, the bone formation rate has been shown to increase from about 1.5 to 2 $\mu m^3/\mu m^2$/day with 3 weekly doses of anti-sclerostin antibody[104]. Given our osteocyte Ca^{2+} imaging depth of ~20-30 μm below the bone surface, it is likely that we are capturing osteocytes in newly-formed bone under short-term (2 weekly doses) of Scl-Ab. Previous studies have shown that osteocyte networks are much more sensitive than osteoblasts to fluid flow stimulation *in vitro*[46] and whole-bone compression *ex vivo*[19] in terms of Ca^{2+} oscillations. Considering that an osteocyte is formed from an osteoblast that has been embedded in the matrix it has secreted, it is possible that newly mineralized osteocytes may not

yet exhibit the robust Ca^{2+} signaling capabilities seen in mature osteocyte networks. Additionally, while anteromedial cortical strains have been matched between treatment groups based on experimental strain gauge studies, the matrix-level material properties of the newly mineralized bone may influence the mechanosensing of newly-embedded osteocytes with short-term Scl-Ab treatment. Ca^{2+} responses in the long-term treated group were consistent with osteocytes formed during normal bone homeostasis (vehicle), suggesting that cells embedded as a consequence of bone formation response to long-term Scl-Ab treatment eventually demonstrate a "mature" mechanosensing phenotype. Future studies focusing on osteocyte maturation under Scl-Ab treatment, such as morphological characteristics of *in situ* osteocytes between treatment groups, may support this theory. We do not observe differences in osteocyte Ca^{2+} signaling in load-matched tibia samples where different strains are engendered between treatment groups, which may be masking the localized effects of new bone formation on short-term treated osteocyte mechanosignaling.

Taken together, we conclude that rapid increases in bone mass in the initial bone formation response to Scl-Ab treatment result in reduced Ca^{2+} signaling of newly-embedded osteocytes on the periosteal surface. (Figure 3.8 B). Future work will utilize *in vivo* micro-CT data to investigate periosteal bone modeling and remodeling dynamics in an effort to further attribute rapid mineralization of osteocytes under short-term treatment to the diminished mechanosensitivity of osteocyte Ca^{2+} signaling and identify the mechanisms responsible for the two phases of Scl-Ab bone formation response. This periosteal data will also more closely localize bone formation analysis to the osteocytes in the anteromedial cortical bone surface that we study in our *ex vivo* murine model of Ca^{2+} signaling. We also conclude that osteocyte mechanosensing is maintained with long-term Scl-Ab treatment. Mechanically induced Ca^{2+}

signaling in osteocytes has been shown to influence load-induced bone formation responses[100], but there may be other factors downstream of Ca^{2+} signaling which contribute to the steady phase response to continuous Scl-Ab treatment. For instance, upregulation of various Wnt targets accompanies long-term treatment with Scl-Ab, which may exert a negative feedback to increased Wnt signaling and contribute to self-regulation of bone formation with long-term Scl-Ab treatment[35, 105].

3.5 Conclusions

This study is the first to capture real-time, immediate, mechanosensitive Ca^{2+} responses to load in osteocytes from mice treated with Scl-Ab. By comparing the peak characteristics of Ca^{2+} oscillations in osteocyte networks under load-matched tibial compression, we found that osteocyte mechanosensing is maintained and that the steady bone formation response to long-term treatment may be attributed to self-regulation downstream of Ca^{2+} signaling. However, when mechanical strain is matched between treatment groups, osteocytes embedded during the initial transient bone formation response to Scl-Ab exhibit diminished Ca^{2+} signaling characteristics compared to mature osteocyte networks. These observations further our understanding of the mechanisms of different phases of bone formation responses to Scl-Ab treatment.

3.6 Tables

	% increase, Cortical BMD		% increase, Cortical thickness	
	Short-Term	Long-Term	Short-Term	Long-Term
Day 14	0.3 ± 0.1	5.6 ± 0.3	-0.1 ± -0.01	11 ± 0.6
Day 28	0.7 ± 0.03	8.9 ± 0.5	-3.0 ± -0.3	19 ± 1.3
Day 42	0.7 ± 0.04	10 ± 0.5	-2.5 ± 0.5	19 ± 3.3
Day 53	5.8 ± 0.3	12 ± 0.6	11 ± 0.8	25 ± 1.6

Table 3.1 Percent changes in cortical bone formation in response to short-term and long-term Scl-Ab treatment. Biweekly *in vivo* micro-CT scans reveal increases in cortical BMD (mg HA/ccm) and cortical thickness (mm) within two weeks of initiation of Scl-Ab treatment for long-term (Day 14) and short-term (Day 53) treated animals. Percent changes (mean ± SD) are calculated relative to age-matched vehicle controls. Greyed values represent time points before effects of Scl-Ab administration.

		Vehicle	Short-Term	Long-Term
Load-matched	Load magnitude	10 N		
	Strain magnitude	2045 με	1843 με	1560 με
Strain-matched	Load magnitude	9.8 N	10.9 N	13.0 N
	Strain magnitude	2000 με		

Table 3.2 Loading parameters for tibia samples used for osteocyte Ca^{2+} imaging. Load-matched samples in each treatment group were subjected to a 10 N load magnitude and resulting anteromedial cortical bone surface strains were calculated from force-strain relationships as determined by strain gauge experiments. To achieve a strain magnitude of 2000 με, samples from each treatment group were subjected to mechanical load magnitudes calculated from treatment-specific force-strain relationships.

		Vehicle	Short-Term	Long-Term
Load-matched	Tibia Samples	6	5	8
	Osteocytes	716	395	1039
Strain-matched	Tibia Samples	8	6	6
	Osteocytes	996	415	594

Table 3.3 Experimental tibia samples and osteocytes for analysis. Ca^{2+} signaling in osteocytes from treated tibia samples were analyzed for both the load-matched and strain-matched loading conditions, depending on the success of Fluo-8 intracellular Ca^{2+} dye-loading and baseline cell signals.

3.7 Figures

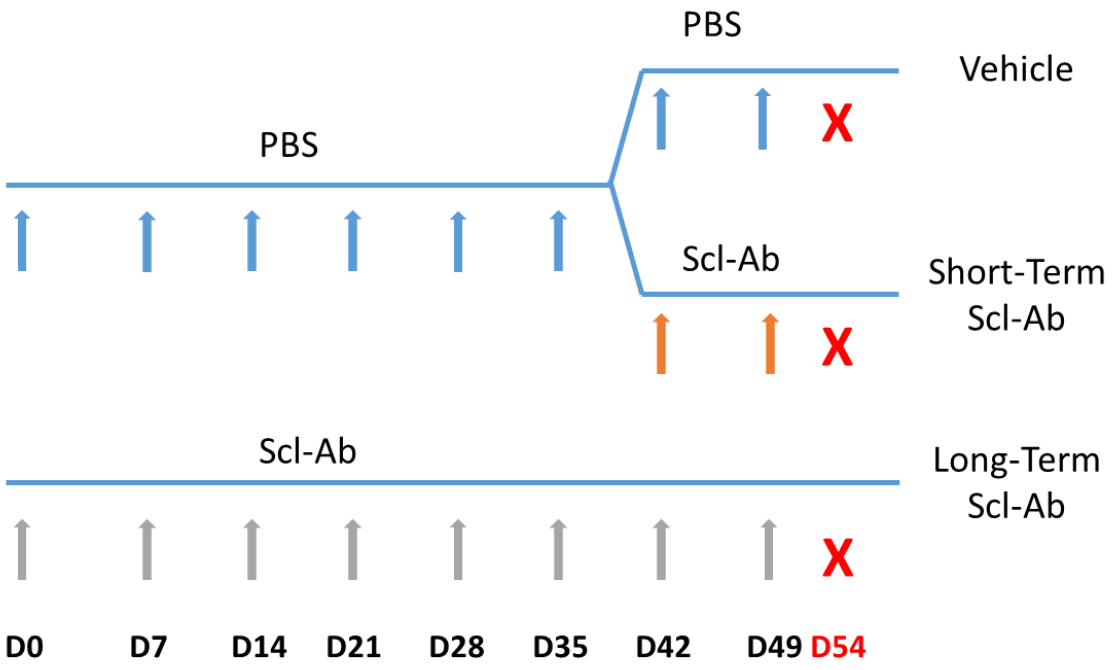

Figure 3.1 Timeline for Scl-Ab treatment. Female BALB/cJ mice were given weekly subcutaneous injections of 25 mg/kg Scl-Ab or PBS vehicle. Vehicle control mice were given eight doses of PBS. Short-term Scl-Ab treated mice received six doses of PBS before beginning Scl-Ab treatment at Day 42. Long-term Scl-Ab treated mice received eight doses of Scl-Ab. All mice were sacrificed at Day 54 for osteocyte Ca^{2+} imaging experiments. n=16 mice/treatment group.

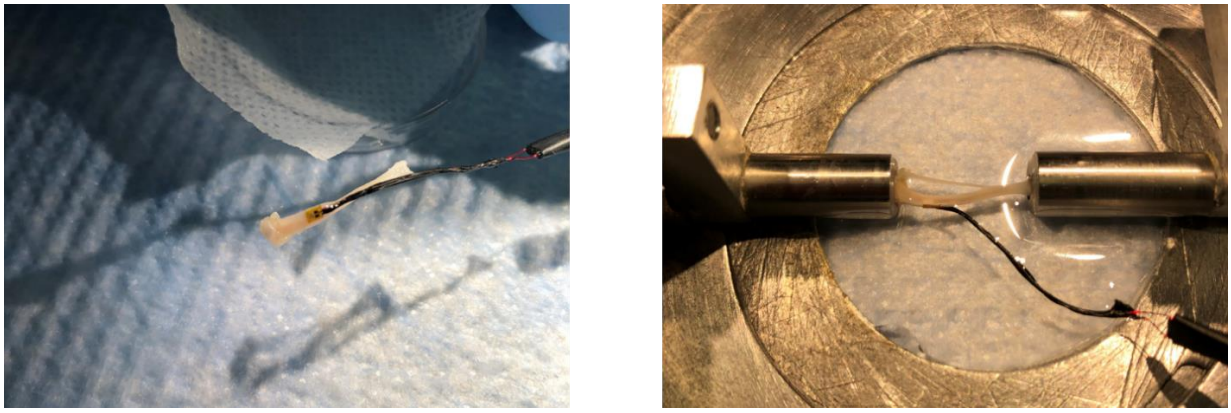

Figure 3.2 Strain gauge experimental set-up. Strain gauges are affixed to the anteromedial cortical bone surface of frozen tibiae (left) and tested in the custom *ex vivo* axial mechanical loading system (right) while submerged in phosphate buffered saline. Cortical bone surface strains were recorded as the tibia samples were axially compressed.

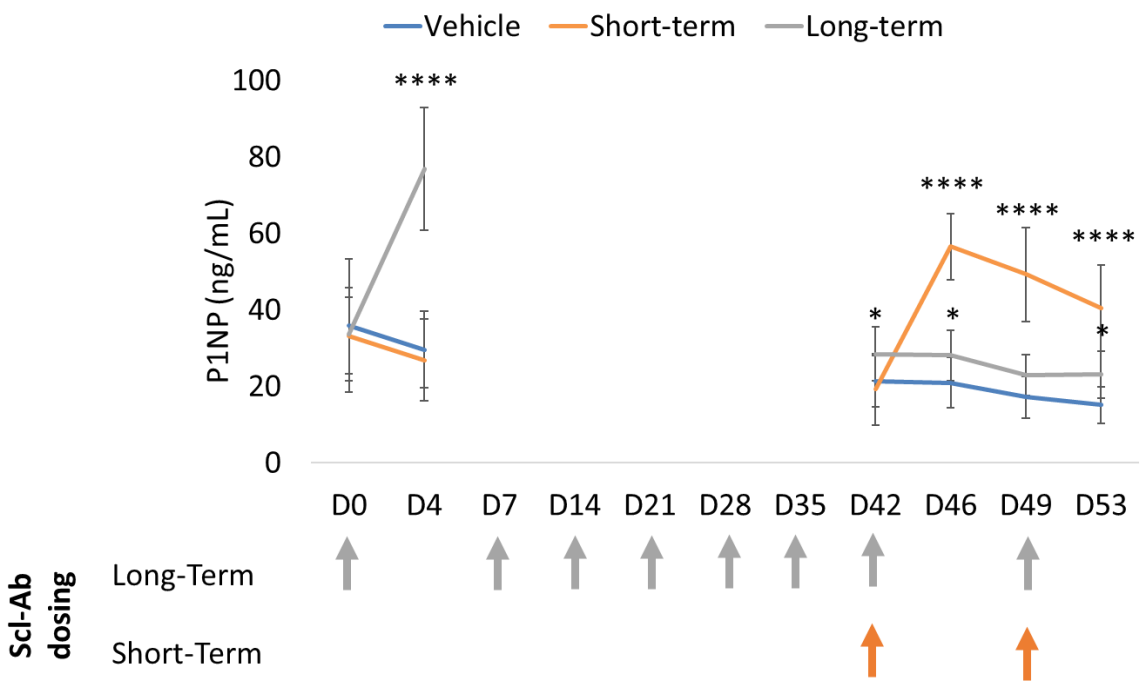

Figure 3.3 Serum P1NP levels during Scl-Ab treatment. P1NP was detected by enzyme immunoassay from serum samples taken immediately prior to and 4 days following treatment doses (Scl-Ab doses indicated by arrows; n=14-16 mice/group). Data are mean ± SD. *p<0.05, ****p<0.0001 compared with vehicle control (one-way ANOVA, Tukey's HSD).

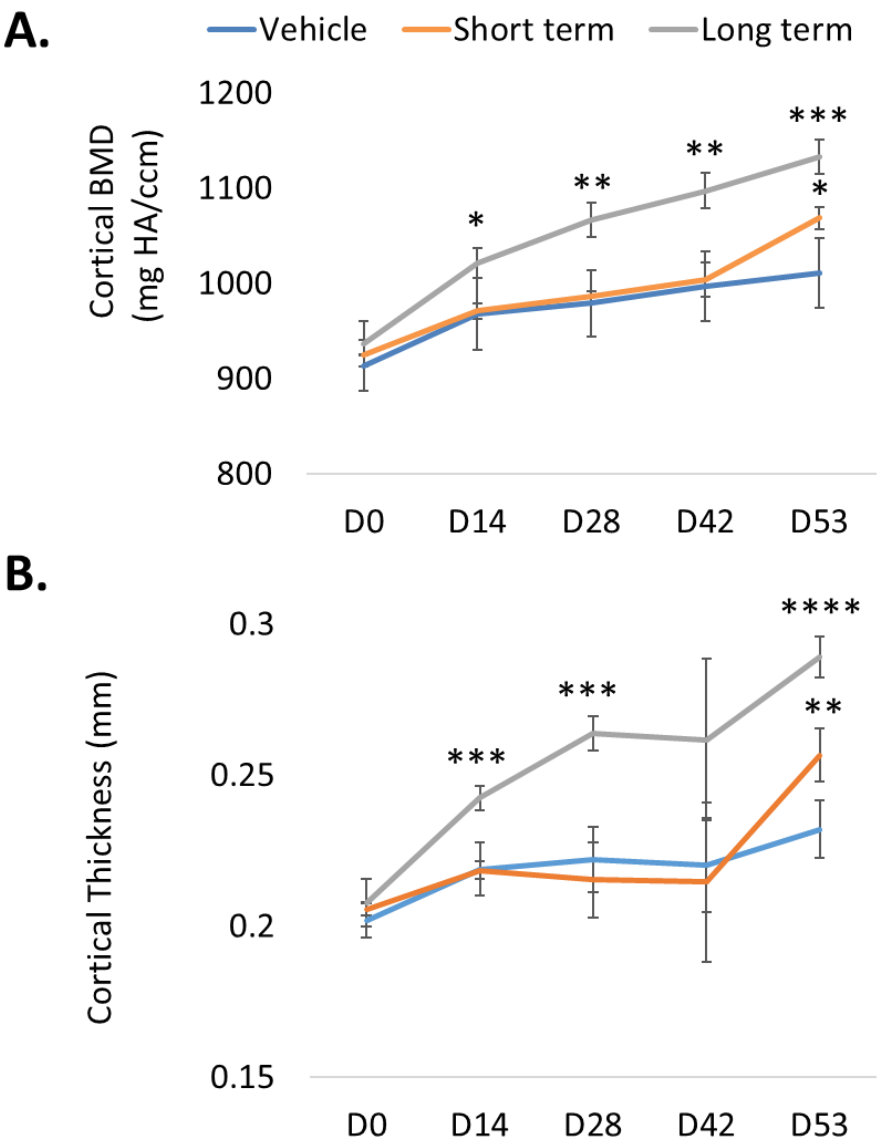

Figure 3.4 *In vivo* cortical bone responses to treatment with Scl-Ab. A. Cortical bone mineral density (BMD) and **B.** cortical thickness in a sub-set of Scl-Ab treated mice (n=4/group) as measured by biweekly *in vivo* micro-CT scans of the left tibia. Data are mean ± SD. *p<0.05, **p<0.01, ***p<0.001, ****p<0.0001 compared with vehicle control (one-way ANOVA, Tukey's HSD).

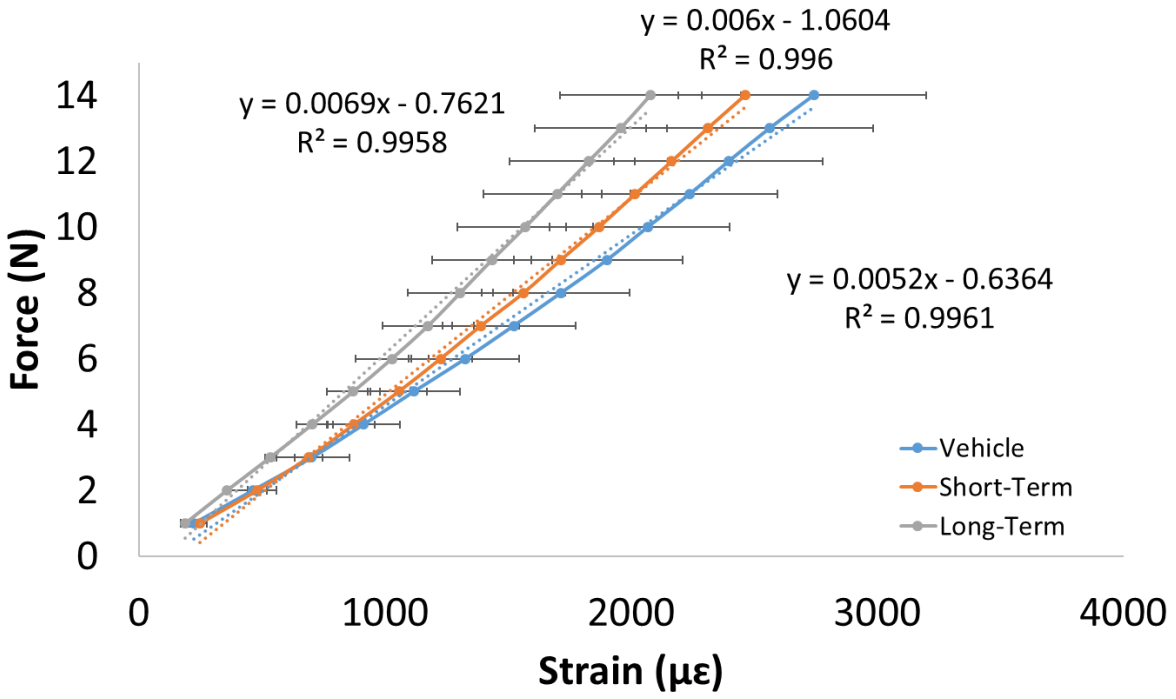

Figure 3.5 Experimentally-determined force-strain relationships in tibia from Scl-Ab treated mice. Linear regression determines linear relationships (dotted lines) between force applied and anteromedial cortical bone surface strain for vehicle, short-term, and long-term Scl-Ab treatment groups (n=4 tibia/group). Data are mean ± SD.

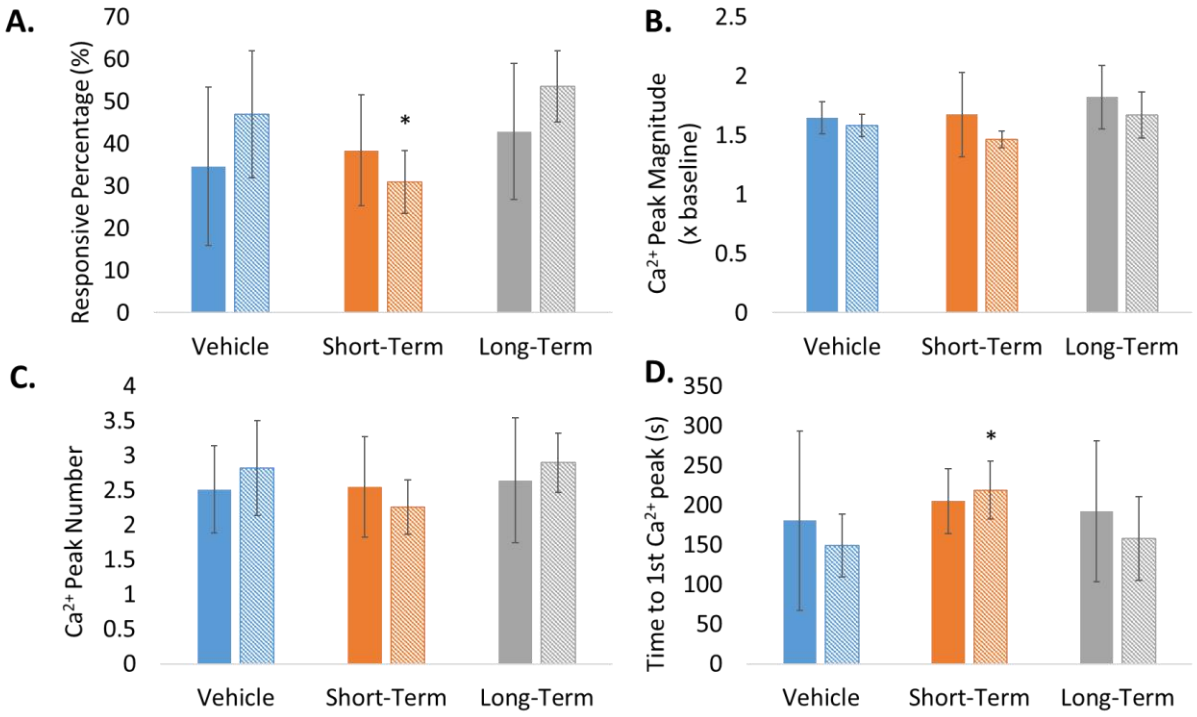

Figure 3.6 Ca^{2+} signaling parameters of osteocytes from Scl-Ab treated mice. Ca^{2+} peak characteristics were determined for cells under load-matched (solid) and strain-matched (hatched) mechanical loading for each treatment group. **A.** Percentage of responsive cells ($\geq$1 Ca^{2+} peak) was determined from of all cells in the field of view of each treated tibia sample. **B.** The average magnitude Ca^{2+} peaks relative to baseline intensities, **C.** the average number of Ca^{2+} peaks, and **D.** the time at which the first Ca^{2+} peak was observed were quantified based on individual osteocyte Fluo-8 intensities over the 900s loading period. n=5-8 tibia/group/loading condition. Data are mean ± SD. *$p<0.05$ compared with strain-matched vehicle control (one-way ANOVA, Tukey's HSD).

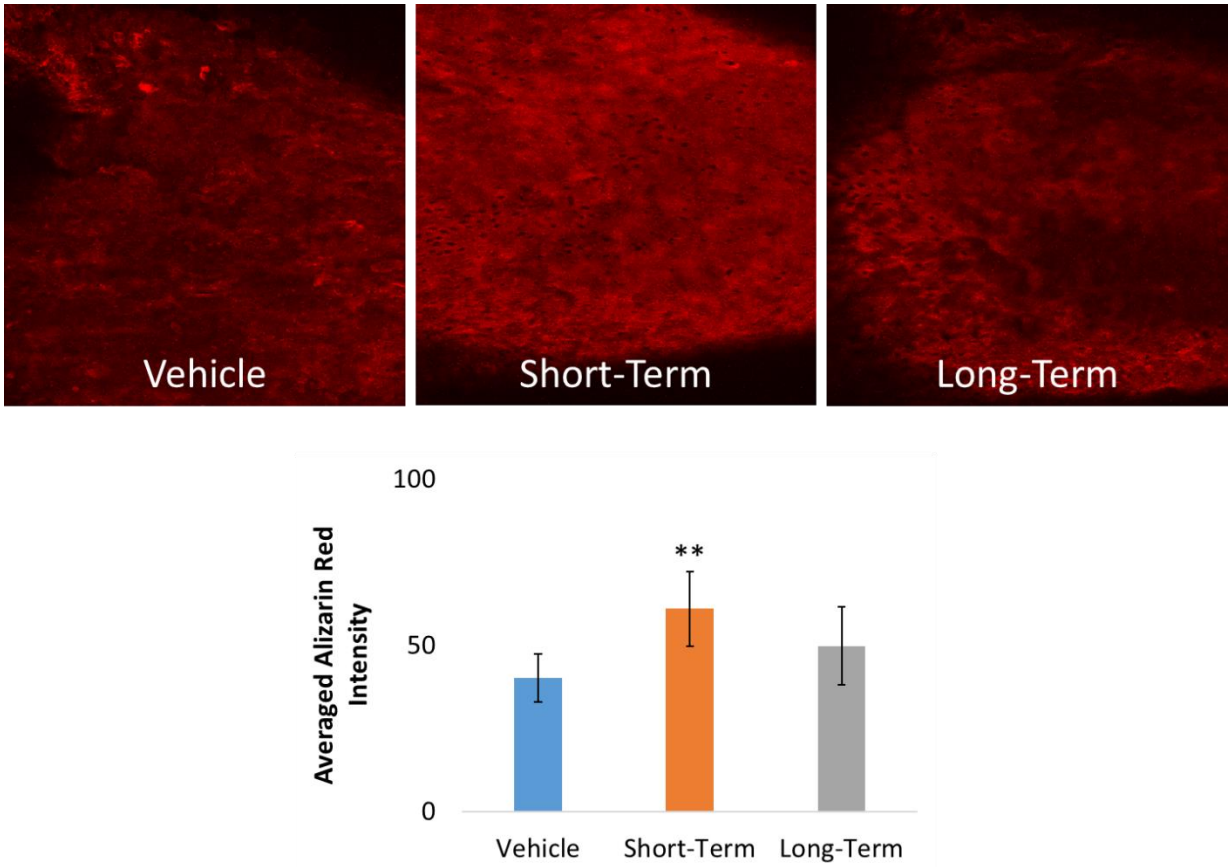

Figure 3.7 Local bone mineralization in Scl-Ab treated mice. Alizarin red intensity was averaged to estimate mineralization in the field of view of Ca^{2+} signaling in response to vehicle, short-term, and long-term Scl-Ab treatment (n=6-7 tibia/group). Data are mean ± SD. **p<0.01 compared with vehicle control (one-way ANOVA, Tukey's HSD).

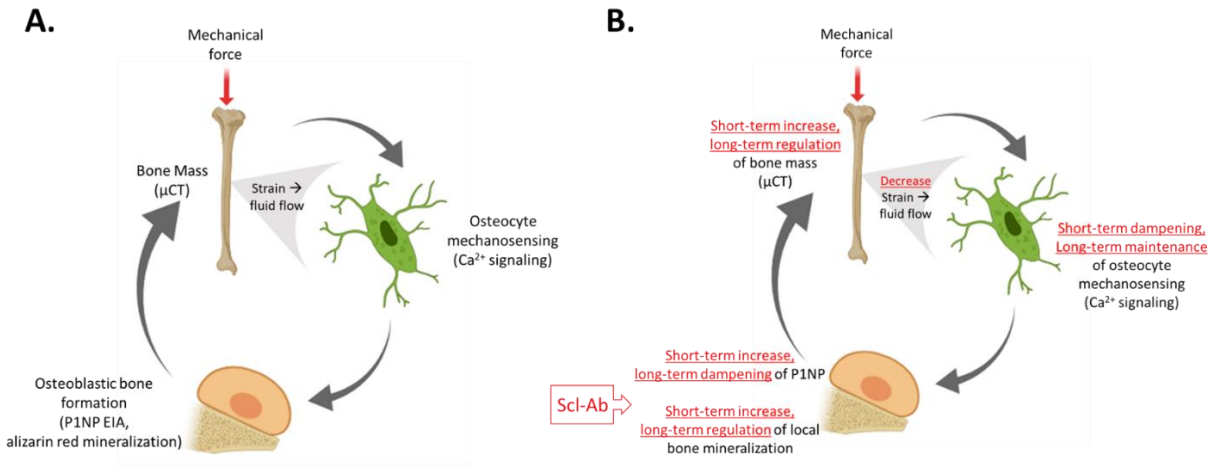

Figure 3.8 Bone formation processes in response to Scl-Ab treatment. A. In homeostasis, mechanical forces applied to whole bones result in tissue-level mechanical strain and subsequent fluid flow in the lacunar-canalicular system that is sensed by osteocytes. Osteocyte mechanosensing regulates bone formation processes, which in turn modify bone mass and whole bone mechanics. **B.** Under Scl-Ab treatment, osteoblastic bone formation is initially enhanced, resulting in a rapid, transient increase in bone mass. Local rapid bone mineralization diminishes Ca^{2+} signaling in newly-embedded osteocytes, either due to their immature phenotype or the mechanical properties of newly-mineralized bone. However, with long-term treatment, the P1NP response to Scl-Ab dosing indicative of osteoblast bone formation is dampened and increases in bone mass reach a steady phase. Osteocyte mechanosensing is maintained despite altered whole-bone mechanical properties seen with long-term Scl-Ab treatment, suggesting that other downstream factors are contributing to the self-regulation of the bone formation response to Scl-Ab.

Chapter 4: Real-Time Observation of Mechanosensitive Intracellular Calcium and Actin Network Dynamics in *Ex Vivo* Osteocytes

This thesis chapter has been previously published, in part, in the manuscript:

Andrea E. Morrell, Genevieve N. Brown, Samuel T. Robinson, Rachel L. Sattler, Andrew D. Baik, Gehua Zhen, Xu Cao, Lynda F. Bonewald, Weiyang Jin, Lance C. Kam, X. Edward Guo. "Mechanically induced Ca^{2+} oscillations in osteocytes release extracellular vesicles and enhance bone formation". *Bone Research* 2018 **6**(1):72-82.

4.1 Introduction

From a morphological standpoint, osteocytes lend their ability to sense whole-bone mechanical forces to their unique stellate features, longevity, and intercellular connectivity throughout a vast network embedded in the bone tissue[106]. Biochemical evidence of osteocyte mechanosensing is supported by studies investigating intracellular calcium (Ca^{2+}) signaling in osteocytes in response to various mechanical stimuli[50, 51, 77, 107]. For example, when exposed to fluid shear *in vitro* and dynamic deformational loading of whole bones *ex vivo*, osteocytes exhibit robust, unattenuated oscillations in intracellular Ca^{2+}, dependent on extracellular Ca^{2+} and the second messenger ATP[19, 47]. Furthermore, it has been shown that release of Ca^{2+} from intracellular stores temporally corresponds with and contributes to these robust oscillations in cytosolic Ca^{2+} oscillations[48]. Ca^{2+} oscillations in osteocytes are distinct from those of osteoblasts, more abundant than autonomous signals, and become more pronounced under increasing mechanical loading magnitudes[19, 46], suggesting that osteocyte mechanosensitivity can be encoded through unique intracellular Ca^{2+} dynamics.

As osteoblasts embed in the bone matrix to differentiate into osteocytes, changes in cytoskeleton arrangement and distribution of structural elements occur, including formation of a dense cortical actin shell as well as actin-enriched structures that extend the entire length of the dendrites[108-110]. This uniquely-organized actin cytoskeleton of osteocytes can respond and restructure in response to mechanical loading[70, 108]. Previous work investigating dynamics of single osteocyte cytoskeletal components under flow showed that fluid shear introduces strains in the cortical actin network, demonstrating sensitivity of the actin cytoskeleton to mechanical stimuli[111, 112]. The influence of this early deformation of the osteocyte actin network on Ca^{2+} signaling was investigated in subsequent unpublished work from our group which utilized cytochalasin D to disrupt osteocyte actin polymerization prior to fluid flow, significantly reducing both the number and magnitude of flow-induced Ca^{2+} peaks[113]. While this suggests the importance of the actin cytoskeleton in initiating Ca^{2+} responses to fluid flow, there is little evidence of actin cytoskeleton dynamics occurring downstream, or dependent upon, Ca^{2+} signaling in osteocytes.

Since Ca^{2+} signaling can regulate diverse cellular functions in multiple cell types, continued study of this mechanosensitive phenomenon in osteocytes begs the question of functionality. One consequence of Ca^{2+} signaling that is well-characterized in other cell types is Ca^{2+}-dependent contractility. While classically attributed to muscle cells[114], other cell types utilize this mechanism for specific functions, such as release of extracellular vesicles[115] or wound healing[116-118]. Interestingly, the expression of muscle contraction-related proteins is upregulated as bone cells mature into osteocytes[119]. Regarding actin network responses downstream of Ca^{2+}-signaling, we have observed Ca^{2+}-dependent, smooth muscle-mediated contractility in osteocytes *in vitro* with implications for cell-cell communication via extracellular vesicles[100]. However, the

relationship between Ca^{2+} signals and downstream cytoskeletal dynamics in native osteocytes, as well as their mechanosensitive potential under physiological load, has yet to be explored.

Our laboratory has developed a synchronized mechanical loading and imaging approach for investigating *in situ* osteocyte Ca^{2+} mechanotransduction[19]. This model maintains a viable osteocyte network in tibiae *ex vivo*, allowing for simultaneous application of physiological mechanical loads to the whole bone and imaging of osteocytes *in situ*. Intracellular dyes are utilized to access osteocytes in the bone tissue and fluorescently image real-time Ca^{2+} dynamics in response to load. The flexibility of this system permits the study of osteocyte mechanosensitivity in tibia samples from a variety of contexts, as we have seen in this body of work studying aged mice and mice receiving therapies promoting anabolic bone formation. Additionally, transgenic mice expressing fluorescent tags to various intracellular structures and molecules would permit visualization of a variety of real-time responses of *in situ* osteocytes to whole bone mechanical loading.

In this study, our goal was to enhance our established model of *ex vivo* osteocyte mechanotransduction to include real-time, simultaneous, high-magnification visualization of Ca^{2+} signaling and actin network dynamics in response to mechanical loading to identify potential Ca^{2+}-dependent contractile behavior as we have observed *in vitro*[100]. Based on our knowledge of mechanosensitive Ca^{2+} signaling in *ex vivo* osteocytes, we hypothesize that these load-induced Ca^{2+} oscillations will yield similarly mechanosensitive actin contractions in osteocytes residing in their native 3D network.

4.2 Materials and Methods

4.2.1 Mice

Lifeact mRFPruby mice, a gift from Michael Sixt and Roland Wedlich-Söldner at the Max Planck Institute of Biochemistry, were bred with C57BL/6 J mice (The Jackson Laboratory, Bar Harbor, ME, USA) to produce offspring with the filamentous actin (F-actin) network tagged with mRFP in all cell types, including osteocytes[120, 121]. These mice were genotyped for Lifeact by screening tail-snipped tissue samples for RFP. Ai38 mice were purchased from The Jackson Laboratory (B6;129S-*Gt(ROSA)26Sor*$^{tm38(CAG-GCaMP3)Hze}$/J mice) and bred to Dmp1-Cre mice (a gift from Dr. Lynda Bonewald). Dmp1-Cre;Ai38$^{flx/flx}$ mice expressing the Ca^{2+} indicator GCaMP3 targeted to osteocytes[71-73] were then bred to Lifeact mRFP$^{+/-}$ mice to produce triple transgenic Dmp1-Cre;Ai38$^{flx/flx}$;Lifeact mRFP$^{+/-}$ mice (Figure 1). Mice were genotyped for Cre and Ai38 using qPCR on tissue lysates with previously noted primer sequences[71, 72]. All animals were housed 2-5 per cage and given access to food and water *ad libitum* (PicoLab 5053 and 5058, LabDiet, St. Louis, MO, USA). All animal procedures were approved by the Institutional Animal Care and Use Committee at Columbia University in accordance with Institute for Comparative Medicine and national guidelines.

4.2.2 Osteocyte intracellular Ca^{2+} and actin imaging

Three-month-old Lifeact mRFP$^{+/-}$ mice were sacrificed by CO_2 inhalation and bilateral tibiae were immediately dissected under sterile conditions. Tibiae were maintained in supplemented cell culture media (αMEM + 5% calf serum, 5% defined fetal bovine serum) and incubated at 37°C, 5% CO_2 for 2 hours. Tibia samples were then incubated with Ca^{2+} indicator Fluo-8 AM (AAT Bioquest, Sunnyvale, CA, USA) dissolved in 20% Pluronic F-127 in DMSO (Invitrogen, Carlsbad, CA, USA) for 45 minutes, washed, and post-incubated for 10 minutes

before being transferred to a custom mechanical loading device for simultaneous loading and imaging. Tibiae from three-month-old Dmp1-Cre;Ai38$^{flx/flx}$;Lifeact$^{+/-}$ mice were similarly dissected and maintained in supplemented media before being immediately placed in the custom mechanical loading device.

Using an Olympus FluoView FV1000 laser scanning confocal microscope with a 60x long working distance objective, Fluo-8 AM dyed osteocytes expressing Lifeact mRFP (Fluo-8 + Lifeact) or osteocytes expressing both GCaMP3 and Lifeact mRFP (GCaMP3 + Lifeact) were visualized 20-30 µm below the anteromedial cortical bone surface of either the right or left tibiae, depending on Fluo-8 AM dye baseline signals. Fluo-8 AM and GCaMP3 Ca^{2+} indicators were excited at 473 nm and fluorescence emissions were collected at 520 nm, while Lifeact mRFP was sequentially excited at 559 nm and collected at 618 nm. Kalman filtering was applied during sequential imaging with an acquisition time of 2.218 s/frame acquired every 6 seconds.

4.2.3 Biochemical stimuli of intracellular Ca^{2+}

For Fluo-8 + Lifeact osteocytes, either 20 mM ATP (20 mM, n=15 cells) or ionomycin (20 µM n=33 cells) (both Sigma-Aldrich, St. Louis, MO, USA) was added via micro-pipette to tibia samples secured in the custom loading device while Ca^{2+} and actin network dynamics were imaged simultaneously. For GCAMP3 + Lifeact osteocytes, either ATP (10 mM, n= 6 cells) or ionomycin (10 µM, n= 6 cells) was added to the media well of the loading system via syringe. Identical volumes of culture media were similarly introduced to the media well before each biochemical stimulus as a negative control.

4.2.4 Whole-bone mechanical loading

For mechanical loading experiments, confocal time-lapse images were synchronized with a rest-inserted mechanical loading protocol to eliminate out-of-focus motion artifacts resulting from deformation of the bone sample. Five baseline images were acquired before mechanical loading was initiated via a trigger from the FluoView software to a 16-bit data acquisition (DAQ) card (NI USB-6210) and LabView VI (National Instruments, Austin, TX, USA). Samples were maintained in supplemented cell culture media while cyclic mechanical loads were applied along the long axis of the tibia using a custom-designed system[19]. A pre-load of 2 N was applied, followed by cyclic axial loading of 1 Hz triangle waveforms with 5 s rest-insertion after each cycle to allow for confocal image acquisition. A load magnitude of 8 N was applied to Fluo-8 + Lifeact tibia samples (n=19 cells). For GCAMP3 + Lifeact samples, loading bouts with magnitudes of 4 N and 8 N applied to each tibia in random order with 15 minutes of rest between bouts. These samples were categorized as undergoing either an increasing load sequence (4 N → rest → 8 N; n=6 cells) or decreasing load sequence (8 N → rest → 4 N; n=6 cells).

4.2.5 Osteocyte image analysis

Analysis of Fluo-8, Lifeact mRFP, and GCaMP3 images was performed in MATLAB 2014b (The MathWorks, Natick, MA, USA). Strain fields in individual cells were directly estimated from time-lapse Lifeact mRFP images without the need to first estimate displacements, resulting in a very simple method and low computational cost[122]. From these strain fields, average strains of the intracellular cytoskeletal network relative to the long and short axes of the osteocyte cell body were calculated over time. Average pixel intensity of the Ca^{2+} indicator in each individual cell was normalized by the average intensity of

corresponding baseline frames. A Ca^{2+} peak was defined as a transient increase greater than three times the standard deviation of the baseline intensity noise in each cell. A contraction in either the long or short axis of the cell was defined by a decrease and recovery of normal strain with a minimum prominence of 1.5% strain. For Fluo-8 + Lifeact cells, the frequency of Ca^{2+} peaks and contractions in both the long and short axes of the cells were calculated for cells with >2 Ca^{2+} peaks (n=9 cells). A measure of percent synchrony between the contractions in each of the cell axes and Ca^{2+} peaks was calculated as described previously[48]. For GCaMP3 + Lifeact cells, the number of Ca^{2+} peaks and total contractile events, contractile events along the short axis of the cell, and contractile events along the long axis of the cell were quantified.

4.2.6 Statistics

All data are presented as mean ± standard deviation. Paired Student's t-test was used to determine significant differences in frequency between Ca^{2+} peaks and contractile events in Fluo-8 + Lifeact cells. For GCaMP3 + Lifeact cells, the number of Ca^{2+} peaks, total contractile events, contractile events along the short axis of the cell, and contractile events along the long axis of the cell were compared between load levels using paired Student's t-test; comparisons were made between the first loads of different loading sequences (increasing vs. decreasing) using Student's t-test. Statistical significance is observed when $p<0.05$.

4.3 Results

4.3.1 Visualizing intracellular Ca^{2+} and actin cytoskeleton in *ex vivo* osteocytes

Intracellular Ca^{2+} and actin network dynamics were successfully measured using confocal microscopy in both Fluo-8 + Lifeact osteocytes and GCaMP3 + Lifeact osteocytes (Figure 4.2).

Using 60x magnification, fields of view with as many as six individual osteocytes could be imaged. Sequential excitation of the two channels allowed for collection of time-lapse images without spectrum excitation/emission interference, and the dwell time between load cycles was sufficient to obtain both images after a given load cycle as well as capture the oscillatory characteristics of intracellular Ca^{2+} dynamics.

4.3.2 Osteocyte Ca^{2+} and contractile dynamics in response to biochemical stimuli

Both ATP and ionomycin elevated Ca^{2+} levels in the *ex vivo* Fluo-8+Lifeact and GCaMP3 + Lifeact osteocytes by at least two-fold (Figures 4.3 - 4.5). A decrease in actin network strain along the normal axes of the osteocytes was observed immediately following the increase in Ca^{2+} in response to each biochemical stimulus. For ATP-stimulated cells, these contractile dynamics were transient with Ca^{2+} elevation while in ionomycin-treated cells, contraction persisted throughout the elevation of intracellular Ca^{2+}. ATP and ionomycin induced a Ca^{2+} response in 73.3% and 90.9% of Fluo-8 + Lifeact cells, and a contraction was present in 54.5% and 50.0% of these cells that showed a Ca^{2+} response to ATP and ionomycin, respectively (Figure 4.3). ATP induced a transient increase of intracellular Ca^{2+} in 67% of GCaMP3 + Lifeact osteocytes, followed by contractions in 20% of responsive cells (Figure 4.4). Introduction of ionomycin resulted in step-elevation of Ca^{2+} in 83% of the GCaMP3 + Lifeact cells observed, of which 80% exhibited contractile behavior (Figure 4.5). Addition of media volume to the system via syringe had no quantifiable effect on GCaMP3 + Lifeact actin dynamics.

4.3.3 Osteocytes exhibit Ca^{2+}-dependent mechanosensitive contractions dependent upon sequence of mechanical load magnitude

Fluo-8 + Lifeact osteocytes demonstrated robust and repetitive Ca^{2+} spikes under cyclic mechanical loading (Figure 4.6A). Of cells that responded with mechanically-induced Ca^{2+}

peaks, 41.2% also exhibited a decrease and recovery in strain along at least one of the normal axes of the cell. On average, the magnitude of incremental contractile strain following a Ca^{2+} peak was 1.8%. Quantification of osteocyte Ca^{2+} oscillations and contractions over time reveals an average Ca^{2+} peak frequency of 0.012 ± 0.004 Hz and average contraction frequency of 0.0093 ± 0.003 Hz, which were not found to be significantly different in cells exhibiting both Ca^{2+} peaks and contractile events. Connecting individual Ca^{2+} peaks with subsequent contractions revealed the majority of Ca^{2+} peaks (>50%) were synchronous with a cytoskeletal contraction.

Osteocytes from Dmp1-Cre;Ai38$^{flx/flx}$;Lifeact mRFP$^{+/-}$ tibiae loaded at both 4 N and 8 N showed significantly amplified Ca^{2+} signaling at the higher load level as expected, regardless of load sequence (Figure 4.7)[19]. The average number of actin contractions along either axis of the cell were enhanced from an average of 2.3 ± 2.1 to 4.2 ± 3.1 contractions with increasing load sequence ($p<0.05$) (Figure 4.8). However, there were no significant differences in the number of contractile events between load levels with decreasing load sequence. Contractile events were dominated by those along the short axis of cells in both load levels of the decreasing load sequence, but not in the increasing load sequence. When comparing only the first load level from each sequence, representing an unpaired comparison of 4 N and 8 N events, there is only a significant difference in number of Ca^{2+} peaks between the two load levels while the number of contractile events remained consistent.

4.4 Discussion

Osteocytes are a cell type in which mechanosensitive potential as well as downstream mechanosignaling processes are dependent upon their unique actin cytoskeleton morphology and

connectivity in the bone matrix. Additionally, the mechanical stimuli experienced by these cells is dependent upon fluid flow in the lacunar-canalicular system (LCS) resulting from tissue-level compressive and tensile strains in the bone. Therefore, it is ideal to preserve the osteocyte network *in situ* and apply physiological loads to whole bone *ex vivo* when elucidating mechanotransduction mechanisms. We have successfully captured and quantified both Ca^{2+} and actin dynamics of *ex vivo* osteocytes and identified Ca^{2+}-dependent contractile behavior under various stimuli. Ca^{2+} signaling and contractile behavior in response to mechanical loading was first identified in tibial osteocytes of Lifeact $mRFP^{+/-}$ mice incubated with the intracellular Ca^{2+} indicator Fluo-8AM. This Ca^{2+} indicator has been used in previous studies of *ex vivo* osteocyte mechanosensitivity by our group and others for the robust visualization of Ca^{2+} dynamics of cells embedded in the dense bone tissue[19, 51, 107, 123]. When incubated with tibiae dissected from Lifeact $mRFP^{+/-}$ mice, in which F-actin tagged with mRFP via the Lifeact probe, simultaneous visualization of Ca^{2+} and actin network dynamics of individual osteocytes was possible. The frequency of Ca^{2+} signaling and contractions in response to mechanical loading as well as the synchrony of the two intracellular events were quantified for the first time using this experimental method.

Studies measuring intracellular dynamics at a high magnification and long imaging periods rely on stable intracellular fluorescent molecules while maintaining physiological integrity of the intracellular processes *in situ*. This study also builds upon the previously established protocol by developing and utilizing a novel mouse model with targeted expression of fluorescent proteins to observe intracellular Ca^{2+} and actin dynamics of live osteocytes within the bone tissue immediately after tissue explant. Dmp1-Cre;$Ai38^{flx/flx}$;Lifeact $mRFP^{+/-}$ mice were developed with the genetically encoded Ca^{2+} indicator GCaMP3 targeted to osteocytes which

also express Lifeact mRFP. Samples from these mice could be dissected and imaged immediately, eliminating the need for incubation periods with intracellular dyes to reach osteocytes deep within the bone tissue, thus minimizing time between explant and imaging. Indeed, the Ca^{2+} and contractile dynamics observed in GCaMP3 + Lifeact osteocytes in response to ATP, ionomycin, and mechanical loading are similar to those observed in Lifeact $mRFP^{+/-}$ osteocytes dyed with Fluo-8 AM. These triple transgenic samples could therefore be used for longer imaging sessions, allowing us to pair mechanical loading data and thus investigate mechanosensitivity of the intracellular dynamics in individual osteocytes.

This work is the first to demonstrate the a Ca^{2+}-dependent contractile mechanism in osteocytes *in situ*, with both Ca^{2+} peaks and actin network contractions being enhanced with load magnitude. Decreases in normal strains along the short and long axes of the cell were consistent with the contractile behavior we have previously observed in osteocytes *in vitro*. To confirm the dependence of actin contractions on Ca^{2+} dynamics rather than experimental artifact, ATP and ionomycin were used to chemically stimulate a Ca^{2+} response with different temporal profiles in the absence of mechanical load. Indeed, the normal strain profiles along the long and short axes of the osteocytes mimicked the Ca^{2+} dynamics for each stimulus. For example, ATP stimulated cells displayed a recovery to baseline in both Ca^{2+} and actin strain, demonstrating a reversible, phasic contraction. These phasic contractions were also coincident with Ca^{2+} peaks induced by mechanical loading. The frequencies of the load-induced Ca^{2+} transients and contractions were not found to be significantly different and the majority of these intracellular events were synchronous with one another in individual cells, suggesting their coordination in response to mechanical load.

The characteristics of the Ca^{2+}-dependent actin network contractions we identify in osteocytes *in situ* are similar to those observed *in vitro*. We have previously characterized contractile dynamics of single MLO-Y4 cells under both biochemical stimuli and fluid flow and showed a decrease and recovery of the average intracellular actin normal strain in the height of the cell to a magnitude of 0.015-0.02 strain[100]. Contractile events detected in Fluo-8 + Lifeact and GCaMP3 + Lifeact cells were of comparable magnitude and time scale. However, one benefit of our *ex vivo* experimental setup is the ability to observe multiple phasic contractions with prolonged mechanical loading cycles, whereas contractile dynamics were only recorded for 200 seconds at most in single cells *in vitro*. While other studies have identified multiple, phasic, tissue-level contractions corresponding to intracellular Ca^{2+} transients[124, 125], we are for the first time demonstrating Ca^{2+}-dependent contractile behavior in osteocytes at the cellular level.

This Ca^{2+}-dependent contractile mechanism in osteocytes could potentially contribute to other downstream mechanosensitive pathways, such as release of extracellular vesicles (EVs)[100]. Vesicle release has recently been highlighted as an important means of intercellular communication, whereby cells package proteins and genetic materials in EVs to shuttle their contents amongst one another[126]. EV release is stimulated by actomyosin contractility in endothelial cells[127] and facilitated by Ca^{2+}/actin dynamics in mast cells[115]. Considering actin networks have been implicated in mechanically-induced protein responses in osteocytes[128], it is feasible that osteocyte contractility may facilitate release of EVs containing key bone regulatory proteins *in situ*. Indeed, a recent morphological study showed strong co-localization of RANKL to vesicle-like structures in osteocytes and OPG-positive structures in the canaliculi, indicating intracellular transport of the proteins in the canaliculi[129]. This is further confirmed by

multiplexed confocal imaging of *in situ* osteocytes revealing vesicle-like structures present throughout the bone matrix surrounding the osteocytes and in-between dendrites[69].

Our paired data of intracellular dynamics at two mechanical load magnitudes indicate that the mechanosensitivity of the osteocyte contractions is dependent upon loading history. Increasing load sequences highlight the differential contractile responses between load levels in individual cells while decreasing load sequences appear to saturate the contractile mechanism, as contractions are not significantly different from the 8 N load to the 4 N load. These differential responses have previously been observed in other bone cell types. For example, primary osteoblasts have been shown to exhibit different anabolic gene expression and protein production responses to increasing/decreasing fluid shear stress *in vitro*[130]. Consideration of additional load levels and configurations would provide further insight into dependence of the responses on loading history. Differences in contractions between cell axes also suggest dependence of the mechanism on osteocyte morphology, which warrants further exploration.

Future work will determine relative contributions of mechanical loading and Ca^{2+} dynamics on actin contractions using actin stabilizing compounds and inhibitors of Ca^{2+} signaling. Previous studies have utilized several inhibitors of Ca^{2+} signaling in determining relevant pathways contributing to oscillatory responses to load, suggesting that antagonists for the ATP pathway and the endoplasmic reticulum would be most efficient in inhibiting Ca^{2+} responses in osteocytes and studying the effect on actin network contractions[19, 47]. Furthermore, jasplakinolide has been used *in vitro* to stabilize actin filaments by accelerating actin polymerization, thereby inhibiting depolymerization[131-133]. Unpublished work from our group has demonstrated inhibition of contractile dynamics without impairing Ca^{2+} responses in MLO-Y4 cells *in vitro* using jasplakinolide[113]. Thus, jasplakinolide would be useful for future studies aiming to delineate the roles of Ca^{2+} oscillations and contractility in downstream osteocyte functions *in situ*.

4.5 Conclusions

Biochemical and fluid flow-induced Ca^{2+} responses have been shown to induce contractions of the actin cytoskeleton in osteocytes *in vitro*. Here, we confirm this functional consequence of Ca^{2+} signaling in osteocytes in their native 3D network by expanding upon our *ex vivo* model of osteocyte mechanosignaling to simultaneously visualize intracellular Ca^{2+} and the actin cytoskeleton in single cells in response to whole-bone loading using transgenic mice. We have identified contractile events corresponding to load-induced Ca^{2+} peaks *in situ* while demonstrating a potential sensitivity to mechanical loading history. This Ca^{2+}-dependent contractility is a potential target for therapies for conditions in which osteocyte mechanosensitivity is diminished, such as age-induced osteoporosis.

4.6 Tables

		ATP	Ionomycin	Mechanical Loading (8N)	Mechanical Loading (4N → 8N)	Mechanical Loading (8N → 4N)
Fluo-8 + Lifeact	Tibia Samples	6	14	11	--	--
	Osteocytes	15	33	19	--	--
GCaMP3 + Lifeact	Tibia Samples	2	2	--	4	3
	Osteocytes	6	6	--	6	6

Table 4.1 Tibia samples and osteocytes analyzed for intracellular responses. In Lifeact mRFP mice tibiae dyed with Fluo-8 AM (Fluo-8 + Lifeact), intracellular responses were analyzed in cells under biochemical stimulation by ATP and ionomycin, as well as mechanical loading at an 8 N load magnitude. Osteocytes from Dmp1-Cre;Ai38$^{flx/flx}$;Lifeact mRFP$^{+/-}$ mice (GCaMP3 + Lifeact) were analyzed in response to biochemical stimulation as well as one of two mechanical loading sequences (increasing or decreasing).

4.7 Figures

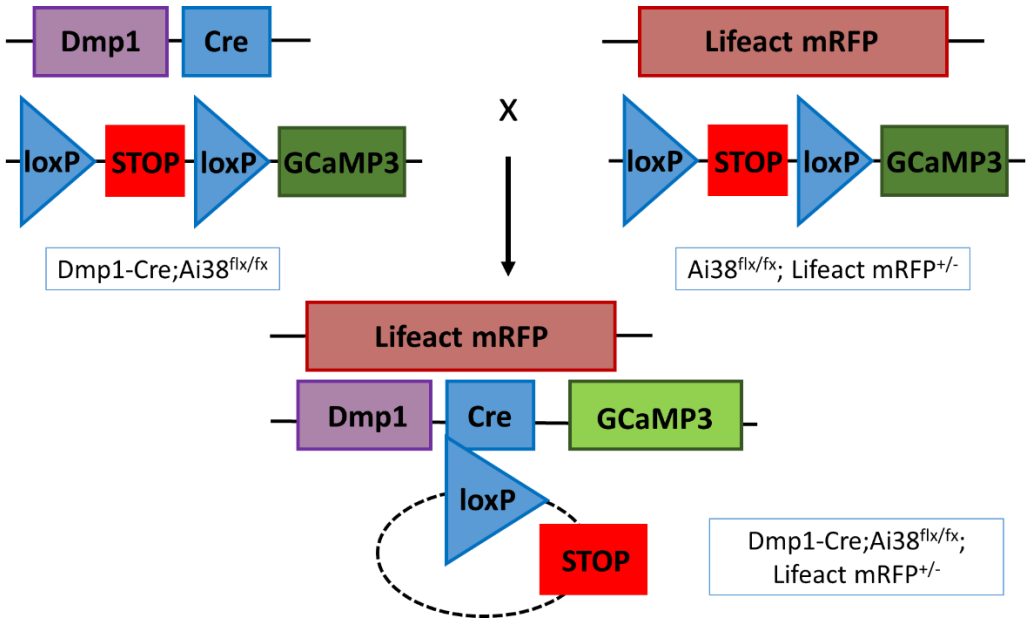

Figure 4.1 Gene targeting strategy used to generate Dmp1-Cre;Ai38$^{flx/flx}$;Lifeact mRFP$^{+/-}$ mice. The Ai38 floxed GCaMP3 reporter mouse line is Cre-dependent via a *lox-stop-lox* cassette. Osteocyte-specific GCaMP3 expression is achieved by crossing the Ai38 reporter mice with Dmp1-Cre mice in which Cre recombinase is driven by the osteocyte-specific protein Dmp1. Dmp1-Cre;Ai38$^{flx/flx}$ mice are bred to Ai38$^{flx/flx}$;Lifeact mRFP$^{+/-}$ mice, in which F-actin is tagged to RFP via the Lifeact probe, resulting in mice with osteocytes expressing both GCaMP3 and Lifeact mRFP.

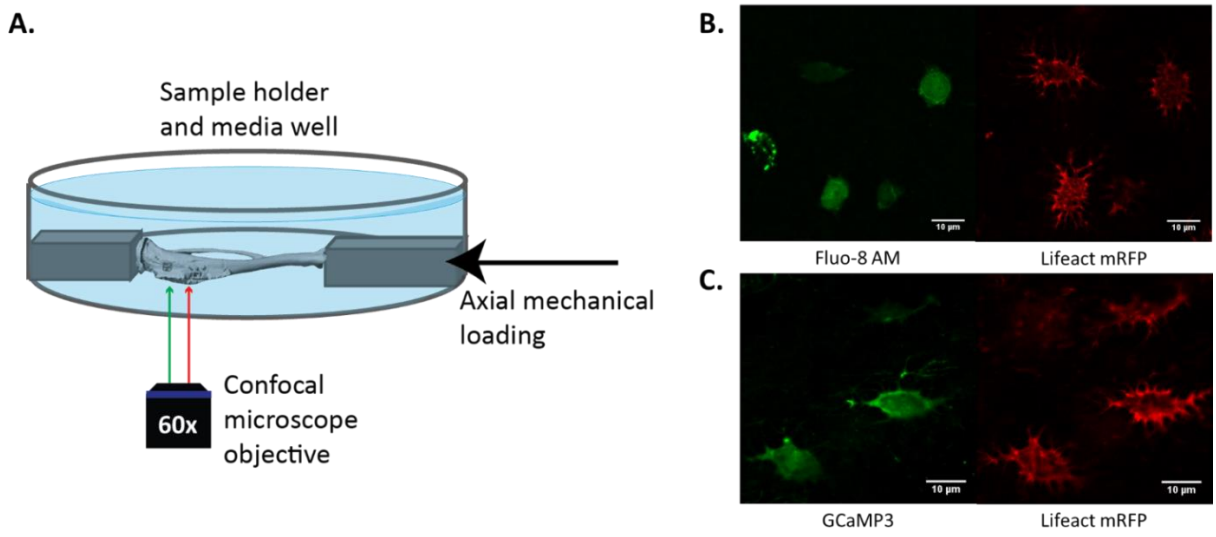

Figure 4.2 Visualization of intracellular Ca^{2+} and actin cytoskeleton in *ex vivo* osteocytes. A. Confocal microscopy is used with a custom mechanical loading system to capture osteocyte intracellular responses to whole-bone mechanical loading. Intracellular Ca^{2+} dynamics are visualized using either **B.** incubation of tibia samples with the intracellular Ca^{2+} dye Fluo-8 AM, or **C.** osteocyte-specific expression of GCaMP3. Both experimental methods capture osteocyte actin network dynamics via expression of Lifeact mRFP tagged to F-actin.

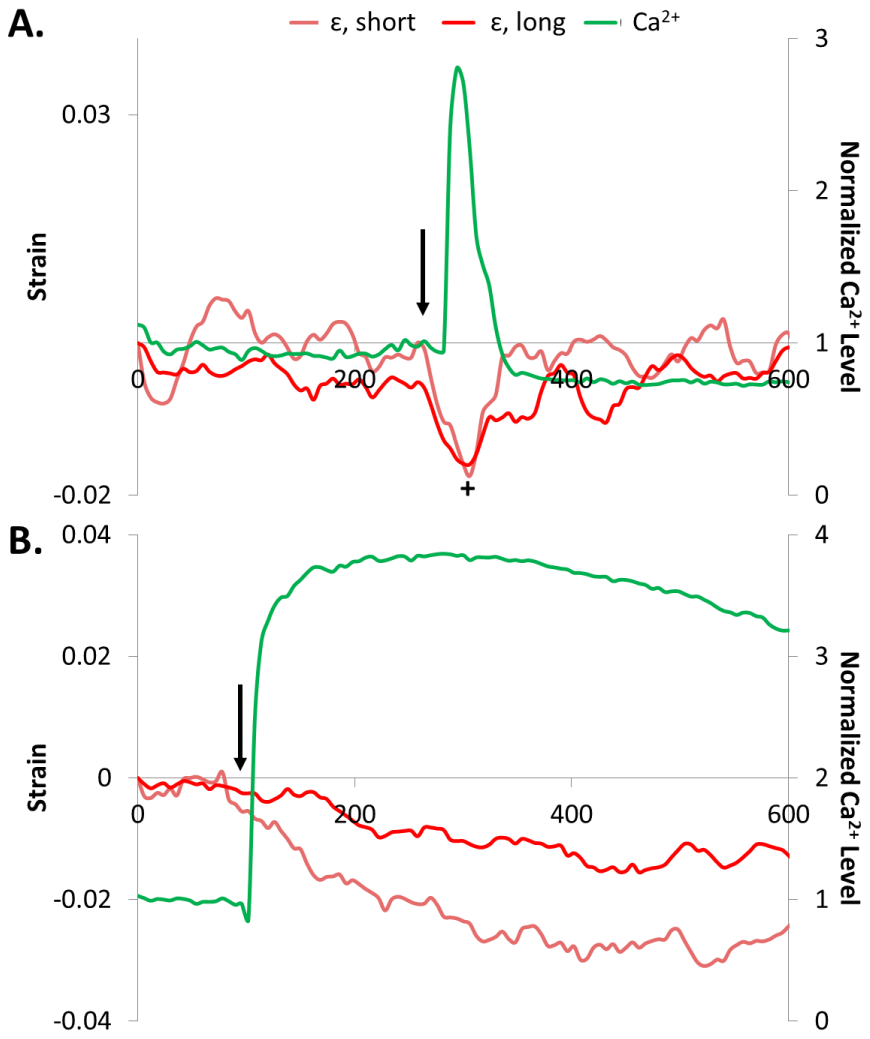

Figure 4.3 Biochemically-induced Ca^{2+} responses and subsequent actin dynamics in Fluo-8 + Lifeact osteocytes. Representative time courses of intracellular Ca^{2+} and actin network strain along the short (ε, short) and long (ε, long) axes of osteocytes stimulated by addition of either **A.** 20 mM ATP (n=15 cells), or **B.** 20 μM ionomycin (n=33 cells) to the experimental system, indicated by arrows. A contractile event is identified following the peak in intracellular Ca^{2+} in response to ATP (+) while the contraction in response to ionomycin-induced Ca^{2+} influx begins immediately following the Ca^{2+} response.

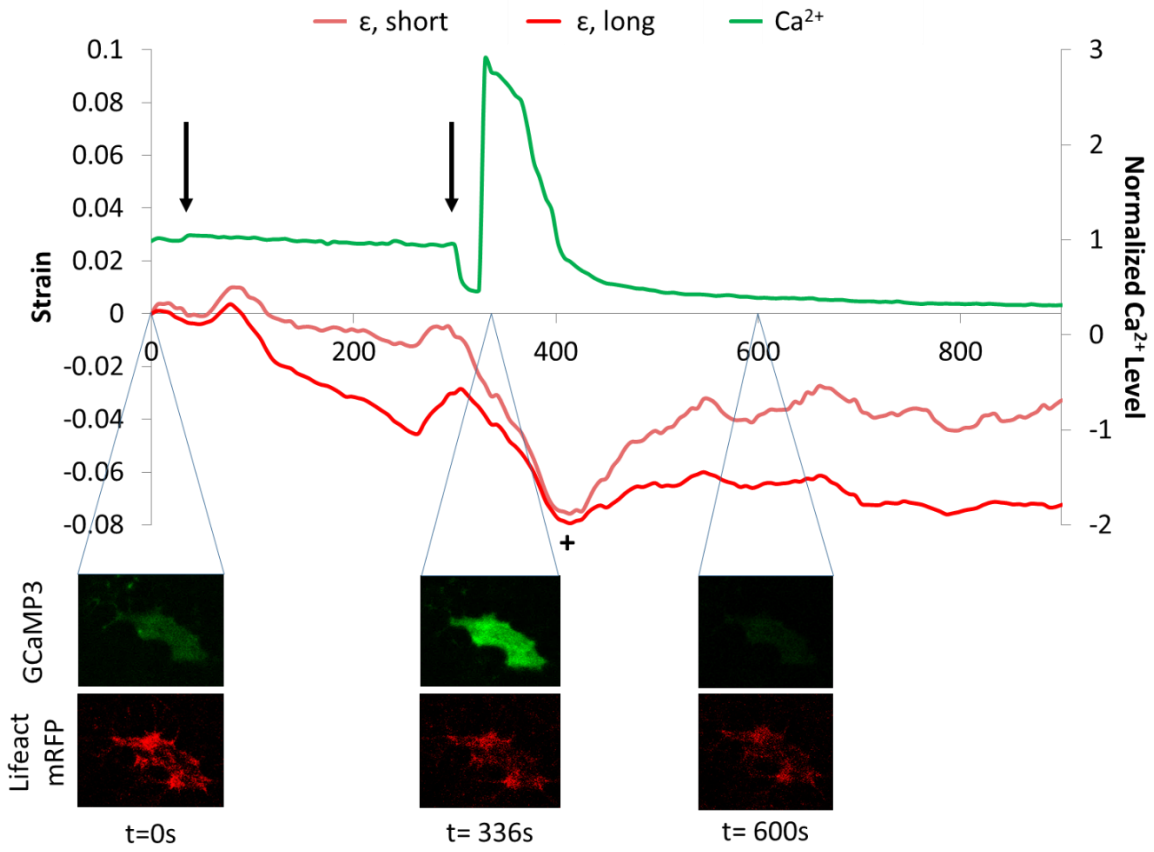

Figure 4.4 ATP-induced Ca^{2+} responses and subsequent actin dynamics in GCaMP3 + Lifeact osteocytes. Representative time courses of intracellular Ca^{2+} and actin network strain along the short (ε, short) and long (ε, long) axes of an osteocyte stimulated by the addition 10 mM ATP (n= 6 cells). Addition of media control and biochemical stimulus are indicated by arrows. Time-lapse images of GCaMP3 and Lifeact mRFP for the given osteocyte are displayed at time points before (t=0 s) and immediately after addition of ATP (t=336 s), and at return to baseline (t=600s). A contractile event is identified following the peak in intracellular Ca^{2+} (+).

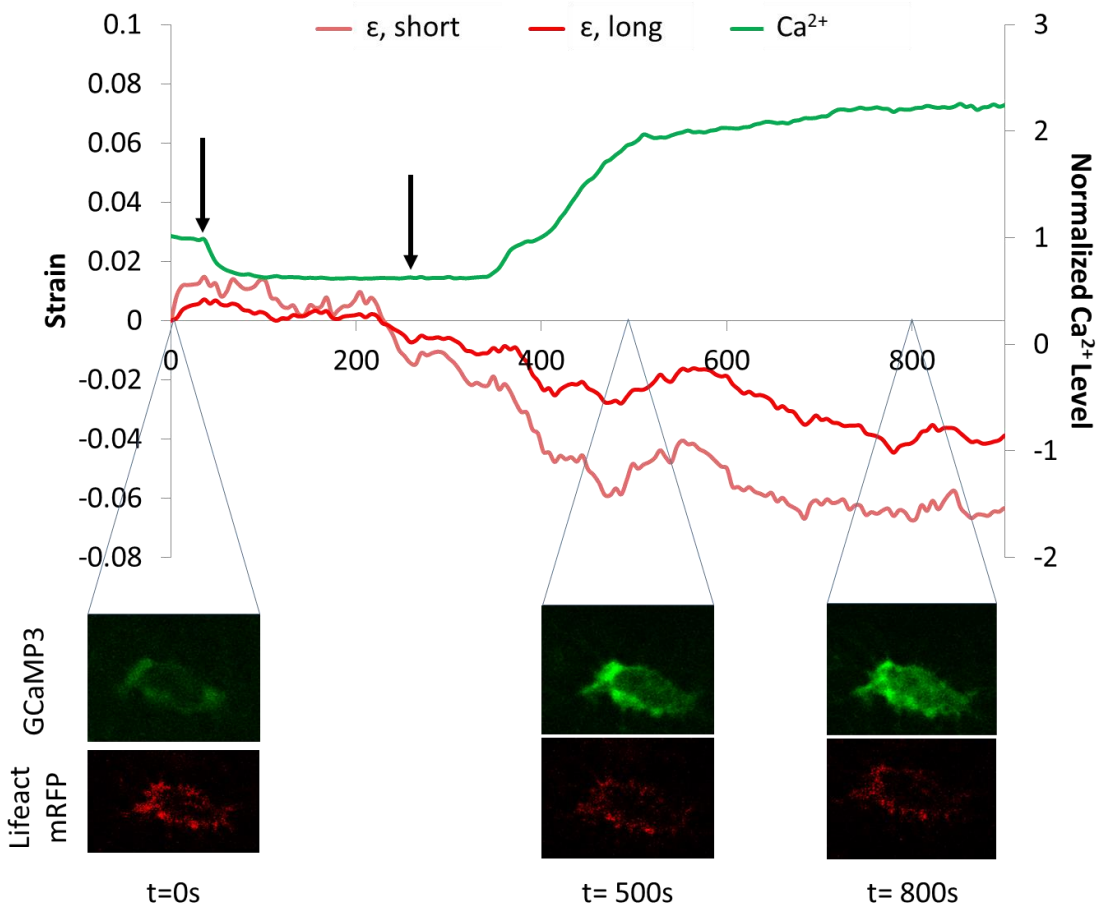

Figure 4.5 Ionomycin-induced Ca^{2+} responses and subsequent actin dynamics in GCaMP3 + Lifeact osteocytes. Representative time courses of intracellular Ca^{2+} and actin network strain along the short (ε, short) and long (ε, long) axes of an osteocyte stimulated by the addition 10 μM ionomycin (n= 6 cells). Addition of media control and biochemical stimulus are indicated by arrows. Time-lapse images of GCaMP3 and Lifeact mRFP for the given osteocyte are displayed at time points before (t=0 s) and after addition of ionomycin (t=500 s), and at a point of sustained elevated Ca^{2+} (t=800s). Contractile dynamics in both axes of the cell initiate following the initiation of Ca^{2+} response.

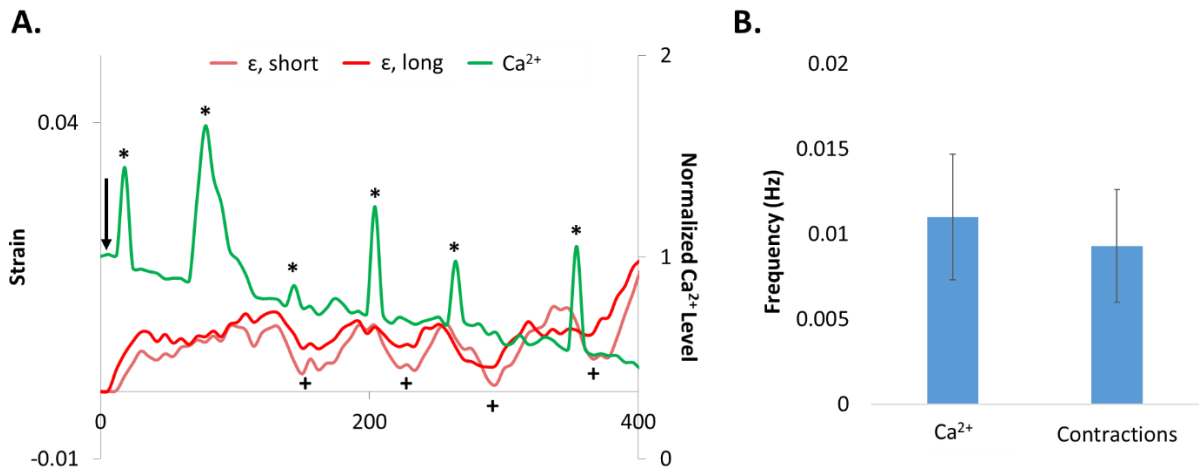

Figure 4.6 Mechanically-induced Ca^{2+} responses and subsequent actin dynamics in Fluo-8 + Lifeact osteocytes. A. Representative time courses of intracellular Ca^{2+} and actin network strain along the short (ε, short) and long (ε, long) axes of an osteocyte under 8 N of cyclic mechanical loading applied to the whole tibia. Contractile events (+) are identified following peaks in intracellular Ca^{2+} (*). Loading initiation indicated by arrow. **B.** The frequencies of Ca^{2+} peaks and actin contractile events are quantified and compared for cells exhibiting both Ca^{2+} responses and contractions (n = 9 cells, paired Student's t-test).

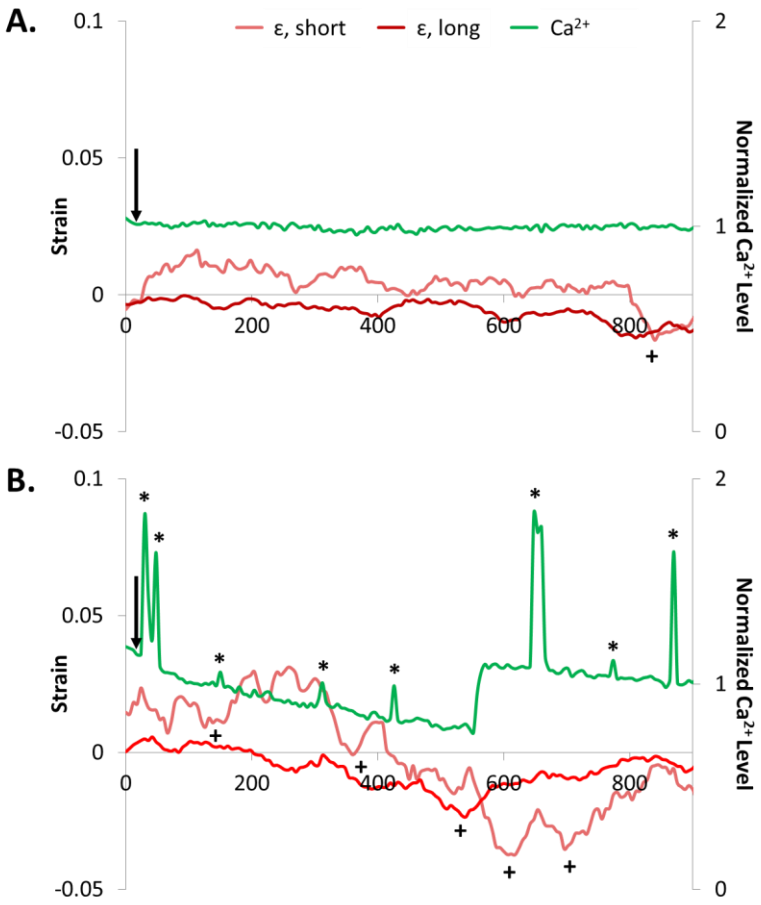

Figure 4.7 Mechanosensitive Ca^{2+} responses and actin contractions in GCaMP3 + Lifeact osteocytes. Representative time courses of intracellular Ca^{2+} and actin network strain along the short (ε, short) and long (ε, long) axes of an osteocyte under both **A.** 4 N of cyclic mechanical loading, or **B.** 8 N of cyclic mechanical loading applied to the whole tibia. These intracellular dynamics are considered responses to an increasing load sequence for this cell. Contractile events (+) are identified following peaks in intracellular Ca^{2+} (*). Loading initiation indicated by arrow.

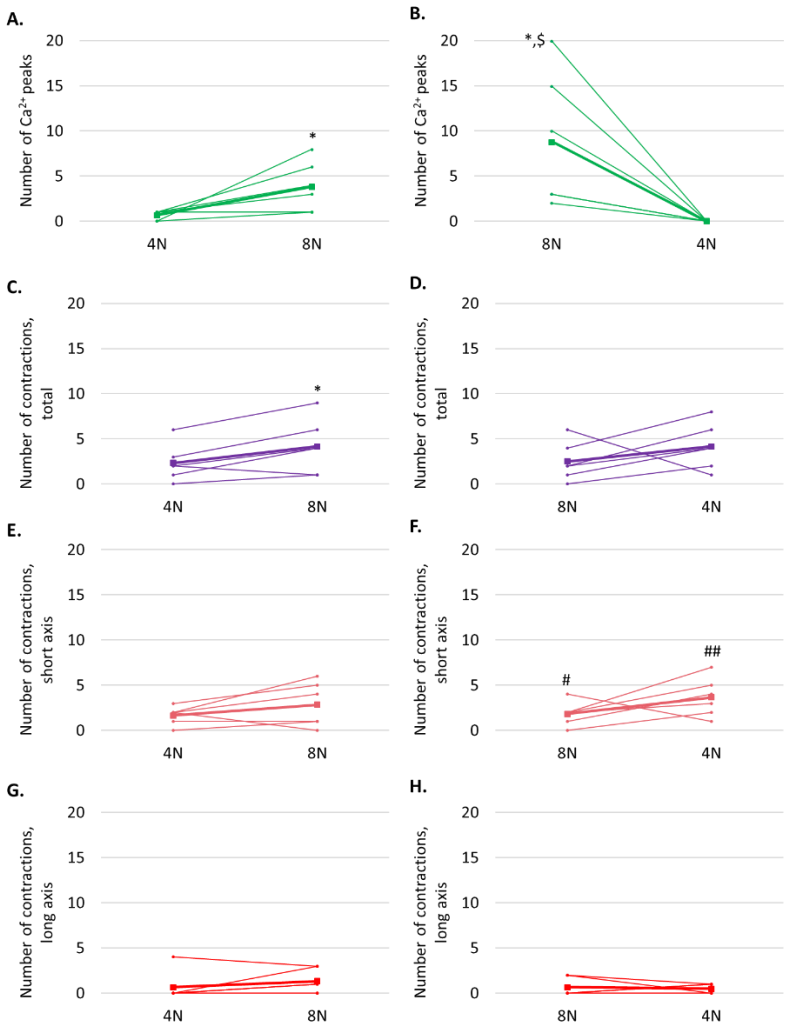

Figure 4.8 ***Ex vivo*** **osteocyte intracellular Ca^{2+} and contractile events under different loading sequences.** Paired data are shown for osteocytes experiencing increasing (n=6 cells) and decreasing (n=6 cells) load sequences, with the average events between load levels shown as a bolded line. The number of intracellular Ca^{2+} peaks (**A, B**) and total intracellular contractions (**C, D**) are evaluated for each load level in each loading sequence. Contractions are further characterized in increasing and decreasing load sequences by those occurring along the short (**E, F**) and long axes (**G, H**) of individual osteocytes. *$p<0.05$, between load levels within a load sequence (paired Student's t-test). $^{\#}p<0.05$, $^{\#\#}p<0.01$, short axis vs. long axis contractions within a load level (paired Student's t-test). $p<0.05, between first load levels applied (Student's t-test).

Chapter 5: Conclusion

5.1 Summary

Surmounting evidence over the past few decades has solidified the osteocyte as the primary mechanosensor in bone. This cell type is primed for this role by its longevity, distribution as an interconnected network throughout the bone tissue, stellate morphology, and mechanosensitive production of key bone regulatory proteins. In fact, the development of osteoporosis is thought to stem from an imbalance of osteocyte-mediated bone resorption by osteoclasts and bone formation by osteoblasts, which implies a disruption of normal mechanotransduction processes. A particularly robust mechanosensitive phenomenon in osteocytes that is observable in real time in systems of multiple scales is intracellular calcium (Ca^{2+}) signaling. Osteocyte cell networks both *in vitro* and *ex vivo* exhibit robust oscillations in intracellular Ca^{2+} under mechanical stimulation and are more responsive than osteoblasts, further supporting their role as the major mechanosensing cell type in bone. Thus, the real-time mechanosensitive potential of osteocytes can potentially be characterized in a variety of contexts using an *ex vivo* murine tibia model of osteocyte Ca^{2+} responses to whole-bone loading. This body of work explores *ex vivo* osteocyte Ca^{2+} signaling in a model of aging as well as in mice undergoing a recently-approved treatment for osteoporosis.

The first chapter of this thesis explored the possibility of diminished osteocyte mechanosensing with age, supported by evidence of a blunted anabolic response to mechanical loading *in vivo* in aged mice. Tibiae were dissected from 5-month-old (young-adult) and 22-month-old (aged) mice and incubated with Fluo-8 AM to image real-time osteocyte Ca^{2+} dynamics in response to whole-bone mechanical loading using confocal microscopy. Tibia from

aged mice demonstrated a significantly thinner cortex than young-adult mice, confirming age-induced bone loss. When loading was applied to match 1500 με strain at the anteromedial cortical bone surface, osteocytes in this region responded with oscillatory Ca^{2+} peaks; however, fewer cells demonstrated Ca^{2+} responses in aged mice and the initiation of these responses was significantly delayed. Additionally, synchrony analysis revealed an inverse linear relationship between responsive cell pairs and cell-cell distance in 5-month-old mice that was absent in 22-month-old mice. This suggests a diminished mechanosensitivity in aged osteocytes and lack of ability to generate coordinated Ca^{2+} responses to mechanical load that are seen in young-adult mice, possibly due to the reduction in osteocyte cell density and dendricity seen in aged female mice or a blunted mechanosensitive ATP pathway response upstream of Ca^{2+} signaling. This evidence regarding the real-time mechanosensitive potential of aged osteocytes compared to young-adult osteocytes provides insight into the impairment of long-term bone formation processes with aging.

Chapter 3 of this work investigated the effects of a newly-approved treatment for osteoporosis, commonly influenced by age-induced bone loss, on osteocyte mechanosensing. The rapid increase in bone mass resulting from initial treatment with sclerostin antibody (Scl-Ab) may alter both the whole-bone and local mechanical environments of osteocytes in the bone matrix, resulting in altered mechanosensitivity and possibly contributing to the bone formation response return to steady state with long-term treatment. To investigate this, mice were treated with either vehicle, short-term, or long-term Scl-Ab for eight weeks. Mice were sacrificed, and tibiae were dissected for simultaneous *ex vivo* mechanical loading and osteocyte Ca^{2+} imaging. The bone formation marker P1NP was probed at different time points throughout the treatment period to confirm the blunting of serum P1NP response to Scl-Ab doses with long-term

treatment. Micro-CT analyses of cortical bone revealed a rapid initial increase of BMD and cortical thickness with Scl-Ab treatment, with decreasing rates of bone accrual under long-term treatment as expected. Indeed, increased BMD following Scl-Ab treatment resulted in differences in force-strain relationships in the anteromedial cortical bone as measured by *ex vivo* tibial strain gauging. When cyclic mechanical loading was applied to tibia from all treatment groups at a 10 N magnitude, there were no significant differences in osteocyte Ca^{2+} response parameters, suggesting maintained mechanosensitivity despite accrual of bone mass and resulting differences in strain magnitudes. However, when loading was applied to match 2000 με at the anteromedial cortical bone surface in all samples, osteocytes from short-term treated mice exhibited fewer responsive osteocytes with delayed Ca^{2+} signaling. Alizarin red intensity analysis in the field of view of osteocyte imaging revealed that newly calcified bone was more evident in short-term treated bones than in long-term or vehicle groups. This suggests that osteocytes from the short-term treatment group are embedded in newly-formed cortical bone, which may present altered local mechanical properties of newly-mineralized bone or a less-mature osteocyte phenotype compared to vehicle or long-term treated osteocytes. These observations further our understanding of the mechanisms of different phases of bone formation responses to Scl-Ab treatment.

Chapter 4 seeks to identify a functional consequence of the mechanically-induced Ca^{2+} responses that have been characterized in Chapters 2 and 3 of this work, as well as by others, and its mechanosensitive potential. Most recently, our lab has demonstrated that mechanical stimulation of osteocytes activates Ca^{2+}-dependent contractions and enhances the production and release of extracellular vesicles containing bone regulatory proteins *in vitro*. We hypothesized that load-induced Ca^{2+} oscillations yield similarly mechanosensitive actin contractions in

osteocytes residing in their native 3D network, and therefore enhanced our established system for *ex vivo* loading of whole bone and simultaneous imaging of Ca^{2+} to include visualization of the actin cytoskeleton network in live cortical osteocytes. *Ex vivo* tibiae from Lifeact mice dyed with Fluo-8 AM (Fluo-8 + Lifeact) as well as triple transgenic Dmp1-Cre;Ai38$^{flx/flx}$;Lifeact mRFP$^{+/-}$ (GCaMP3 + Lifeact) were utilized to simultaneously image intracellular Ca^{2+} and actin network dynamics in osteocytes *in situ*. ATP and ionomycin were used to biochemically-induce Ca^{2+} responses in osteocytes of *ex vivo* tibiae and confirm Ca^{2+}-dependency of the contractile mechanism in both Fluo-8 + Lifeact and GCaMP3 + Lifeact osteocytes. Osteocytes from both mouse models exhibited Ca^{2+} oscillations and contractile events in response to whole-bone mechanical loading. In GCaMP3 + Lifeact mice, differential contractile responses were exhibited between increasing and decreasing loading sequences in individual osteocytes. This work improves our previously established protocol via a novel mouse model with targeted expression of fluorescent proteins to observe intracellular Ca^{2+} and actin dynamics of live osteocytes within the bone tissue immediately after tissue explant, as Ca^{2+} and contractile dynamics observed in response to ATP, ionomycin, and mechanical loading are similar to those observed in Fluo-8 AM + Lifeact osteocytes. Using this model for improved real-time study of single cells *in situ*, this work is the first to demonstrate the mechanosensitivity of a Ca^{2+}-dependent contractile mechanism in osteocytes, with both Ca^{2+} peaks and actin network contractions being enhanced with load magnitude. This Ca^{2+}-dependent contractile mechanism may be a potential target for therapies for conditions in which osteocyte mechanosensitivity is diminished, such as age-induced osteoporosis.

5.2 Future work

Overall, based on our success in observing mechanically-induced Ca^{2+} oscillations in osteocytes from *ex vivo* Dmp1-Cre;Ai38$^{flx/flx}$;Lifeact mRFP$^{+/-}$ mice tibiae comparable to those demonstrated by Fluo-8 AM-dyed osteocytes, a logical next step would be to utilize Dmp1-Cre;Ai38$^{flx/flx}$ mice in further studies of osteocyte Ca^{2+} signaling *ex vivo*. These mice would express the GCaMP3 Ca^{2+} indicator targeted specifically to osteocytes, eliminating limitations of Fluo-8 AM which include dye penetration depth and dye compartmentalization by cell metabolic processes during the loading and imaging period. This would also minimize experimental manipulation and incubation time of tibia samples, make it easier to perform Ca^{2+} signaling analyses in a more physiological manner. This condensed experimental timeline would most benefit the Scl-Ab studies in which sacrifice, dissection, and imaging of tibia samples from all treatment groups is ideally carried out in as short a time as possible. Additionally, the GCaMP3 mouse model would be particularly beneficial when applied to the aged osteocyte mechanosensing studies and would help determine if the low number of cells analyzed in Chapter 2 is due to lower osteocyte density in the aged mice, rather than the impaired ability of aged osteocytes to take up and rapidly esterify Fluo-8.

Given the diminished mechanosignaling properties in aged mice, it would be of interest to determine the mechanism responsible by using agonists for pathways that we know to be critical for sustaining load-induced Ca^{2+} oscillations, such as ATP. Furthermore, methods of preserving the osteocyte network as the mice age, either through pharmacological means or transgenic mouse models, would provide insight into the role of diminished osteocyte cell density and connectivity in maintaining and coordinating Ca^{2+} responses. The nature of the fluid flow in the lacunar-canalicular system (LCS) of aged osteocyte networks would also be an

interesting point for exploration through computational modeling, as fewer cells in the lacunae and reduced dendricity throughout the canaliculi may alter the fluid flow dynamics responsible for inducing osteocyte responses to whole-bone loading, including intracellular Ca^{2+}.

In further studies of Scl-Ab treatment, investigation of bone modeling and remodeling processes at the periosteum would strengthen the connection between rapid mineralization of osteocytes under short-term treatment and diminished mechanosensitivity of osteocyte Ca^{2+} signaling in the region of interest. This could be accomplished through temporal analyses of weekly *in vivo* micro-CT scans of the tibia anteromedial cortical bone surface. These micro-CT scans could also be used to generate computational finite element models, which could be used to support our experimental measures of anteromedial cortical bone strain. Identification of rapid modeling processes at the periosteum would confirm that the osteocytes visualized during cyclic loading and Ca^{2+} imaging are embedded as a result of the initial increase in bone formation response with short-term Scl-Ab treatment. Additionally, comparison of morphological characteristics of *in situ* osteocytes between treatment groups may provide some additional evidence for the differences in mechanosensitive potential observed in osteocytes from short-term Scl-Ab treated animals.

Based on our characterization of load-induced Ca^{2+} responses and downstream contractile events, future work would ideally be focused on probing points upstream and downstream of these mechanisms. Further study to determine relative contributions of mechanical loading and Ca^{2+} dynamics on actin contractions using actin stabilizing compounds and inhibitors of Ca^{2+} signaling would bring deeper understanding to this mechanism and its possible downstream contributions to bone formation processes. Additionally, investigating the contribution of mechanically-induced, Ca^{2+}-dependent osteocyte contractions to the release of extracellular

vesicles *in situ* would confirm our previously-published *in vitro* findings and provide further evidence for extracellular vesicle release as a means of cell-cell communication in bone and a mechanism by which osteocytes direct bone formation processes.

5.3 Significance

This broader impact of this body of work is the advancement in understanding of osteocyte mechanosensing in clinically-relevant contexts. It is thought the pathology of osteoporosis stems from impaired osteocyte mechanosensing and directing of bone resorption relative to formation. The studies in Chapter 2 provide, for the first time, a direct measure of this diminished mechanosensing in real time by comparing osteocyte Ca^{2+} signaling in tibia from aged and young-adult mice. With prior knowledge of the role of Ca^{2+} signaling in anabolic bone formation responses to load, dampened Ca^{2+} signaling in aged osteocytes may contribute to the dampened anabolic response to mechanical loading seen in longer-term, tissue-level studies. Previous work identifying the pathways responsible for load-induced Ca^{2+} signaling in osteocytes provides possible points of pharmacological agonist intervention to rescue the reduced mechanosignaling with aging.

While the effects of antibody to sclerostin, recently approved by the U.S. Food and Drug Administration as EVENITY™ for treatment of osteoporosis, on bone formation and resorption have been thoroughly characterized in animal studies as well as clinical trials, our work in Chapter 3 uncovers real-time mechanosensing measures in osteocytes from animals undergoing different treatment timelines. By showing that osteocyte mechanosensitivity is maintained in all treatment groups apart from strain-matched short-term treated samples, we demonstrate the distinct phases of the bone formation response to the drug at a cellular level. Having identified

diminished mechanosensing in newly-mineralized osteocytes, we now turn our attention to other possible Wnt antagonists or additional pathways responsible for self-regulation of the bone formation response, which may be addressed with supplemental therapies to EVENITY™.

Ca^{2+}-dependent contractility has been previously and thoroughly characterized in a variety of cell types. However, this mechanism has yet to be demonstrated in the osteocyte. This body of work not only confirms this common physiological mechanism for the first time in osteocytes *in situ*, but it provides evidence for the mechanosensitivity of Ca^{2+}-dependent actin network contractions. Our work presents this mechanism as a potential link between osteocytes sensing mechanical loads and transducing changes in mechanical stimuli to bone effector cells such as osteoblasts and osteoclasts, therefore allowing for another point of intervention in treating diseases that are thought to develop as a result of reduced osteocyte mechanotransduction.

References

1. Withers B. Lovely Day. Menagerie; 1977.

2. Frost HM. Wolff's Law and bone's structural adaptations to mechanical usage: an overview for clinicians. *Angle Orthod* 1994; **64**(3)**:** 175-188.

3. Haapasalo H, Kontulainen S, Sievanen H, Kannus P, Jarvinen M, Vuori I. Exercise-induced bone gain is due to enlargement in bone size without a change in volumetric bone density: a peripheral quantitative computed tomography study of the upper arms of male tennis players. *Bone* 2000 Sep; **27**(3)**:** 351-357.

4. Taaffe DR, Robinson TL, Snow CM, Marcus R. High-impact exercise promotes bone gain in well-trained female athletes. *J Bone Miner Res* 1997 Feb; **12**(2)**:** 255-260.

5. Kazakia GJ, Tjong W, Nirody JA, Burghardt AJ, Carballido-Gamio J, Patsch JM, *et al.* The influence of disuse on bone microstructure and mechanics assessed by HR-pQCT. *Bone* 2014 6//; **63**(0)**:** 132-140.

6. Smith SM, Abrams SA, Davis-Street JE, Heer M, O'Brien KO, Wastney ME, *et al.* Fifty Years of Human Space Travel: Implications for Bone and Calcium Research. *Annual Review of Nutrition* 2014; **34**(1)**:** 377-400.

7. Al Nazer R, Lanovaz J, Kawalilak C, Johnston JD, Kontulainen S. Direct in vivo strain measurements in human bone-a systematic literature review. *J Biomech* 2012 Jan 3; **45**(1)**:** 27-40.

8. Franz-Odendaal TA, Hall BK, Witten PE. Buried alive: how osteoblasts become osteocytes. *Dev Dyn* 2006 Jan; **235**(1)**:** 176-190.

9. Bonewald LF, Johnson ML. Osteocytes, mechanosensing and Wnt signaling. *Bone* 2008 Apr; **42**(4)**:** 606-615.

10. Lanyon LE, Hampson WG, Goodship AE, Shah JS. Bone deformation recorded in vivo from strain gauges attached to the human tibial shaft. *Acta Orthop Scand* 1975 May; **46**(2)**:** 256-268.

11. Srinivasan S, Agans SC, King KA, Moy NY, Poliachik SL, Gross TS. Enabling bone formation in the aged skeleton via rest-inserted mechanical loading. *Bone* 2003 Dec; **33**(6)**:** 946-955.

12. Rubin CT, Lanyon LE. Regulation of bone mass by mechanical strain magnitude. *Calcified tissue international* 1985 Jul; **37**(4)**:** 411-417.

13. Fritton SP, Weinbaum S. Fluid and Solute Transport in Bone: Flow-Induced Mechanotransduction. *Annu Rev Fluid Mech* 2009 Jan 1; **41:** 347-374.

14. Riddle RC, Donahue HJ. From streaming-potentials to shear stress: 25 years of bone cell mechanotransduction. *J Orthop Res* 2009 Feb; **27**(2)**:** 143-149.

15. Weinbaum S, Cowin SC, Zeng Y. A model for the excitation of osteocytes by mechanical loading-induced bone fluid shear stresses. *J Biomech* 1994 Mar; **27**(3)**:** 339-360.

16. Piekarski K, Munro M. Transport mechanism operating between blood supply and osteocytes in long bones. *Nature* 1977 Sep 1; **269**(5623)**:** 80-82.

17. Price C, Zhou X, Li W, Wang L. Real-time measurement of solute transport within the lacunar-canalicular system of mechanically loaded bone: direct evidence for load-induced fluid flow. *J Bone Miner Res* 2011 Feb; **26**(2)**:** 277-285.

18. Wang L, Wang Y, Han Y, Henderson SC, Majeska RJ, Weinbaum S, *et al.* In situ measurement of solute transport in the bone lacunar-canalicular system. *Proc Natl Acad Sci U S A* 2005 Aug 16; **102**(33)**:** 11911-11916.

19. Jing D, Baik AD, Lu XL, Zhou B, Lai X, Wang L, *et al.* In situ intracellular calcium oscillations in osteocytes in intact mouse long bones under dynamic mechanical loading. *The FASEB Journal* 2014; **28**(4)**:** 1582-1592.

20. Tatsumi S, Ishii K, Amizuka N, Li M, Kobayashi T, Kohno K, *et al.* Targeted ablation of osteocytes induces osteoporosis with defective mechanotransduction. *Cell metabolism* 2007 Jun; **5**(6)**:** 464-475.

21. Robling AG, Niziolek PJ, Baldridge LA, Condon KW, Allen MR, Alam I, *et al.* Mechanical stimulation of bone in vivo reduces osteocyte expression of Sost/sclerostin. *J Biol Chem* 2008 Feb 29; **283**(9)**:** 5866-5875.

22. Xiong J, Onal M, Jilka RL, Weinstein RS, Manolagas SC, O'Brien CA. Matrix-embedded cells control osteoclast formation. *Nature medicine* 2011 Sep 11; **17**(10)**:** 1235-1241.

23. Nakashima T, Hayashi M, Fukunaga T, Kurata K, Oh-Hora M, Feng JQ, *et al.* Evidence for osteocyte regulation of bone homeostasis through RANKL expression. *Nature medicine* 2011 Sep 11; **17**(10)**:** 1231-1234.

24. Morse A, McDonald MM, Kelly NH, Melville KM, Schindeler A, Kramer I, *et al.* Mechanical load increases in bone formation via a sclerostin-independent pathway. *J Bone Miner Res* 2014 Nov; **29**(11)**:** 2456-2467.

25. Moustafa A, Sugiyama T, Prasad J, Zaman G, Gross TS, Lanyon LE, *et al.* Mechanical loading-related changes in osteocyte sclerostin expression in mice are more closely associated with the subsequent osteogenic response than the peak strains engendered. *Osteoporos Int* 2012 Apr; **23**(4)**:** 1225-1234.

26. Spatz JM, Ellman R, Cloutier AM, Louis L, van Vliet M, Suva LJ, *et al.* Sclerostin antibody inhibits skeletal deterioration due to reduced mechanical loading. *J Bone Miner Res* 2013 Apr; **28**(4)**:** 865-874.

27. Milovanovic P, Zimmermann EA, Hahn M, Djonic D, Puschel K, Djuric M, *et al.* Osteocytic canalicular networks: morphological implications for altered mechanosensitivity. *ACS nano* 2013 Sep 24; **7**(9)**:** 7542-7551.

28. Holguin N, Brodt MD, Silva MJ. Activation of Wnt Signaling by Mechanical Loading Is Impaired in the Bone of Old Mice. *J Bone Miner Res* 2016 Dec; **31**(12)**:** 2215-2226.

29. Rubin CT, Bain SD, McLeod KJ. Suppression of the osteogenic response in the aging skeleton. *Calcified tissue international* 1992 Apr; **50**(4)**:** 306-313.

30. Turner CH, Takano Y, Owan I. Aging changes mechanical loading thresholds for bone formation in rats. *J Bone Miner Res* 1995 Oct; **10**(10)**:** 1544-1549.

31. Leader D, Williams SA, Curtis JR, Weiss R. Osteoporosis-Related Fracture Events in the US. *Journal of Clinical Densitometry* 2018 2018/10/01/; **21**(4)**:** 606.

32. Ominsky MS, Boyce RW, Li X, Ke HZ. Effects of sclerostin antibodies in animal models of osteoporosis. *Bone* 2017 Mar; **96:** 63-75.

33. McClung MR, Grauer A, Boonen S, Bolognese MA, Brown JP, Diez-Perez A, *et al.* Romosozumab in postmenopausal women with low bone mineral density. *N Engl J Med* 2014 Jan 30; **370**(5)**:** 412-420.

34. Cosman F, Crittenden DB, Adachi JD, Binkley N, Czerwinski E, Ferrari S, *et al.* Romosozumab Treatment in Postmenopausal Women with Osteoporosis. *N Engl J Med* 2016 Oct 20; **375**(16)**:** 1532-1543.

35. Holdsworth G, Greenslade K, Jose J, Stencel Z, Kirby H, Moore A, *et al.* Dampening of the bone formation response following repeat dosing with sclerostin antibody in mice is associated with up-regulation of Wnt antagonists. *Bone* 2018 Feb; **107:** 93-103.

36. Stolina M, Dwyer D, Niu QT, Villasenor KS, Kurimoto P, Grisanti M, *et al.* Temporal changes in systemic and local expression of bone turnover markers during six months of sclerostin antibody administration to ovariectomized rats. *Bone* 2014 Oct; **67:** 305-313.

37. Li X, Niu QT, Warmington KS, Asuncion FJ, Dwyer D, Grisanti M, *et al.* Progressive increases in bone mass and bone strength in an ovariectomized rat model of osteoporosis after 26 weeks of treatment with a sclerostin antibody. *Endocrinology* 2014 Dec; **155**(12)**:** 4785-4797.

38. Hung CT, Pollack SR, Reilly TM, Brighton CT. Real-time calcium response of cultured bone cells to fluid flow. *Clin Orthop Relat Res* 1995 Apr; (313)**:** 256-269.

39. Banes AJ, Tsuzaki M, Yamamoto J, Fischer T, Brigman B, Brown T, *et al.* Mechanoreception at the cellular level: the detection, interpretation, and diversity of responses to mechanical signals. *Biochem Cell Biol* 1995 Jul-Aug; **73**(7-8)**:** 349-365.

40. Hwang SY, Putney JW, Jr. Calcium signaling in osteoclasts. *Biochim Biophys Acta* 2011 May; **1813**(5)**:** 979-983.

41. Kajiya H, Okamoto F, Nemoto T, Kimachi K, Toh-Goto K, Nakayana S, *et al.* RANKL-induced TRPV2 expression regulates osteoclastogenesis via calcium oscillations. *Cell Calcium* 2010 Nov; **48**(5)**:** 260-269.

42. Donahue SW, Jacobs CR, Donahue HJ. Flow-induced calcium oscillations in rat osteoblasts are age, loading frequency, and shear stress dependent. *Am J Physiol Cell Physiol* 2001 Nov; **281**(5)**:** C1635-1641.

43. Jacobs CR, Yellowley CE, Davis BR, Zhou Z, Cimbala JM, Donahue HJ. Differential effect of steady versus oscillating flow on bone cells. *J Biomech* 1998 Nov; **31**(11)**:** 969-976.

44. Adachi T, Aonuma Y, Tanaka M, Hojo M, Takano-Yamamoto T, Kamioka H. Calcium response in single osteocytes to locally applied mechanical stimulus: differences in cell process and cell body. *J Biomech* 2009 Aug 25; **42**(12)**:** 1989-1995.

45. Rath AL, Bonewald LF, Ling J, Jiang JX, Van Dyke ME, Nicolella DP. Correlation of cell strain in single osteocytes with intracellular calcium, but not intracellular nitric oxide, in response to fluid flow. *J Biomech* 2010 May 28; **43**(8)**:** 1560-1564.

46. Lu XL, Huo B, Chiang V, Guo XE. Osteocytic network is more responsive in calcium signaling than osteoblastic network under fluid flow. *J Bone Miner Res* 2012 Mar; **27**(3)**:** 563-574.

47. Lu XL, Huo B, Park M, Guo XE. Calcium response in osteocytic networks under steady and oscillatory fluid flow. *Bone* 2012; **51**(3)**:** 466-473.

48. Brown GN, Leong PL, Guo XE. T-Type voltage-sensitive calcium channels mediate mechanically-induced intracellular calcium oscillations in osteocytes by regulating endoplasmic reticulum calcium dynamics. *Bone* 2016 Jul; **88:** 56-63.

49. Brown GN, Sattler RL, Guo XE. Experimental studies of bone mechanoadaptation: bridging in vitro and in vivo studies with multiscale systems. *Interface Focus* 2016 Feb 6; **6**(1)**:** 20150071.

50. Adachi T, Aonuma Y, Ito S, Tanaka M, Hojo M, Takano-Yamamoto T, *et al.* Osteocyte calcium signaling response to bone matrix deformation. *J Biomech* 2009 Nov 13; **42**(15)**:** 2507-2512.

51. Ishihara Y, Sugawara Y, Kamioka H, Kawanabe N, Hayano S, Balam TA, *et al.* Ex vivo real-time observation of Ca(2+) signaling in living bone in response to shear stress applied on the bone surface. *Bone* 2013 Mar; **53**(1)**:** 204-215.

52. Consensus development conference: diagnosis, prophylaxis, and treatment of osteoporosis. *Am J Med* 1993 Jun; **94**(6)**:** 646-650.

53. Manolagas SC, Jilka RL. Bone marrow, cytokines, and bone remodeling. Emerging insights into the pathophysiology of osteoporosis. *N Engl J Med* 1995 Feb 2; **332**(5)**:** 305-311.

54. Zebaze RM, Ghasem-Zadeh A, Bohte A, Iuliano-Burns S, Mirams M, Price RI, *et al.* Intracortical remodelling and porosity in the distal radius and post-mortem femurs of women: a cross-sectional study. *Lancet* 2010 May 15; **375**(9727)**:** 1729-1736.

55. Seeman E, Delmas PD. Bone quality--the material and structural basis of bone strength and fragility. *N Engl J Med* 2006 May 25; **354**(21)**:** 2250-2261.

56. Hemmatian H, Bakker AD, Klein-Nulend J, van Lenthe GH. Aging, Osteocytes, and Mechanotransduction. *Curr Osteoporos Rep* 2017 Oct; **15**(5)**:** 401-411.

57. Okada S, Yoshida S, Ashrafi SH, Schraufnagel DE. The canalicular structure of compact bone in the rat at different ages. *Microsc Microanal* 2002 Apr; **8**(2)**:** 104-115.

58. Busse B, Djonic D, Milovanovic P, Hahn M, Puschel K, Ritchie RO, *et al.* Decrease in the osteocyte lacunar density accompanied by hypermineralized lacunar occlusion reveals failure and delay of remodeling in aged human bone. *Aging Cell* 2010 Dec; **9**(6)**:** 1065-1075.

59. Tiede-Lewis LM, Xie Y, Hulbert MA, Campos R, Dallas MR, Dusevich V, *et al.* Degeneration of the osteocyte network in the C57BL/6 mouse model of aging. *Aging (Albany NY)* 2017 Oct 26; **9**(10)**:** 2190-2208.

60. Lai X, Price C, Modla S, Thompson WR, Caplan J, Kirn-Safran CB, *et al.* The dependences of osteocyte network on bone compartment, age, and disease. *Bone Res* 2015; **3**.

61. Holguin N, Brodt MD, Sanchez ME, Silva MJ. Aging diminishes lamellar and woven bone formation induced by tibial compression in adult C57BL/6. *Bone* 2014 Aug; **65:** 83-91.

62. Silva MJ, Brodt MD, Lynch MA, Stephens AL, Wood DJ, Civitelli R. Tibial loading increases osteogenic gene expression and cortical bone volume in mature and middle-aged mice. *PLoS One* 2012; **7**(4)**:** e34980.

63. Lynch ME, Main RP, Xu Q, Schmicker TL, Schaffler MB, Wright TM, *et al.* Tibial compression is anabolic in the adult mouse skeleton despite reduced responsiveness with aging. *Bone* 2011 Sep; **49**(3)**:** 439-446.

64. Klein-Nulend J, Sterck JG, Semeins CM, Lips P, Joldersma M, Baart JA, *et al.* Donor age and mechanosensitivity of human bone cells. *Osteoporos Int* 2002; **13**(2)**:** 137-146.

65. Sterck JG, Klein-Nulend J, Lips P, Burger EH. Response of normal and osteoporotic human bone cells to mechanical stress in vitro. *Am J Physiol* 1998 Jun; **274**(6 Pt 1)**:** E1113-1120.

66. Flurkey K, Currer J, Harrison D. *The Mouse in Aging Research*, vol. 3, 2007.

67. Patel TK, Brodt MD, Silva MJ. Experimental and finite element analysis of strains induced by axial tibial compression in young-adult and old female C57Bl/6 mice. *J Biomech* 2014 Jan 22; **47**(2)**:** 451-457.

68. Jing D, Lu XL, Luo E, Sajda P, Leong PL, Guo XE. Spatiotemporal properties of intracellular calcium signaling in osteocytic and osteoblastic cell networks under fluid flow. *Bone* 2013 Apr; **53**(2)**:** 531-540.

69. Kamel-ElSayed SA, Tiede-Lewis LM, Lu Y, Veno PA, Dallas SL. Novel approaches for two and three dimensional multiplexed imaging of osteocytes. *Bone* 2015 Jul; **76:** 129-140.

70. Vatsa A, Breuls RG, Semeins CM, Salmon PL, Smit TH, Klein-Nulend J. Osteocyte morphology in fibula and calvaria --- is there a role for mechanosensing? *Bone* 2008 Sep; **43**(3)**:** 452-458.

71. Lu Y, Xie Y, Zhang S, Dusevich V, Bonewald LF, Feng JQ. DMP1-targeted Cre expression in odontoblasts and osteocytes. *J Dent Res* 2007 Apr; **86**(4)**:** 320-325.

72. Zariwala HA, Borghuis BG, Hoogland TM, Madisen L, Tian L, De Zeeuw CI, *et al.* A Cre-dependent GCaMP3 reporter mouse for neuronal imaging in vivo. *J Neurosci* 2012 Feb 29; **32**(9)**:** 3131-3141.

73. Lewis KJ, Frikha-Benayed D, Louie J, Stephen S, Spray DC, Thi MM, *et al.* Osteocyte calcium signals encode strain magnitude and loading frequency in vivo. *Proc Natl Acad Sci U S A* 2017 Oct 31; **114**(44)**:** 11775-11780.

74. Plotkin LI, Speacht TL, Donahue HJ. Cx43 and mechanotransduction in bone. *Curr Osteoporos Rep* 2015 Apr; **13**(2)**:** 67-72.

75. Huo B, Lu XL, Costa KD, Xu Q, Guo XE. An ATP-dependent mechanism mediates intercellular calcium signaling in bone cell network under single cell nanoindentation. *Cell Calcium* 2010 Mar; **47**(3)**:** 234-241.

76. Huo B, Lu XL, Guo XE. Intercellular calcium wave propagation in linear and circuit-like bone cell networks. *Philos Trans A Math Phys Eng Sci* 2010 Feb 13; **368**(1912)**:** 617-633.

77. Thi MM, Suadicani SO, Schaffler MB, Weinbaum S, Spray DC. Mechanosensory responses of osteocytes to physiological forces occur along processes and not cell body and require alphaVbeta3 integrin. *Proc Natl Acad Sci U S A* 2013 Dec 24; **110**(52)**:** 21012-21017.

78. Huo B, Lu XL, Hung CT, Costa KD, Xu Q, Whitesides GM, *et al.* Fluid Flow Induced Calcium Response in Bone Cell Network. *Cell Mol Bioeng* 2008 Mar 1; **1**(1)**:** 58-66.

79. Davis HM, Aref MW, Aguilar-Perez A, Pacheco-Costa R, Allen K, Valdez S, *et al.* Cx43 overexpression in osteocytes prevents osteocyte apoptosis and preserves cortical bone quality in aging mice. *JBMR Plus* 2018 Jul; **2**(4)**:** 206-216.

80. Burge R, Dawson-Hughes B, Solomon DH, Wong JB, King A, Tosteson A. Incidence and economic burden of osteoporosis-related fractures in the United States, 2005-2025. *J Bone Miner Res* 2007 Mar; **22**(3)**:** 465-475.

81. Baron R, Hesse E. Update on bone anabolics in osteoporosis treatment: rationale, current status, and perspectives. *J Clin Endocrinol Metab* 2012 Feb; **97**(2)**:** 311-325.

82. FDA Approves EVENITY™ (romosozumab-aqqg) For The Treatment Of Osteoporosis In Postmenopausal Women At High Risk For Fracture. www.prnewswire.com: UCB and Amgen; 2019.

83. Poole KE, van Bezooijen RL, Loveridge N, Hamersma H, Papapoulos SE, Lowik CW, *et al.* Sclerostin is a delayed secreted product of osteocytes that inhibits bone formation. *FASEB J* 2005 Nov; **19**(13)**:** 1842-1844.

84. Winkler DG, Sutherland MK, Geoghegan JC, Yu C, Hayes T, Skonier JE, *et al.* Osteocyte control of bone formation via sclerostin, a novel BMP antagonist. *The EMBO journal* 2003 Dec 1; **22**(23)**:** 6267-6276.

85. van Bezooijen RL, Roelen BA, Visser A, van der Wee-Pals L, de Wilt E, Karperien M, *et al.* Sclerostin is an osteocyte-expressed negative regulator of bone formation, but not a classical BMP antagonist. *J Exp Med* 2004 Mar 15; **199**(6)**:** 805-814.

86. Semenov M, Tamai K, He X. SOST is a ligand for LRP5/LRP6 and a Wnt signaling inhibitor. *J Biol Chem* 2005 Jul 22; **280**(29)**:** 26770-26775.

87. Holdsworth G, Slocombe P, Doyle C, Sweeney B, Veverka V, Le Riche K, *et al.* Characterization of the interaction of sclerostin with the low density lipoprotein receptor-

related protein (LRP) family of Wnt co-receptors. *J Biol Chem* 2012 Aug 3; **287**(32)**:** 26464-26477.

88. Li X, Zhang Y, Kang H, Liu W, Liu P, Zhang J, *et al.* Sclerostin binds to LRP5/6 and antagonizes canonical Wnt signaling. *J Biol Chem* 2005 May 20; **280**(20)**:** 19883-19887.

89. Gong Y, Slee RB, Fukai N, Rawadi G, Roman-Roman S, Reginato AM, *et al.* LDL receptor-related protein 5 (LRP5) affects bone accrual and eye development. *Cell* 2001 Nov 16; **107**(4)**:** 513-523.

90. Glass DA, 2nd, Bialek P, Ahn JD, Starbuck M, Patel MS, Clevers H, *et al.* Canonical Wnt signaling in differentiated osteoblasts controls osteoclast differentiation. *Dev Cell* 2005 May; **8**(5)**:** 751-764.

91. Appelman-Dijkstra N, Van Lierop A, Papapoulos S. SOST-Related Sclerosing Bone Dysplasias. In: Adam MP, Ardinger HH, Pagon RA, Wallace SE, Bean LJH, Stephens K, *et al.* (eds). *GeneReviews((R))*: Seattle (WA), 1993.

92. Brunkow ME, Gardner JC, Van Ness J, Paeper BW, Kovacevich BR, Proll S, *et al.* Bone dysplasia sclerosteosis results from loss of the SOST gene product, a novel cystine knot-containing protein. *Am J Hum Genet* 2001 Mar; **68**(3)**:** 577-589.

93. Balemans W, Patel N, Ebeling M, Van Hul E, Wuyts W, Lacza C, *et al.* Identification of a 52 kb deletion downstream of the SOST gene in patients with van Buchem disease. *J Med Genet* 2002 Feb; **39**(2)**:** 91-97.

94. Holdsworth G, Roberts SJ, Ke HZ. Novel actions of sclerostin on bone. *J Mol Endocrinol* 2019 Feb 1; **62**(2)**:** R167-R185.

95. Ominsky MS, Richards WG, Li X, Ke HZ. Sclerostin and Dickkopf-1 as Therapeutic Targets in Bone Diseases. *Endocrine Reviews* 2012; **33**(5)**:** 747-783.

96. Li X, Ominsky MS, Niu QT, Sun N, Daugherty B, D'Agostin D, *et al.* Targeted deletion of the sclerostin gene in mice results in increased bone formation and bone strength. *J Bone Miner Res* 2008 Jun; **23**(6)**:** 860-869.

97. Li X, Ominsky MS, Warmington KS, Morony S, Gong J, Cao J, *et al.* Sclerostin antibody treatment increases bone formation, bone mass, and bone strength in a rat model of postmenopausal osteoporosis. *J Bone Miner Res* 2009 Apr; **24**(4)**:** 578-588.

98. Padhi D, Allison M, Kivitz AJ, Gutierrez MJ, Stouch B, Wang C, *et al.* Multiple doses of sclerostin antibody romosozumab in healthy men and postmenopausal women with low bone mass: a randomized, double-blind, placebo-controlled study. *J Clin Pharmacol* 2014 Feb; **54**(2)**:** 168-178.

99. Ominsky MS, Vlasseros F, Jolette J, Smith SY, Stouch B, Doellgast G, *et al.* Two doses of sclerostin antibody in cynomolgus monkeys increases bone formation, bone mineral density, and bone strength. *J Bone Miner Res* 2010 May; **25**(5)**:** 948-959.

100. Morrell AE, Brown GN, Robinson ST, Sattler RL, Baik AD, Zhen G, *et al.* Mechanically induced Ca(2+) oscillations in osteocytes release extracellular vesicles and enhance bone formation. *Bone Res* 2018; **6:** 6.

101. Weatherholt AM, Fuchs RK, Warden SJ. Cortical and trabecular bone adaptation to incremental load magnitudes using the mouse tibial axial compression loading model. *Bone* 2013 Jan; **52**(1)**:** 372-379.

102. Berman AG, Clauser CA, Wunderlin C, Hammond MA, Wallace JM. Structural and Mechanical Improvements to Bone Are Strain Dependent with Axial Compression of the Tibia in Female C57BL/6 Mice. *PLoS One* 2015; **10**(6)**:** e0130504.

103. Judex S, Donahue LR, Rubin C. Genetic predisposition to low bone mass is paralleled by an enhanced sensitivity to signals anabolic to the skeleton. *FASEB J* 2002 Aug; **16**(10)**:** 1280-1282.

104. McDonald MM, Reagan MR, Youlten SE, Mohanty ST, Seckinger A, Terry RL, *et al.* Inhibiting the osteocyte-specific protein sclerostin increases bone mass and fracture resistance in multiple myeloma. *Blood* 2017 Jun 29; **129**(26)**:** 3452-3464.

105. Taylor S, Ominsky MS, Hu R, Pacheco E, He YD, Brown DL, *et al.* Time-dependent cellular and transcriptional changes in the osteoblast lineage associated with sclerostin antibody treatment in ovariectomized rats. *Bone* 2016 Mar; **84:** 148-159.

106. Bonewald LF. The amazing osteocyte. *J Bone Miner Res* 2011 Feb; **26**(2)**:** 229-238.

107. Hu M, Tian GW, Gibbons DE, Jiao J, Qin YX. Dynamic fluid flow induced mechanobiological modulation of in situ osteocyte calcium oscillations. *Arch Biochem Biophys* 2015 Aug 1; **579:** 55-61.

108. Tanaka-Kamioka K, Kamioka H, Ris H, Lim S-S. Osteocyte Shape Is Dependent on Actin Filaments and Osteocyte Processes Are Unique Actin-Rich Projections. *Journal of Bone and Mineral Research* 1998; **13**(10)**:** 1555-1568.

109. Kamioka H, Sugawara Y, Honjo T, Yamashiro T, Takano-Yamamoto T. Terminal differentiation of osteoblasts to osteocytes is accompanied by dramatic changes in the distribution of actin-binding proteins. *J Bone Miner Res* 2004 Mar; **19**(3)**:** 471-478.

110. Murshid SA, Kamioka H, Ishihara Y, Ando R, Sugawara Y, Takano-Yamamoto T. Actin and microtubule cytoskeletons of the processes of 3D-cultured MC3T3-E1 cells and osteocytes. *J Bone Miner Metab* 2007; **25**(3)**:** 151-158.

111. Baik AD, Qiu J, Hillman EM, Dong C, Edward Guo X. Simultaneous Tracking of 3D Actin and Microtubule Strains in Individual MLO-Y4 Osteocytes under Oscillatory Flow. *Biochem Biophys Res Commun* 2013 Jan 22.

112. Baik AD, Lu XL, Qiu J, Huo B, Hillman EM, Dong C, *et al.* Quasi-3D cytoskeletal dynamics of osteocytes under fluid flow. *Biophys J* 2010 Nov 03; **99**(9)**:** 2812-2820.

113. Brown GN. The Sustainment and Consequences of Cytosolic Calcium Signals in Osteocytes. PhD thesis, Columbia University, 2016.

114. Kuo IY, Ehrlich BE. Signaling in muscle contraction. *Cold Spring Harb Perspect Biol* 2015 Feb 2; **7**(2)**:** a006023.

115. Wollman R, Meyer T. Coordinated oscillations in cortical actin and Ca2+ correlate with cycles of vesicle secretion. *Nat Cell Biol* 2012 12//print; **14**(12)**:** 1261-1269.

116. Bement WM, Mandato CA, Kirsch MN. Wound-induced assembly and closure of an actomyosin purse string in Xenopus oocytes. *Curr Biol* 1999 Jun 3; **9**(11)**:** 579-587.

117. Clark AG, Miller AL, Vaughan E, Yu HY, Penkert R, Bement WM. Integration of single and multicellular wound responses. *Curr Biol* 2009 Aug 25; **19**(16)**:** 1389-1395.

118. Stanisstreet M. Calcium and wound healing in Xenopus early embryos. *J Embryol Exp Morphol* 1982 Feb; **67:** 195-205.

119. Paic F, Igwe JC, Nori R, Kronenberg MS, Franceschetti T, Harrington P, *et al.* Identification of differentially expressed genes between osteoblasts and osteocytes. *Bone* 2009 Oct; **45**(4)**:** 682-692.

120. Riedl J, Crevenna AH, Kessenbrock K, Yu JH, Neukirchen D, Bista M, *et al.* Lifeact: a versatile marker to visualize F-actin. *Nat Methods* 2008 Jul; **5**(7)**:** 605-607.

121. Riedl J, Flynn KC, Raducanu A, Gartner F, Beck G, Bosl M, *et al.* Lifeact mice for studying F-actin dynamics. *Nat Methods* 2010 Mar; **7**(3)**:** 168-169.

122. Boyle JJ, Kume M, Wyczalkowski MA, Taber LA, Pless RB, Xia Y, *et al.* Simple and accurate methods for quantifying deformation, disruption, and development in biological tissues. *J R Soc Interface* 2014 Nov 06; **11**(100)**:** 20140685.

123. Ishihara Y, Sugawara Y, Kamioka H, Kawanabe N, Kurosaka H, Naruse K, *et al.* In situ imaging of the autonomous intracellular Ca(2+) oscillations of osteoblasts and osteocytes in bone. *Bone* 2012 Apr; **50**(4)**:** 842-852.

124. Borysova L, Dora KA, Garland CJ, Burdyga T. Smooth muscle gap-junctions allow propagation of intercellular Ca(2+) waves and vasoconstriction due to Ca(2+) based action potentials in rat mesenteric resistance arteries. *Cell Calcium* 2018 Nov; **75:** 21-29.

125. Hashitani H, Brading AF, Suzuki H. Correlation between spontaneous electrical, calcium and mechanical activity in detrusor smooth muscle of the guinea-pig bladder. *Br J Pharmacol* 2004 Jan; **141**(1)**:** 183-193.

126. Théry C. Exosomes: secreted vesicles and intercellular communications. *F1000 Biology Reports* 2011 07/01; **3:** 15.

127. Nightingale TD, White IJ, Doyle EL, Turmaine M, Harrison-Lavoie KJ, Webb KF, *et al.* Actomyosin II contractility expels von Willebrand factor from Weibel–Palade bodies during exocytosis. *The Journal of Cell Biology* 2011 August 22, 2011; **194**(4)**:** 613-629.

128. McGarry JG, Klein-Nulend J, Prendergast PJ. The effect of cytoskeletal disruption on pulsatile fluid flow-induced nitric oxide and prostaglandin E2 release in osteocytes and osteoblasts. *Biochem Biophys Res Commun* 2005 Apr 29; **330**(1)**:** 341-348.

129. Solberg LB, Stang E, Brorson SH, Andersson G, Reinholt FP. Tartrate-resistant acid phosphatase (TRAP) co-localizes with receptor activator of NF-KB ligand (RANKL) and osteoprotegerin (OPG) in lysosomal-associated membrane protein 1 (LAMP1)-positive vesicles in rat osteoblasts and osteocytes. *Histochem Cell Biol* 2015 Feb; **143**(2)**:** 195-207.

130. Pan J, Zhang T, Mi L, Zhang B, Wang B, Yang L, *et al.* Stepwise increasing and decreasing fluid shear stresses differentially regulate the functions of osteoblasts. *Cell Mol Bioeng* 2010 Dec; **3**(4)**:** 376-386.

131. Zhang X, Cui X, Cheng L, Guan X, Li H, Li X, *et al.* Actin stabilization by jasplakinolide affects the function of bone marrow-derived late endothelial progenitor cells. *PLoS One* 2012; **7**(11)**:** e50899.

132. Arnsdorf EJ, Tummala P, Kwon RY, Jacobs CR. Mechanically induced osteogenic differentiation--the role of RhoA, ROCKII and cytoskeletal dynamics. *Journal of cell science* 2009 Feb 15; **122**(Pt 4)**:** 546-553.

133. Chen Z, Luo Q, Lin C, Kuang D, Song G. Simulated microgravity inhibits osteogenic differentiation of mesenchymal stem cells via depolymerizing F-actin to impede TAZ nuclear translocation. *Sci Rep* 2016 Jul 22; **6:** 30322.